

Karl F. Kleinau

Development of Environment-Friendly Concrete Constructions by use of Aluminium Reinforcement

Master's thesis in Industriell kjemi og bioteknologi - masterstudium (5-årig)

Supervisor: Ida Westermann

Co-supervisor: Harald Justnes, Trond Furu

June 2022

Karl F. Kleinau

Development of Environment-Friendly Concrete Constructions by use of Aluminium Reinforcement

Master's thesis in Industriell kjemi og bioteknologi - masterstudium (5-
årig)

Supervisor: Ida Westermann

Co-supervisor: Harald Justnes, Trond Furu

June 2022

Norwegian University of Science and Technology
Faculty of Natural Sciences
Department of Materials Science and Engineering



Norwegian University of
Science and Technology

Preface

I want to thank everyone who has helped me through the last five years, which has resulted in this master's thesis. First, I like to thank my supervisor and co-supervisors Ida Westermann, Harald Justnes, and Trond Furu for their good follow-up over the past year. Furthermore, I would like to thank Øyvind Lindgrd, Giovanni Scilipoti, Yannick Anton, Kristian Aamot, and the rest of the SINTEF team for their guidance and support during the experimental part of the master's. A thank also goes to Yingda Yu and Kai Zhang for their training and experience transfer assistance. Last but not least, I like to thank my friends and family for their help and support over the last five years.

Abstract

Cement production is responsible for the third-largest CO₂-emission in modern times, accounting for 8% of worldwide CO₂-emissions with 4.1 billion metric tonnes emitted yearly. Moreover, corrosion of reinforcing steel, the most widely used reinforcing material, reduces structural functionality and service life. Globally, renovating concrete infrastructure is anticipated to cost 100 billion dollars annually. Consequently, there is a considerable need for environmentally friendly, corrosion-resistant concrete constructions.

Using Supplementary cement materials (SCM) and aluminium reinforcements, the problem of greenhouse gas emissions and corrosion can be resolved. CO₂-emissions are drastically decreased by substituting high-emitting cement with SCM such as hyaloclastite and Calcined clay (CC) that have no or significant reduced greenhouse gas emissions. Although the alkalinity of the cement paste in conventional concrete constructions leads to the active corrosion of aluminium, SCM's ability to minimise alkalinity will enable the use of recycled aluminium, further reducing greenhouse gas emissions. The concrete structure will further benefit from the future abundance of aluminium alloys in the automotive industry.

This master's thesis maps the potential for using environmentally friendly concrete structures where 55 % of the cement has been replaced with SCM, and the aluminium alloys 6082 and 4xxxAl, found in engine blocks, have been used as reinforcement. The potential of the concrete structure was evaluated by determining the structure's corrosion inhibition, studying the interface between the reinforcement and concrete, and examining the concrete structure's mechanical bonding strength.

The results showed excellent corrosion resistance by the addition of CaCl₂ and the use of hyaloclastite as SCM. Furthermore, using Industry cement (ICEM) in concrete structures revealed promising prospects for future research. By reducing the noise level by a factor of 2.74 and the injection interval by a factor of 3.33, developing a new Flow system improved the accuracy and reliability of the measurements and will therefore be suggested for further study. Analysis of the interface between reinforcement and concrete for samples without additional CaCl₂ revealed the production of a brittle, porous layer composed of multiple aluminium oxides. The results indicate that recycled alloy 4xxxAl has good qualities and superior corrosion resistance than 6082 alloys. Better corrosion resistance was explained by a higher Si concentration in 4xxxAl alloys, which has an inhibitory corrosion effect. Although the EDS did not identify the anticipated protective Si layer when CaCl₂ was added to the concrete, the layer was indirectly detected by GC measurements. The silicate layer increased the concrete's adherence to the reinforcement. The adhesion and friction of minor pitting contributed to the 6082 reinforcement's superior bond strength compared to stainless steel reinforcements. Compared to L-shaped profiles, the geometry of smooth bars increased bond strength due to homogeneous adhesion and less

air bubble accumulation at the interface between the reinforcing bar and the concrete.

In conclusion, the results indicate that the new concrete structures with aluminium reinforcements and SCM have the potential to replace more conventional CO₂-emitting concrete structures. Since 6082 smooth bars in the new concrete structure satisfy both chemical and mechanical requirements, the structure has a high potential for application and will contribute to achieving Sustainable Development Goals.

Sammendrag

Sementproduksjon utgjør det tredje største CO₂-utslippet i moderne tid og står for 8% av de globale utslippene med 4,1 milliarder metriske tonn årlig. Videre fører korrosjon av armeringsstål til reduksjon i funksjonalitet og levetid til det mest brukte armeringsmaterialet. Globalt forventes renovering av betonginfrastruktur å koste 100 milliarder dollar årlig. Det er derfor et betydelig behov for miljøvennlige, korrosjonsbestandige betongkonstruksjoner.

Korrosjon og klimaproblemene kan løses ved bruk av *Supplementary Cement Materials* (SCM) og aluminiumsarmeringer. CO₂-utslippet reduseres drastisk ved å erstatte høytutslippende sement med SCM som hyaloklastitt og kalsinert leire (CC), som har ingen eller betydelig reduserte klimautslipp. Selv om sementpastens alkalitet i konvensjonelle betongkonstruksjoner fører til aktiv korrosjon av aluminium, vil SCMs evne til å minimere alkaliteten i løsningen muliggjøre bruk av resirkulert aluminium. Betongstrukturen vil ytterligere dra nytte av den fremtidige overfloden av aluminiumslegeringer fra bilindustrien.

Denne masteroppgaven kartlegger potensialet for å bruke miljøvennlige betongkonstruksjoner hvor 55 % av sementen er erstattet med SCM og aluminiumslegeringene 6082 og 4xxxA, funnet i motorblokker, er brukt som armering. Betongkonstruksjonens potensial ble evaluert ved å bestemme konstruksjonens korrosjonsmotstand, studere grensesnittet mellom armering og betong og undersøke betongkonstruksjonens mekaniske bindestyrke.

Resultatene viste utmerket korrosjonsmotstand ved tilsetning av CaCl₂ og bruk av hyaloklastitt som SCM. Videre viser bruk av industri-sement (ICEM) i betongkonstruksjoner lovende resultater for fremtidig forskning. Utvikling av et nytt Flow-system reduserer støynivået med en faktor på 2,74 og injeksjonsintervallet med en faktor på 3,33, som fører til mer presise og pålitelige målinger. Bruk av Flow-system anbefales derfor til videre forskning. Analyse av grensesnittet mellom armering og betong for prøver uten tilsatt CaCl₂ viste dannelse av et sprøtt, porøst lag sammensatt av flere aluminiumoksider. Resultatene indikerer at 4xxxA-legeringer har bedre korrosjonsmotstand enn 6082-legeringer. Bedre korrosjonsmotstand kan skyldes en høyere Si-konsentrasjonen i 4xxxA-legeringer, som viser til en hemmende korrosjonseffekt. Selv om EDS ikke fant det forventede beskyttende silikatlaget ved tilsatt CaCl₂ til betongen, ble laget indirekte funnet av GC-målinger. Silikatlaget økte betongens vedheft til armeringen. Adhesjonen og friksjonen ved små gropdannelser i armeringen bidro til at 6082-armeringen hadde en bedre bindestyrke sammenlignet med stålarmeringer. Sammenlignet med L-formede profiler, økte geometrien til glatte stenger bindestyrken på grunn av en homogen vedheft og mindre luftbobleakkumulering i grensesnittet mellom armeringsjernet og betongen.

Oppsummert indikerer resultatene at de nye betongkonstruksjonene med aluminiumsarmeringer og SCM har potensial til å erstatte mere konvensjonelle høytutslippende betongkonstruksjoner. Siden 6082 glatte stenger i den nye be-

tongkonstruksjonen tilfredsstillter både kjemiske og mekaniske krav, har konstruksjonen et stort brukspotensial og vil bidra til å nå de globale klimamålene.

Abbreviation

at%	atomic percent
CC	Calcinied Clay
CCEM	Construction cement
CEM	Cement
DARE2C2	Durable Aluminium Reinforced Environmentally-friendly Concrete Construction
DC	Direct cooling
EDS	Energy-dispersive X-ray spectroscopy
FRP	Fibre-reinforced plastic
GC	Gass chromatography
GGBS	Granulated blast furnace slag
ICEM	Industrial cement
IEA	Internationaø Energy Agency
IP	Inner product
LM	Light microscope
Nor. wt %	Normalised weight precent
OP	Outer product
OPC	Ordinary Portland Cement
RT	Room temperature
SCM	Supplementary cement material
SEM	Secondary electron microscope
SFE	Stacking fault energy
TMP	Thermomechanical process
w/c	Water to cement ratio
wt%	weight percent

Symbol list

Δ	Heating up
Δ_o	Slippage under tension force
δE	Energy gap
E_{HOMO}	Energy of highest occupied molecular orbital
E_{LOMO}	Energy of lowest unoccupied molecular orbital
F_a	Tensile strenght
f_c	Average concrete strenght
f_{em}	Target value of strenght
μ	Micro
\emptyset	Diameter
σ	Standard deviation
τ_{dm}	Bond stress
τ_{cr}	Splitting bond stress

1 Chemical notation

Al	Aluminium
Al_2O_3	Alumina
$\text{Al}(\text{OH})_3$	Aluminium hydroxide(Gibbsite)
$\text{Al}(\text{OOH})$	Aluminium hydroxide oxide
$\text{Al}(\text{OH})_2\text{O}^-$	Aluminium hydroxide oxide ion
$\text{Al}(\text{OH})_2^{2+}$	Aluminium hydroxide ion
AlP	Aluminium phosphate
Ca	Calcium
$\text{Ca}_3\text{Al}_2\text{O}_6 \cdot \text{CaCl}_2 \cdot 12 \text{H}_2\text{O}$	Friedel's salt
$\text{CaAl}_2\text{O}_6 \cdot 6\text{H}_2\text{O}$	Calcium aluminium hydrate
CaCl_2	Caclium chloride
CaCO_3	Calcium carbonate
CaO	Calcium oxide
$\text{Ca}(\text{OH})_2$	Calcium hydroxide
$\text{CaSiO}_3 \cdot \text{H}_2\text{O}$	Calcium silica hydrate
Cl	Chlorine
Cl^-	Chloride ione
CO_2	Carbon dioxide
Cu	Copper
F	Fluorine
Fe	Iron
Fe^{2+}	Iron ion
Fe_2O_3	Iron oxide
$\text{Fe}(\text{OH})_2$	Iron hydroxide
FeOOH	Iron hydroxide oxide
H/H ₂	Hydrogen
$\text{H}^+ / \text{H}_3\text{O}^+$	Hydrogen ion
HCO_3^-	Bicarbonate
H_2O	Hydrogen dioxide/freshwater
K	Potassium
K_2O	Potassium oxide
Mg	Magnesium
MgO	Magnesium oxide
Mg_2Si	Magnesium silicate
Na	Sodium
Na_2	Sodium
NaCl	Sodium chloride
NaOH	Sodium hydroxide
NaSi	Sodium silicate
NaSiO_3	Sodium silicate
O/ O ₂	Oxygen
OH^-	Hydroxide ion
Si	Silicon
SiO_2	Silica
SiO_3^-	Silicon oxide ion

Contents

1	Chemical notation	8
2	Introduction	1
3	Theory	4
3.1	Concrete	4
3.1.1	Cement production	4
3.1.2	Cement hydration	6
3.2	Corrosion of metals	9
3.2.1	Passivity and creation of an oxide layer	9
3.2.2	Variation of corrosion rate determined by pH of different metals	11
3.3	Degradation of steel reinforcements	13
3.3.1	Corrosion of steel reinforcements	13
3.3.2	Preventing corrosion of steel reinforcements	14
3.4	Aluminium as reinforcement	14
3.4.1	Cast and wrought alloys	15
3.4.2	Production of aluminium alloys	15
3.4.3	Hardenable and non-hardenable alloys	17
3.4.4	Heat Treatment by aging	17
3.4.5	Aluminium alloys microstructure	17
3.4.6	Microstructure extrusion	19
3.5	Corrosion of Aluminium	21
3.5.1	Formation of an oxide layer on aluminium	21
3.5.2	Corrosion of aluminium in strong alkaline environments	22
3.5.3	Pitting corrosion	23
3.6	Innovation of a paste suitable with aluminium	24
3.6.1	Supplementary cementitious materials (SCM)	25
3.6.2	Classification of SCMs	25
3.6.3	SCM mechanism	26
3.6.4	Calsined clay (CC)	27
3.6.5	Hyaloclastite	27
3.6.6	Calcium chloride (CaCl_2)	28
3.6.7	Silicate layer mechanism	29
3.7	Mechanical properties	30
3.7.1	Bond strength of concrete constructions	30
3.8	Principle of SEM and EDS	32
3.8.1	Scanning Electron Microscope (SEM)	33
3.8.2	Energy-Dispersive X-ray Spectroscopy (EDS)	33
4	Experimental	34
4.1	Materials used in the experiment	36
4.1.1	6082 and 4xxxAl alloys	36
4.1.2	Ordinary Portland Cement (OPC)	37

4.1.3	Calcined clay (CC)	37
4.1.4	Hyaloclastite	37
4.2	Investigation of chemical corrosion qualities for the concrete construction	38
4.2.1	Procedure	39
4.3	Experimental setup	41
4.3.1	Stationary setup	41
4.3.2	Flow system setup	42
4.4	Measurements conducted prior to GC measurements of the Flow system	44
4.4.1	Determining the desiccator and distillation tube's volume	44
4.4.2	Determining the volume of air in the gas bag	45
4.5	Analysis of the concrete construction	45
4.5.1	Sample preparation for surface and interface analysis	46
4.6	Mechanical properties	49
4.6.1	Preparation and heat treatment of the 6082 reinforcements	49
4.6.2	Pull-out test	50
5	Results	53
5.1	Investigation of chemical corrosion qualities for the concrete construction	53
5.1.1	Stationary setup	53
5.1.2	Flow system setup	54
5.2	Surface analysis	58
5.2.1	Stereo microscope	58
5.2.2	SEM surface analysis	59
5.2.3	EDS for surface analysis	63
5.3	Interface analysis	66
5.3.1	LM and SEM	66
5.3.2	EDS for interfacial analysis	71
5.4	Mechanical results	75
5.4.1	Pull-out test for 6082 and stainless steel smooth bars	75
5.4.2	Pull-out test for 6082 smooth bar and L-shape profiles	77
6	Discussion	82
6.1	Corrosion preventing qualities for generated environmentally friendly concrete constructions	82
6.1.1	Potential of hyaloclastite as SCM	82
6.1.2	Potential of utilising ICEM in newly created cement constructions	84
6.2	Comparing the Stationary and Flow system setup	85
6.2.1	Flow system calibration	85
6.2.2	Standard deviation and noise level of the two setups	85
6.2.3	Registration of H ₂ for the setups	87
6.3	Analysis of the reinforcing-concrete interface	89

6.3.1	Aluminium oxide layer for samples without CaCl_2	89
6.3.2	Corrosion resistance of 6082 and 4xxxA reinforcement . . .	90
6.3.3	Silica layer	92
6.3.4	Samples with added CaCl_2	93
6.3.5	Errors from EDS-analysis	94
6.4	Mechanical bonding properties for concrete construction determined by pull-out test	95
6.4.1	Comparing bond strenght of 6082 and stainless steel reinforcements	96
6.4.2	Comparing bond stress of bars and L-shape profiles for 6082 reinforcements	97
6.4.3	Analysis of reinforcement imprints	98
7	Conclusion	100
8	Further Work	102
A	Theoretical additional information	111
A.1	Pourbaix diagram for aluminium and steel	111
B	Additional experimental information	112
B.1	Table: Determine the volume of air in the gas bag	114
C	Additional results	115
C.1	LM	115
C.1.1	Difference between addition of CaCl_2 to the cement paste for 6082 reinforcements	115
C.1.2	Difference between addition of CaCl_2 to the cement paste for 4xxxA reinforcements	117
C.2	Coating thickness	118
C.3	Standard deviation and noise level of the two setups using Estonian CC	119
C.4	EDS spectra	120
C.4.1	Surface area analysis	120
C.4.2	Interfacial analysis	123
C.4.3	EDS-spectres for samples with CaCl_2	124

2 Introduction

Concrete, produced by combining stone materials and gravel with water (H_2O) and cement, is the most frequently used and significant building material of the twenty-first century. It can be found in anything from cast-in-place bridges, dams, and buildings to prefabricated beams, columns, and walls^[1]. In terms of annual usage and output, only water beats concrete^{[2][3]}.

Cement production is currently the third-largest source of CO_2 -emissions, following the heating/cooling of buildings with fossil fuel and the transportation sector with internal combustion engines^{[4][5]}. In 2019, the world produced 4.1 billion metric tonnes of cement, accounting for 8% of global CO_2 -emissions^{[5][6][7]}. Using fossil fuels, it is predicted that one metric tonne of CO_2 is emitted per tonne of cement produced^[8]. 60 % of the CO_2 -emissions in this process result from the decomposition of limestone during burning, and 40 % are the consequence of the fuel necessary to reach the melting temperature of the clinkers, which is correspondingly $1450\text{ }^\circ\text{C}$ ^{[9][10]}. The high CO_2 values in cement manufacture are not necessarily attributable to the environmentally unfriendly nature of the process itself but rather to the extensive usage of cementitious material^[8]. The International Energy Agency (IEA) predicts a 12-23 % increase in demand for concrete structures by 2050 due to an increasing trend in economic development. The rise in demand is primarily attributable to the expectation of economic expansion in Asia, Africa, Latin America, and the Middle East^{[6][11][12]}.

Four strategies have been formulated to reduce CO_2 -emissions during cement production:

1. Substitute low-carbon alternatives for fossil fuels high in carbon
2. Increase energy efficiency during combustion
3. Capture and store CO_2 extracted from flue gas^[13]
4. Utilise supplementary cementitious materials (SCM) in place of cement clinker^[14]

Replacing Portland clinker in cement with supplemental cementing materials (SCM) is the quickest and easiest technique to minimise CO_2 -emissions from cement production^[15]. Since the maximum limit for thermal energy efficiency in the melting furnace has nearly been reached, and different fuels will also affect the characteristics of cement clinkers, the potential for these alternatives is limited^[16]. Moreover, the capture and storage of CO_2 have not been implemented practically in the concrete industry. Although this approach has enormous potential for the future, it is not a cost-effective solution at the moment^[17].

Energy and CO_2 -emissions are significantly reduced when SCM replaces cement clinkers. Limestone, slag, fly ash, calcined clay (CC) or vulcanic glass like hyaloclastite can all be utilised as SCMs^[9]. The potential of CC, a relatively novel SCM, is enormous. Transport costs and mining will be favourable and have a

sustainable future due to the world's vast clay reserves^{[16][18]}. In addition, the melting temperature of CC, which ranges from 600-800°C, results in substantial energy and CO₂-emissions savings. Hyaloclastite, which is an volcanic glass, is another material which has shown promising SCM properties due to its chemical composition and grain size. In addition, the fact that hyaloclastite does not require heat treatment or preparation before usage makes it extremely energy efficient^{[19][20]}.

To create new concrete structures that are environmentally friendly, the chemical and mechanical problems of concrete structures must be solved.

Corrosion of steel reinforcement is currently the most significant chemical challenge for concrete constructions. Steel reinforcement is the most prevalent reinforcement in structural concrete and is corroded by chloride attack and carbonation^[9]. To preserve the steel reinforcement, a layer of extra-thick, permeable concrete is applied, while the pH of the cement is increased to passivate the steel reinforcement. Consequently, more concrete is utilised than is required for the concrete structure, leading to increased CO₂-emissions. Forming concrete structures with non-corroding reinforcements will result in more environmentally friendly constructions since less cement and CO₂-emissions will be produced simultaneously as the structure has a longer service life.

Most corrosion-resistant reinforcements consist of stainless steel and fibre-reinforced plastic (FRP). Unfortunately, the high cost of stainless steel precludes the economic viability of this solution. Due to the fragility of FRP, this solution cannot be implemented^{[9][21]}. In recent years, aluminium has been seen as a viable alternative for concrete structures.

Aluminium is the third most common element in the earth's crust, corresponding to 8.1%. The dispersion of the material makes it economically advantageous for use as reinforcement in concrete structures, while the material's ductility results in the required mechanical qualities. Aluminium has not been explored as a reinforcement because the cement's alkaline environment causes corrosion. This issue is resolved with SCM, which neutralises cement paste by precipitating hydroxides and aggressive chlorides into stable hydrates and Friedel's salt^{[22][8][23]}. In addition, the author's prior research has demonstrated that adding CaCl₂ to cement paste reduces the corrosion mechanism significantly. The usage of aluminium reinforcements in concrete structures in which a portion of the cement has been replaced with SCMs and CaCl₂ has been added would therefore be able to solve the most significant chemical problems in concrete structures today and will be an excellent candidate for the development of a new environmentally friendly concrete structure.

The type of cement that can be used has an additional influence on the sustainability of the new concrete constructions. Cement can be separated into construction cement and industrial cement(ICEM), with construction cement(CCEM) being used for more significant constructions and industrial cement being utilised

for element manufacture due to its greater early strength. Due to the early strength of ICEM, casting work can be performed in the winter. The ability of the new cement structure to utilise ICEM will therefore be of practical and economic relevance^[24].

Bonding behaviour is one of the most important mechanical properties of concrete constructions. This technique ensures that the reinforcement and concrete behave as a unit. Reinforced concrete constructions are designed to combine the reinforcement's and concrete's mechanical qualities. This is done by the reinforcement equalising tensile stresses while the concrete resists compressive stresses. In order to minimise slippage and the loss of the combined mechanical effect, it will be crucial to establish strong bonding force transmissions at the interface of the concrete and reinforcement while creating new environment-friendly concrete structures^{[25] [26] [27] [28]}.

This master's thesis was written in partnership with the Norwegian research project DARE2C2 (Durable Aluminium Reinforced Environmentally-friendly Concrete Construction). The objective of DARE2C2 is to create environmentally friendly concrete in which $> 50\%$ of the cement has been substituted with SCM. In addition, DARE2C2 utilizes the expected future abundance of secondary high-alloy aluminium alloys from the automotive industry by using these as reinforcements. By decreasing the quantity of cement in concrete, increasing the service life of concrete structures, and using recyclable materials, this technique offers an excellent ability to reduce CO₂-emissions significantly, thereby contributing to the achievement of the Sustainable Development Goals.

Aim of Work

The master's thesis aims to map the potential for aluminium reinforcements in concrete structure by looking at the chemical corrosion resistance and the mechanical bonding strength of the new concrete construction.

3 Theory

The theoretical component of the master's thesis contains the foundational knowledge upon which the remainder of the thesis is built. The theory relies in part on the author's earlier work.

The section starts with a description of the production and hydration of concrete. The corrosion of metals is described further, where passivity and the development of oxide layers are outlined before the variance in corrosion rates for various metals at different pH values is addressed. After establishing the corrosion mechanism for steel in concrete constructions, the assignment addresses aluminium reinforcement. This is accomplished by detailing the manufacture and microstructure of aluminium alloys before describing their corrosion mechanisms. The next paragraph describes the creation of a novel cement paste that is compatible with aluminium reinforcements. This is achieved by addressing the function of supplementary cement materials (SCM) in forming new concrete structures. The possible SCMs calcined clay and hyaloclastite are then presented. In addition, calcium chloride is provided as an effective corrosion inhibitor. The thesis will then concentrate on the mechanical properties of bond stress and how these properties affect the concrete structure. Finally, the principles of SEM and EDS are presented

3.1 Concrete

The construction material concrete is a composite mixture of aggregates and pastes bound into a solid mass. The aggregates are coarse gravel, sand and crushed stone, while the paste is cement and water. The aggregates make up approximately 70% of the volume, while the cement paste represents 30% of the total volume.

Due to concrete's properties, availability and reasonableness, it is second only to water the most consumed material. With three tonnes per year used per person globally, concrete is now consumed more than any other engineering material and is used twice as much as all other building materials combined^{[1][29]}.

3.1.1 Cement production

Cement is a fine powdery mineral hydraulic binder that is the main component in concrete and causes its hardening properties. The binder consists of the four main clinker components Alite (Ca_3SiO_5), Belite (Ca_2SiO_4), Aluminate ($\text{Ca}_3\text{Al}_2\text{O}_6$) and Ferrite ($\text{Ca}_2\text{AlFeO}_5$), which are formed when calcareous and silicon-containing minerals with minor amounts of alumina (Al_2O_3) and ferric oxide, clay, sand and iron are burned together at high temperatures. The formed tiles are then ground with limestone and plaster to produce cement. Table 3.1 shows the Major crystalline phase, Mineralogical term, Chemical notation and Shortened notation for the four main clinker components. Since the production process of cement is very energy-intensive, cement production accounts for

90% of the total energy consumption of concrete production. 60% of the energy in cement production is caused by the decomposition of the raw material limestone, clay and sand to the clinker phase during firing, as reproduced in Reaction 3.1, while the heating of the furnace to reach the clinker temperature of the raw materials at 1450°C accounts for 40% of the energy^[30].

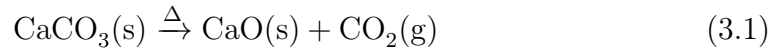


Table 3.1: Major crystalline phase, Mineralogical term, Chemical notation and Shortened notation for the four main clinker components in cement.

Major crystalline phase	Mineralogical term	Chemical notation	Shortened notation
Tricalcium silicate	Alite	3 CaO·SiO ₂	C ₃ S
Dicalcium silicate	Belite	2 CaO·SiO ₂	C ₂ S
Tricalcium aluminate	Aluminate	3 CaO·Al ₂ O ₃	C ₃ A
Tetracalcium aluminoferrite	Ferite	4 CaO·Al ₂ O ₃ ·Fe ₂ O ₃	C ₄ AF

Cement can be produced in two different production processes, called the dry and wet process, which differs in that water is added to the raw materials in the wet process to form a slurry mixture. In contrast, the raw materials in the dry process are dry and mixed before being placed in the cement kiln. Since the dry process is more environmentally friendly than the wet process, the descriptive production process will be based on the dry method. The cement production process is divided into mining, crushing and grinding raw materials (limestone and clay), mixing the raw materials, calcination of the materials using a rotary kiln, and cooling the resulting clinkers before milling and mixing the clinkers with gypsum. Figure 3.1 shows the cement production process using a flowchart. Mining of limestone is extracted usually near the cement plant through blasting techniques. The mixing process starts with a premixing phase where the raw materials limestone, clay and sand are ground and mixed in a homogeneous mixture to form the raw meal.

The production process continues by calcining the feedstock and decomposing the clay minerals in a 900 °C rotary kiln. The decomposition of the clay minerals results in the formation of SiO₂ and Al₂O₃ while the calcium carbonate is converted to calcium oxide (CaO). Furthermore, calcination of CaO will occur when CaCO₃ releases CO₂. The calcination process is given in Reaction 3.1. The calcination process is followed by the clinker process, where CaO reacts with SiO₂, Al₂O₃ and ferrous oxides at high temperatures to form silicates, ferrites and aluminates. The process takes place in a sloping furnace with a rotation of 3-5 rpm and a temperature of 1450 °C. The clinkers formed are then cooled down to room temperature (RT), where it is essential that the cooling takes place as quickly as possible to improve the clinker quality and recover the energy from heating. Hence, shaker coolers are used to cool down the clinkers. The cooled clinkers are ground and then milled together with gypsum, limestone and other additives

to produce the desired composition of the Portland cement. The additions of gypsum and limestone are due to regulation of the curing time^[10].

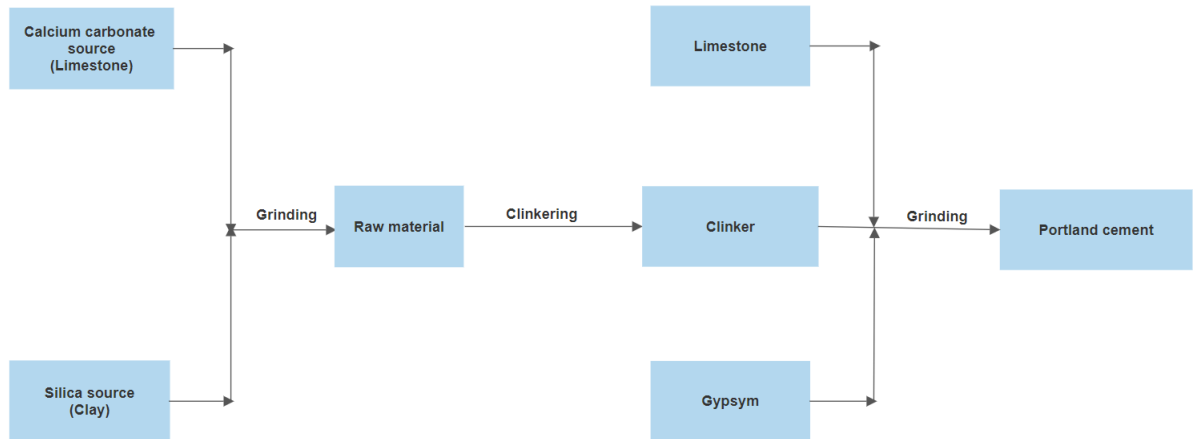
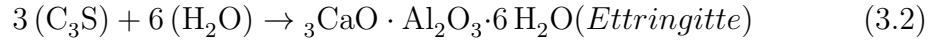


Figure 3.1: Flowchart of the production of Portland cement. The process begins with preparing a raw material consisting of calcium carbonate (limestone) and silica (clay). Limestone and Gypsum are added to the clinker after being clinker and cooled before processing to Portland.

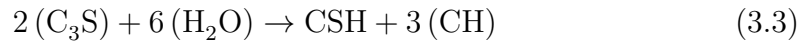
3.1.2 Cement hydration

The curing and hardening of concrete originates in a collection of coupled chemical processes between several successive cement minerals and H_2O , resulting in cementitious binders' formation. In this mechanism, the concrete goes from a liquid-like plastic state to a stone-like state, forming gels and new crystal structures. To better understand the curing process for concrete, it is thus essential to understand the chemical reactions between the four main clinker phases and water. Cement hydrogenation is divided into five phases; *Initial reaction*, *The Dormant Period*, *Accelerating phase* and *Retardation Period*, which are based on the main reactivity of the main clinker phases to H_2O . Since the cement hydrogenation process correlates closely with the temperature change, temperature changes are used to subdivide and track the different phases and processes. Furthermore, the division is based on pure independent components, which is a simplification of reality but illustrate the reaction process in a structured and transparent way^{[31] [32]}.

Initial reaction: In the first phase, tricalcium aluminate (Alite /C3S) and gypsum react with H_2O to form calcium aluminate hydrate, also called ettringite and precipitate CH. Reaction 3.2 shows the ettringite formation by reaction between Alite and H_2O . Ettringite forms a surface layer that covers the cement particles and forms a diffusion barrier for H_2O , preventing direct hydrogenation. The reaction occurs as soon as the cement comes in contact with water and is a very exothermic reaction where the release of energy causes a short and sharp temperature peak, as shown in Figure 3.2. The products from this phase contribute little to later durability or strength development^{[1] [33]}.



The Dormant Period: This period refers to the phase between the first immediate exothermic reaction and the phase where the concrete begins to harden. The ettringite formation dominates the phase as a coating on the cement particles. The formation of ettringite slows down the supply of H_2O in the inner layers of the cement particles, which results in slowing down the hydration reaction. Furthermore, the coating on the cement particles will gradually become thicker, which reduces the reaction rate of the cement hydration to a point where the *Dormant period occurs*. The resting stage is further characterised by minimal physical changes in the concrete since the remaining water in the surface layer increases hydrated product at the same time as the surface layer contains anhydrous products that keep the concrete in a liquid state. The resting stage is further identified by the reaction of silicates from Alite (C3S), and Belite (C2S) with water to form calcium hydroxides (CH) and calcium silicate hydrate (CSH). Equation 3.3 shows the reaction between C3S and H_2O to form CSH. The calcium silicates are formed as anhydrous soluble silicates, which result in the accumulation of hydroxide ions (OH^-) in the solution. The phase ends as soon as CSH and CH break through the germinated surface layer over the anhydrous cement^{[31][32][33][34]}.



Acceleration phase: The *Acceleration phase* is characterized as the beginning of strength development due to hydrogenation of the calcium silicates C3S and C2S to CSH. Equations 3.4 and 3.5 represent the hydrogenation reactions of Alite and Belite with reaction respectively to form calcium silicate hydrate (CSH) and calcium hydroxide ($\text{Ca}(\text{OH})_2$), where the first line in each reaction takes advantage of chemical reaction equation notation, while the second line uses cement notation. The formation of CSH can be categorised into two distinct forms, OP CSH (Outer Product) and IP CSH (Internal Product), which is based on where and when the product is formed. Furthermore, OP CSH and IP CSH differ in that OP CSH is a fast-forming product where the gel consists of many impure forms with a high density of pores, while IP CSH is a cleaner and denser version. The concrete's ability to withstand compressive loads depends on the density of the hydration product and is thus proportional to the increase in IP CSH. Since C3S has a faster reaction rate and is hydrogenated primarily to OP CSH, the start period of the *Acceleration phase* (phase 3) will account for most of the OP CSH production, which causes the majority of later strength reduction and chemical degradation of the concrete. The formation of IP CSH, which primarily results from the hydrogenation of C2S, develops more slowly due to the lower surface area and lower cement composition of C2S in the cement, which further results in less heat exchange than the hydrogenation of C3S. The *Acceleration phase* is thus divided into two phases where the hydrogenation of

C3S dominates the reactions in the first phase (phase 3), but the reaction of C2S predicts the majority of hydrogenation in the second phase. Since heat development is different for the hydrogenation of C3S and C2S, mapping the two periods will consequently be seen by detecting the temperature (Figure 3.2). Since the hydrogenation of the calcium sulphates forms calcium hydroxide (CaOH) as a bi-product, the *Acceleration phase* will be further categorized by an increase in pH^{[31] [32] [33] [34] [1]}.

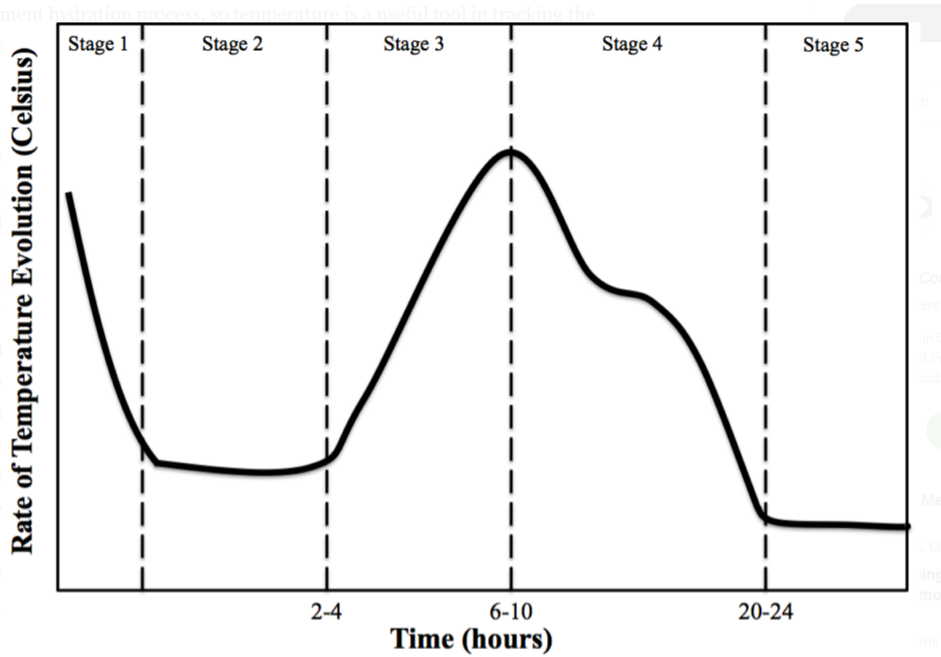
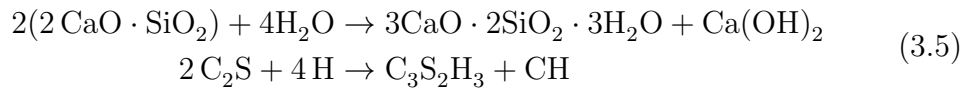
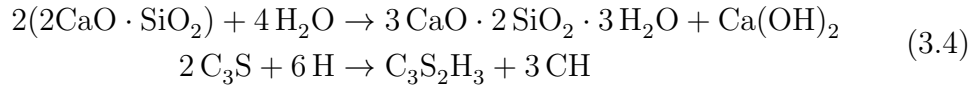


Figure 3.2: Temperature changes over time to highlight the various phases of cement hydration. Stage 1 is the *Initial reaction*, Stage 2 is the *Dormant period*, Stage 3 and 4 is the *Acceleration phase*, and Stage 5 is the *Retardation period*^[30].

Retardation period: In this phase, the reduction rate of CSH formation, mainly from C3S, will decrease due to lower diffusion. Nevertheless, CSH continues to bind to water and solids, which leads to a further reduction in porosity and consequently an increase in hardness. The period persists as long as H₂O and a sufficient amount of silicates are present and are standardized to last up to 28 days^{[1] [31] [32] [33] [34]}.

In addition to the primary components of cement hydrogenation, lesser amounts of bi-products will also be produced. Among these bi-products, AFm is one

($\text{Al}_2\text{O}_3\text{-Fe}_2\text{O}_3\text{-mono}$). AFm refers to hydrated calcium aluminates that do not form solid solutions and create distinct layered phases from a mineralogical standpoint. These layered phases can be separated into positively charged layers in water and a layer of charge-balancing anions^{[10] [35] [22]}.

3.2 Corrosion of metals

Corrosion is the primary chemical degradation mechanism in concrete structures and is the mechanism that poses the most significant challenge and reduces service life to the greatest extent. By forming oxide and hydroxide layers, corrosion breaks down pure reinforcements, which causes significant damage to the concrete structure. On the other hand, the right environment will cause the formation of passive layers, which consequently protect the metal against active corrosion. Therefore, understanding the corrosion process and the following consequences in concrete structures is of great importance. In this subsection, the general mechanism for forming oxide and passive layers is described before the relation between corrosion and pH is presented^[9].

3.2.1 Passivity and creation of an oxide layer

The passivity of metals is due to the formation of oxide and/or hydroxide layers on the metal surface at a reduced corrosion rate. Passive mono-layers of oxide are formed when the nucleation of oxides is adsorbed on an unaffected metal surface and occurs mainly in oxygen-rich or aqueous environments. The oxygen layer grows in a two-dimensional plane, illustrated in Figure 3.3, which shows the formation of a mono-layer formed by an oxide coating. The Reactions 3.6 (reduction), 3.7 (reduction) and 3.8 (oxidation) show half-reactions in the oxide or hydroxide layer process, while the total reaction is represented in Reactions 3.9 and 3.10^[36].

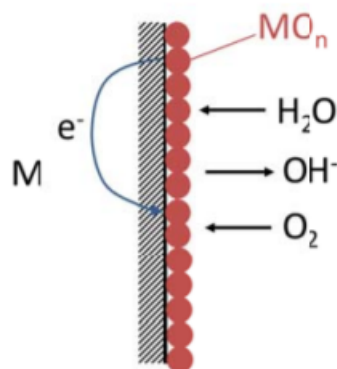


Figure 3.3: Illustration of mechanism for formation of the first monolayer of oxide^[36].

A further factor determining the three-dimensional bulk growth in the oxidation of metals is the conductivity of the oxide layer. If the oxide layer refers to insulating properties, a thin oxide layer will be formed, explained using the

Cabrera-Mott theory. The mechanism is illustrated in Figure 3.4. The reactions in forming such an oxide layer will correspond to the reactions 3.6-3.8, where MO_n is replaced by $MO_{n,ads}$ due to three-dimensional oxidation growth. The insulating properties of the oxide layer result in that the electrons formed at the metal-oxide interface are only transported at a limited speed to the oxide solution interface. In contrast, oxidized metals (MO_{ads}) are not transported. Due to the reduction reaction at the oxide-solution interface (Equations 3.6 and 3.7), an excess of O_2^- -ions will thus occur, which results in charge separation and creates a large electric field. As a result of the formation of the electric field, O_2^- -ions will migrate from the oxide-solution interface to the metal-oxide interface. Arrived at the metal oxide surface triggers O_2 Reaction 3.8, which results in the growth of the oxide layer at the metal-oxide interface. Aluminium is an example of a metal that forms such an oxide layer in a neutral environment^[36].

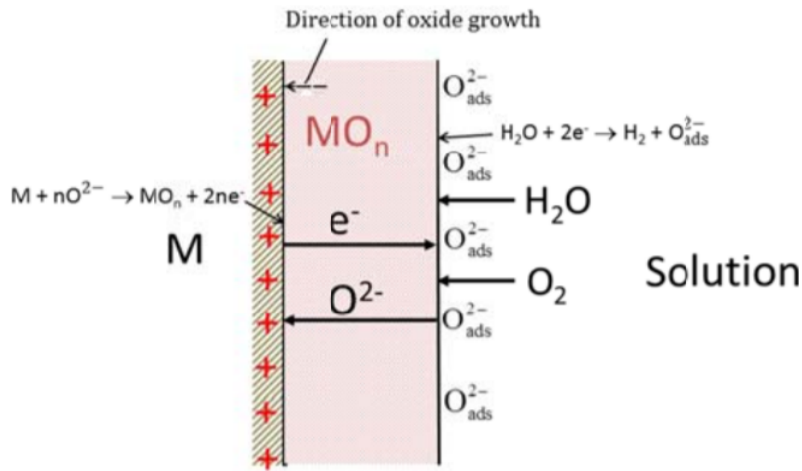
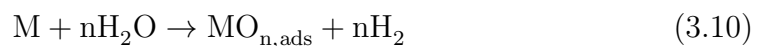
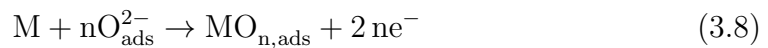


Figure 3.4: Illustration of mechanism for formation of bulk oxide with poor conductivity^[36].



If the monoxide layer has high conductivity, formed electrons and the metal ion (M^{2n+}) are transported from the metal-oxide interface to the oxide-solution interface. Arriving at the oxide-solution interface, the electrons and the metal ion react in a reduction- or hydrolysis reaction in contact with water H_2O and/or O_2 , respectively. The reactions are represented in 3.11-3.14, while the mechanism is illustrated in Figure 3.5. Products from the reactions lead to an active oxidation growth in the oxide-solution interface, resulting in a thicker oxide layer than the situation with lower conductivity. Steel is a metal that forms such a monoxide layer in a neutral environment^[36].

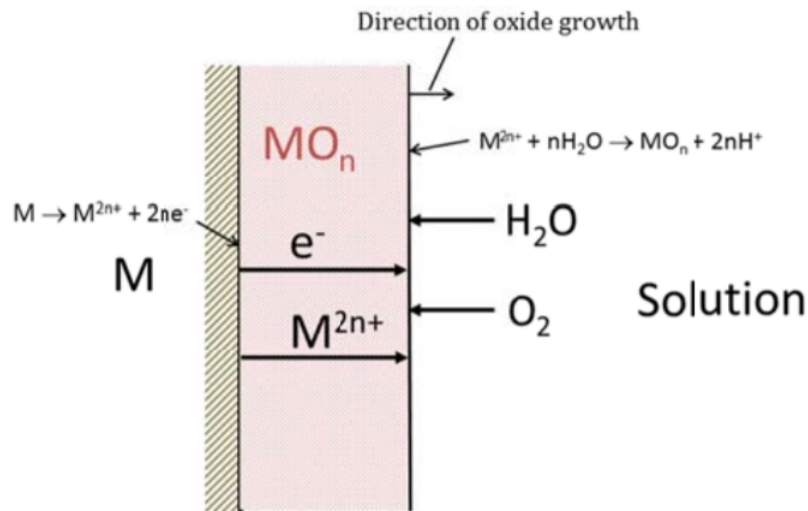
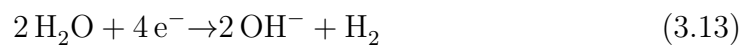
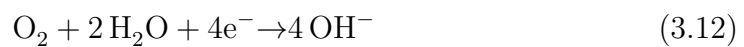


Figure 3.5: Illustration of mechanism for formation of bulk oxide with some conductivity^[36].



3.2.2 Variation of corrosion rate determined by pH of different metals

The corrosion rate of different metals depends on the pH of the corrosive environment. The corrosion rate measures the rate of oxidation reaction when a metal changes to a more stable oxide in an electrode reaction. The electrode reaction depends on the reduction potential of the metal and is consequently different for different metals. Since the electrode reaction of many metals in

the aqueous environment includes the ions OH^- and H_3O^+ , the extent of the electrode reaction depends on the pH. Using the Nernst equation, the electrode reaction and the corrosion rate will thus depend on the potential and pH, given in Equation 3.15. Different potentials and pH cause different metal phases to be thermodynamically stable. This can be seen in the Pourbaix diagram shown in the Appendix A.1. As metal phases have different passivity and resistance to further oxidation, corrosion will also be different. Consequently, metals with different electrochemical potentials will have different passivity and resistance and corrosion rates in different aqueous environments, depending on the pH of the aqueous environment. Figure 3.6 shows the corrosion rate with respect to the pH of the metals iron (Fe), zinc (Zn), lead (Pb), aluminium (Al) and copper (Cu)^{[37][36][38]}.

$$E = E^0 - \frac{R \cdot T}{F} \cdot \ln(10) \cdot pH \quad (3.15)$$

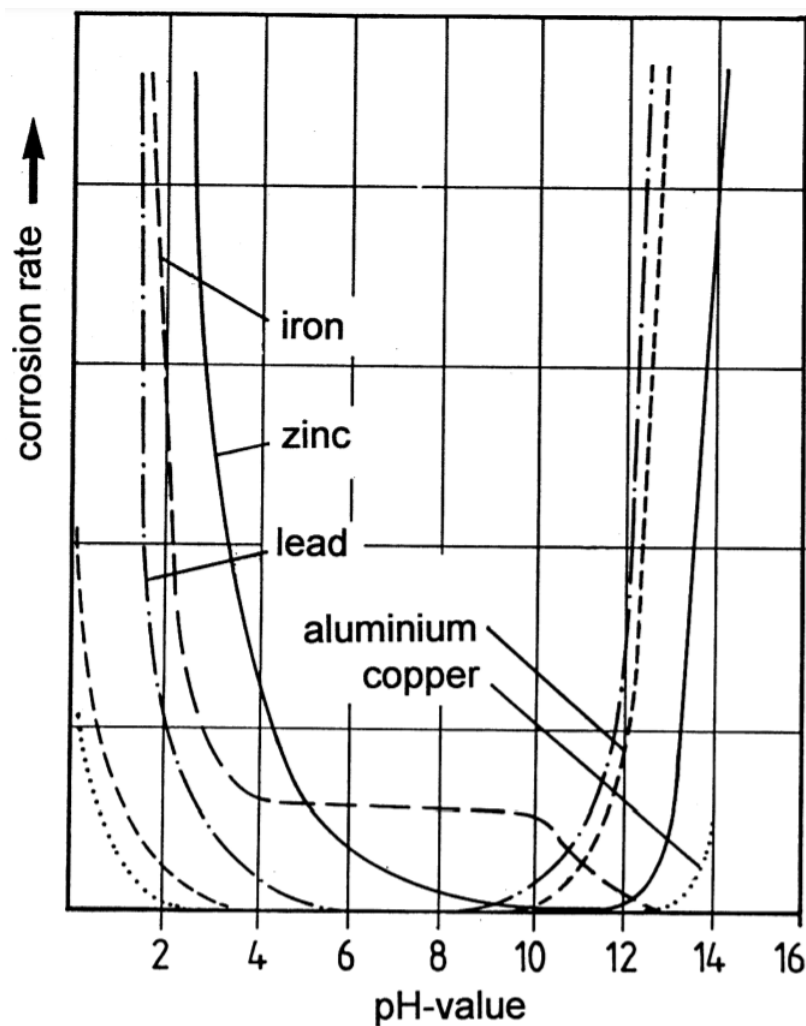


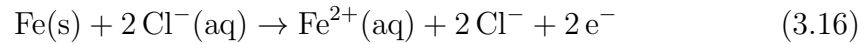
Figure 3.6: Correlation between corrosion rate and pH for iron (Fe), zinc (Zn), lead (Pb), aluminium (Al) and copper (Cu)^[38].

3.3 Degradation of steel reinforcements

Corrosion of reinforcing steel, which is the most often employed reinforcement material in modern times, is the primary cause of the early failure of reinforced concrete structures. Consequently, this causes a decrease in service life. Corrosion does not necessarily lead to the collapse of the concrete structure, but it does lead to cracking and delimitation, which contribute to the loss of structural use. Cracking and delimitation will result in costly repairs and diminished structural functionality. Globally, it is estimated that 100 billion dollar is spent annually on concrete infrastructure rehabilitation. To lower costs and extend the service life of concrete reinforcements, it is essential to understand the corrosion mechanisms in concrete structures better^[39][9].

3.3.1 Corrosion of steel reinforcements

Corrosion initiated by chloride (Cl^-) and carbonisation (CO_2) attacks is the decomposition mechanism that dominates in steel-reinforced concrete structures. Chloride corrosion is caused by Cl^- -ions from dissolved salt that diffuses from the external environment through the pore solution to the steel surface. The corrosion mechanism is shown in Reaction 3.16^[9].



Since Cl^- has a higher reduction potential than iron (Fe), the halogen will oxidise the solid Fe) and form an unstable Fe^{2+} -ion, which causes the formation of pitting corrosion in the steel. Corrosion predicted by carbonisation is due to diffusion of CO_2 into the concrete structure, which, when reacted with the hydroxide (OH^-), results in neutralisation of the cement paste. Furthermore, bicarbonates (HCO_3^-) are formed, which further lowers the pH. The mechanism is described in Reaction 3.17^[38].

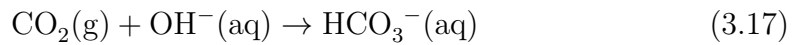
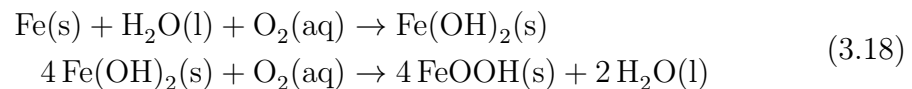


Figure 3.6 shows an increase in corrosion rate for Fe at $\text{pH} < 9$. This is due to the conversion of iron to iron(II)hydroxide ($\text{Fe}(\text{OH})_2$) by contact with oxygen (O_2) and water (H_2O) in neutral or slightly alkaline moist environments. Reaction with O_2 turns into rust, iron(III) (FeOOH)^[38][10]. The Pourbaix diagram A.2 further reflects the phase deviation the pH has on iron^[38][10].



The rust layer, shown in Reaction 3.18, results in active corrosion since the metal oxide does not have passive anti-corrosion properties^[38][36]. Active corrosion degrades the mechanical properties of the metal and consequently reduces the

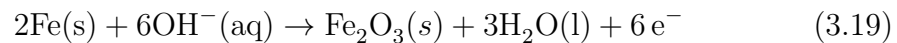
service life of the concrete structure. The service life is further reduced by a reaction between the hydroxide and diffused sulphate, which adds tensile stress by forming ettringite and gypsum, expanding the hardened concrete structure.

3.3.2 Preventing corrosion of steel reinforcements

Two solutions are employed to prevent corrosion of steel reinforcement and increase the lifetime of concrete constructions.

1. Increase the pH of the cement in order to passivate the steel^[9].
2. Implement a protective coating for the steel reinforcement in an extra-thick layer of cement with limited permeability^[9].

As shown in Figure 3.6, an alkaline environment with a high pH value will reduce corrosion rates. This occurs since OH^- reacts with iron Fe to make a passively protective Fe_2O_3 coating on the surface of the steel reinforcement, as shown in Reaction 3.19.



Due to the advantages of passive Fe_2O_3 coating formation in high pH conditions, substantial quantities of alkaline chemicals are added to Portland cement and other cement products. Consequently, concrete's pore water will be extremely alkaline, with a pH between 12.6-13.8. This results in a 2 to 20 mm thick Fe_2O_3 coating^[38].

While the first strategy focuses on extending the service life of concrete structures by developing protective layers, the second way aims to prevent Cl^- ions and CO_2 from interacting with the steel reinforcement. By reducing the permeability of the concrete and increasing the diffusion distance, the diffusion of the molecules is diminished. Thus, a permeability significantly lower than that required for the strength class is employed, and more cement is used than is mechanically required^[21].

CO_2 -emissions rise as a result of the increased utilisation of cement. This emission can be decreased by utilising a reinforcing material resistant to corrosion, carbonation, and chloride attack.

3.4 Aluminium as reinforcement

Aluminium and its alloys are sought after materials due to their exceptional weight-to-strength properties, corrosion-resistant and 100% recyclability. Aluminium is a widely distributed element that makes up 8.1% of the earth's crust^[40]. Due to these properties, aluminium and its alloys are attractive alternatives as reinforcements in concrete structures. Furthermore, it is essential to understand how the aluminium alloys are formed since the production determines the corrosion properties of the alloys.

This subsection looks at how aluminium alloys are made and how the treatment affects the corrosion properties of the resulting alloy.

3.4.1 Cast and wrought alloys

On a regular basis, aluminium alloys are divided into cast and wrought alloys, which are distinguished based on the manner in which the alloy is manufactured due to its formability. The primary shape of cast alloys is established by the casting process, whereas wrought alloys are created through plastic processing. Cast alloys have brittle qualities with a high degree of shape, while wrought alloys are ductile and create symmetrical shapes. In practise, however, this distinction is not straightforward, as many aluminium alloys can be produced into both casting alloys and wrought alloys. Although 4xxxAl alloys are normally accessible as cast alloys, they are like 6082 alloys treated by extrusion in this master's thesis and hence designated as wrought alloys. The thesis will therefore start by introducing the manufacture of cast alloys before delving further into extruding wrought alloys^{[41][42][43]}.

3.4.2 Production of aluminium alloys

Production of cast alloys

Casting is a production process based on solidifying liquid metal that becomes poured in a form or negative imprint. The solidification is due to the cooling or chemical reaction of the melted metal. Since the form or negative imprint directly gives the desired complex shape to the end product, casting is cost-effective compared to other production methods. Cast aluminium will often be highly alloyed to improve cast ability, minimize casting defects, and strengthen aluminium^{[44][45]}.

Production of wrought alloys by extrusion

Extrusion is one of the most widely used processing methods for wrought aluminium alloys. It is a technique that transforms the aluminium alloy into products with a constant cross-sectional profile with a high potential for use. Before the extrusion process begins, the base material becomes the extrudate; the extrusion blocks are formed. For aluminium alloys, the extrusion blocks are usually produced by direct cooling (DC), in which liquid metal is poured into a water-cooled mould for casting by opening the bottom of the mould. This results in the outer layer of the metal solidifies. The solidification process is then completed by spraying water directly on the newly formed blocks, which results in a solid block^[46]. Hot extrusion is the most widely used extrusion method for aluminium alloys. Hot extrusion is a thermomechanical process (TMP) in which the preheated material is forced through a shaped preheated nozzle. The nozzle is preheated to prevent metal from sticking to the nozzle and causes the metal to become flexible enough to carry out the extrusion while maintaining the solid stage. Furthermore, heating the extrusion blocks below solidus temperature will

improve the extrusion blocks' extrudability and mechanical properties by homogenising and removing grain boundaries. When heated, the alloy composition will also be essential.

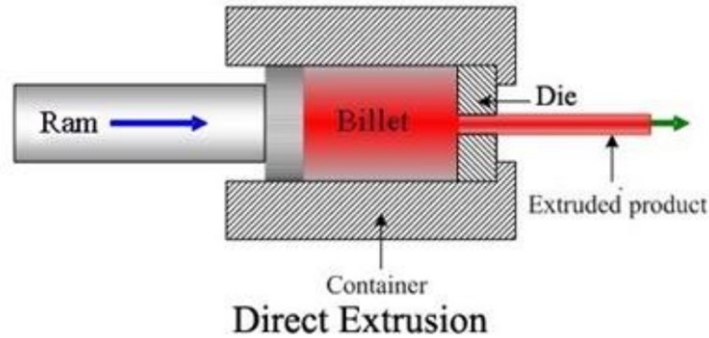


Figure 3.7: Illustration of hot direct extrusion^[47]

The extrusion is carried out by applying pressure either by direct or indirect extrusion. For indirect extrusion, the pressure is applied by the piston moving toward the ingot, while the nozzle moves towards the ingot by indirect extrusion. Direct extrusion is illustrated in Figure 3.7^[47]. As a result of the pressure, the solid metal will be pushed out through the opening of the nozzle and come out on the other side as a fully formed profile with a uniform shape and density^[48]. After the hot extrusion, the extrudate will be cooled in an oxidizing environment either by quenching with water or air cooling. This cooling process is a critical step in the production process and significantly impacts the metallurgical properties. The metallic properties can be further modified by precipitation hardening or age hardening. Figure 3.8 depicts the whole process of alloy manufacture, from ingot to final product.

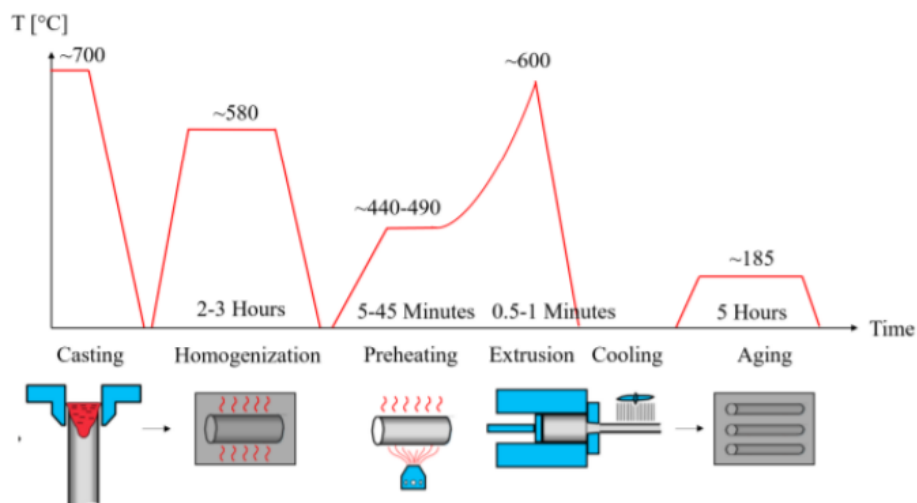


Figure 3.8: Aluminum alloy extrusion manufacturing process^[49]

3.4.3 Hardenable and non-hardenable alloys

In addition to distinguishing between cast and wrought alloys, alloys are categorised into hardenable and non-hardenable alloys. Hardenable alloys are strengthened by heat treatment, while non-hardenable alloys increase the strength of the material by mechanical cold working and deformation hardening. In the heat treatment of hardenable alloys, a subsequent heating and quenching operation will result in precipitation hardening, which gives the metal product the desired properties by changing the metal's metallurgical structure and metallic properties. However, for aluminium alloys, the term is limited to operations to increase the hardness and strength of the precipitable hardenable cast and forged alloys^{[41][50][43]}.

3.4.4 Heat Treatment by aging

One of the advantages of using aluminium alloys is that many are hardenable alloys when the proper condition is in place. The most common method of hardening the alloys is by aging.

Metal aging is one of the most common ways to change metal alloys' physical and aesthetic properties. In this process, hardening intermetallic alloying elements are precipitated in the supersaturated solid solution phase of metal alloys which further blocks displacements in the metal and thus increases the hardness and strength of the metal alloy while reducing the ductility. Metal aging is divided into natural and artificial aging processes, where natural aging takes place at RT throughout the life of the metal alloy. In contrast, artificial aging accelerates the formation of precipitates by heat-treating the metal alloy. This results in a higher hardness and strength level than for natural aging. In artificial aging, the temperature of the solution heat-treated metal alloy is increased to a point where the precipitation forms, but which is below the crystallisation temperature. At the correct size of the alloying element deposits, the metal alloy cools to counteract further changes in the metal alloy.

Due to the mentioned mechanical changes and increased corrosion resistance, artificial aging of aluminium alloys will be advantageous. Artificial aging occurs in air furnaces at temperatures between 100 and 208 °C, depending on the aluminium alloy composition. As with other metal alloys, heavy precipitation and hardening elements in the form of intermetallic compounds will occur during the artificial aging of aluminium^[51].

3.4.5 Aluminium alloys microstructure

Dendritic microstructures are produced during the solidification of aluminium alloys. The structure results from two mechanisms: precipitation from a supersaturated solid solution during cast cooling, resulting in dendrites with very fine needle-like precipitates, and local concentration segregation's at the liquid-solid interface, forming a solidification front by liquid adsorbed on the particle and

solidifying.

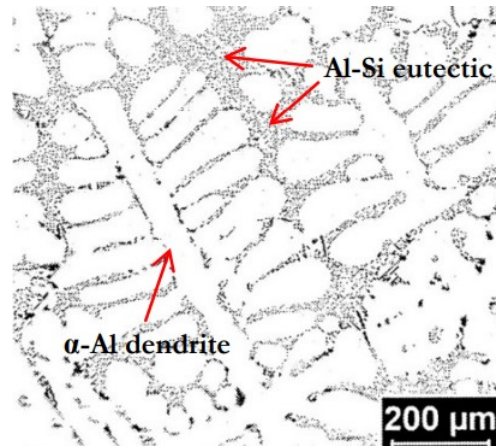


Figure 3.9: Solidification microstructure of Al-Si alloys [52].

Figure 3.9 depicts the microstructure of a cast Al-Si alloy. The irregular lamellar eutectic microstructure derives from the structural components α -Al from solid solution dendrites and Al-Si formed interdendritic eutectic mixture (red arrows). In addition, the β -Al solution produces dendrites from extremely thin needle-like precipitates. The majority of the particles are uniformly dispersed. In contrast, the silicon in the aluminium casting alloy can be found as either fine dendrites or coarse crystals. Due to the anisotropy of the Si growth and the low interface energy between Si and Al, the massive, coarse, lamellar-like plates of Si in the eutectic aluminium structure lead the alloy to be brittle. The ductility of the Al-Si alloy is also governed by the Al dendritic grain size and the morphology of Si particles, where large grain scatterings of Al lead to elongated Si particles with acicular morphology, resulting in poor ductility [53] [54]. Small alloy particles influence the microstructure of aluminium alloys by altering the intermetallic phases during solidification. The addition of impurities like Fe or alloying elements like Mg causes eutectic and peritectic reactions in the alloy. This produces intermetallic phases such as Fe- and Mg_2Si -containing phases [55] [56]. The development of β -AlFeSi is the most detrimental of the intermetallic phases since it impacts the mechanical and casting characteristics of the alloy by creating massive, brittle platelets. Mg and Mn are added to avoid the development of the β -phase and boost the strength of the alloy. The inclusion of Mg causes Mg_2Si particles to precipitate in the matrix, enhancing the strength. Additionally, the inclusion of Mg will result in forming a harmless phase and enable the age hardening of Al-Si alloys [57]. The inclusion of Mn decreases the solubility of Si and Fe in the matrix, modifying the shape and composition of Al-Fe-Si phases by favouring the production of $\text{Al}_{12}(\text{Fe},\text{Mn})_3\text{Si}$ phases over the detrimental Al_5FeSi phase. In addition, large concentrations of Cu in the aluminium matrix will boost the alloy's strength because aging or precipitation hardening leads to the production of Θ - Al_2Cu , S- CuAlMg_2 , and Q- $\text{Al}_5\text{Cu}_2\text{Mg}_7\text{Si}_7$ phases, which generate dislocation movements and reduce sliding planes. In contrast, the ductility and corrosion re-

sistance of the alloy would decrease as the copper percentage increases^{[53][58][59]}. In addition, minor alloying elements like Na, Sr, and Ca function as modifiers and inhibit the production of primary Si crystals, resulting in a more nuanced distribution of the lamellar eutectic Al-Si structure^[60]. In contrast, the addition of P will result in the synthesis of AlP in an intermetal phase, resulting in the creation of fine-grained microstructures after solidification^[61].

3.4.6 Microstructure extrusion

In contrast to castings, plastic deformation throughout mechanical processing reinforces wrought alloys, resulting in significantly enhanced mechanical properties. This reinforcement for wrought alloys results from a higher density of lattice defects. Furthermore, high alloy casting alloys will be more challenging to process. The alloys will thus usually use lower alloy additions.

As the extruded microstructure, especially grain size, has such a significant impact on the resulting mechanical properties of wrought alloys, it is necessary to consider how the microstructure evolves in the extrusion process both during and after deformation.

The pressure via the nozzle causes plastic deformation during the actual extrusion process. In addition, coarse intermetallic particles will be aligned in the direction of metal flow, making them more stringent and fragmented. The microstructure throughout the extrusion sample is depicted in Figure 3.10. Since the increased lattice stresses are caused by the increased specific surface area of the smaller particles, the internal energy will likewise increase. This will change the metal's microstructural development^[62]. Extrusion can also result in an anisotropic microstructure that changes extrusion directions over the profile. The anisotropic microstructure is the consequence of forcing a considerable volume through a narrow tool. This pressure induces the crystal structure to arrange in the desired orientations along with the extrusion. In addition, grain structure might become elongated. Moreover, high temperature, friction and large deformation when in contact to the tool during extrusion make it thermodynamically favourable for the outer peripheries to recrystallize in a thin layer since temperature and deformation are most significant at the material's outer layers. This leads to the strain field depicted in Figure 3.10.

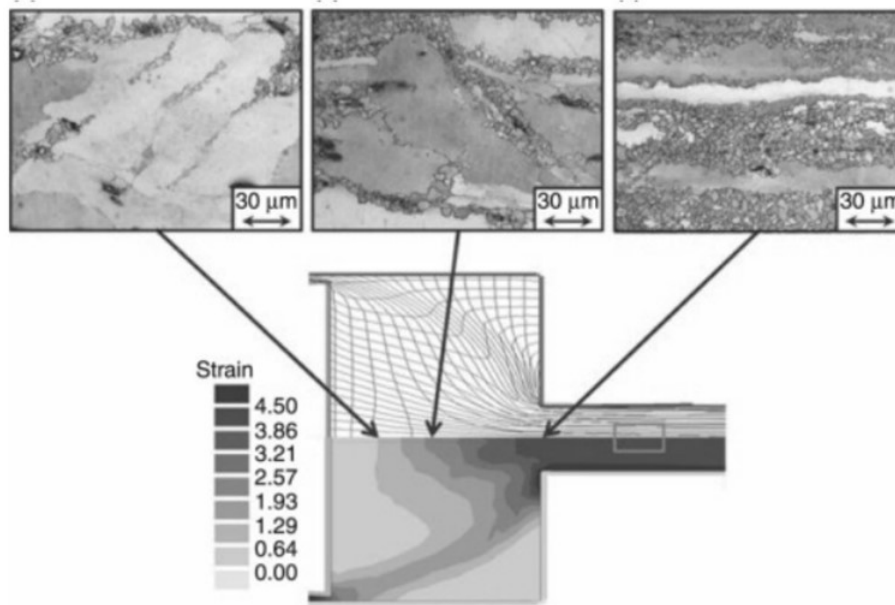


Figure 3.10: Illustration of strain field and subsequent microstructure during extrusion^[62].

Upon application of plastic deformation, the majority of energy will be transferred to heat. At the same time, a small percentage will create defects, which will increase the deformed metal's internal energy. The stored energy and dislocation density (and its distribution) rely on a number of variables, including the metal itself, its purity, grain size, and the quantity, mode, temperature, and rate of deformation. Due to the emergence of internal energy, the metal will no longer be in thermodynamic equilibrium. Hence, the metal will seek to decrease its energy by settling at a lower energy level to counterbalance the newly produced internal energy.

Recovery, recrystallising and performing grain growth, makes it possible to decrease the inner energy^[63].

The internal load energy from the previously cold-worked metal is restored upon recovery. Furthermore, the physical properties of the metal, such as thermal and electrical conductivity, are restored. During recovery, some of the stored internal charge energy is relieved by dislocation motion due to increased atomic diffusion. Recovery occurs in two ways, either statically when the metal is heated or dynamically due to stress and subsequent deformation at high temperatures. Since stacking fault energy SFE is directly proportional to the dislocation mobility, a high degree of (SFE) will result in easier recovery, which reduces the number of lattice defects. Recovery is depicted in Figure 3.11^{[63][64]}.

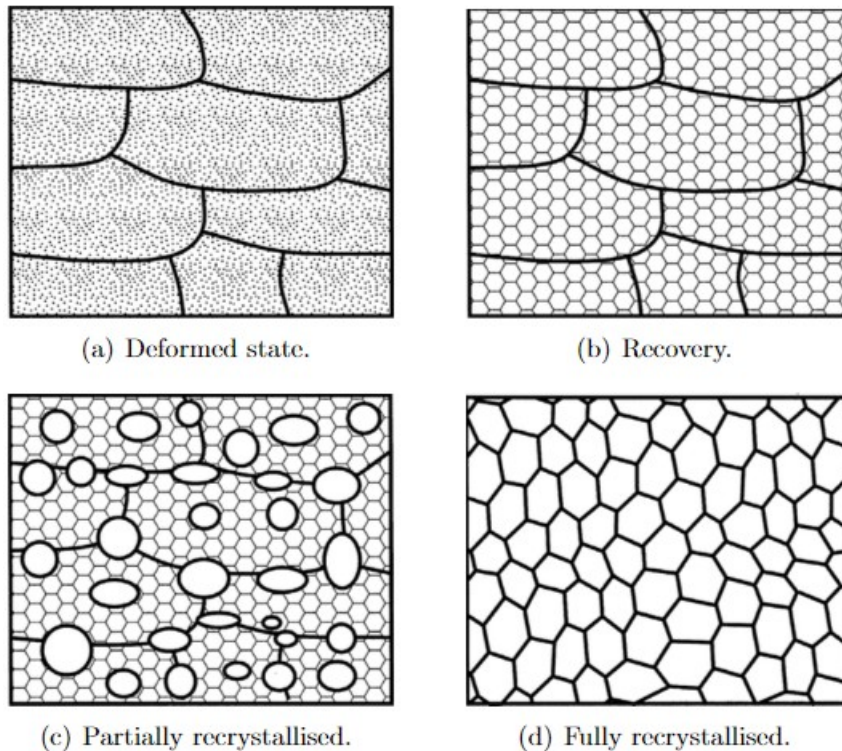


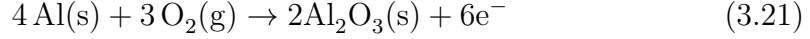
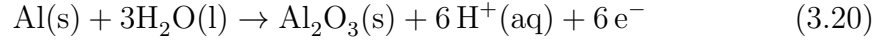
Figure 3.11: Illustration of recrystallisation sequence^[65].

Recrystallisation is the formation of new, tensile-free, equiaxed grains, which reduces defects and results in a material with a decreased dislocation density^{[64] [63]}. Recrystallisation arises when the deformation and temperature are high enough to be thermodynamically favourable for developing nuclei of new solid phases in the metal. Upon completion of crystallisation, grain growth occurs since the microstructure of the newly formed recrystallised grains retains internal energy and is thus not entirely stable. Growth of grains may be continuous or discontinuous, with continuous growth resulting in average grain size. Meanwhile, discontinuous convexity causes a few grains to accelerate. Therefore, discontinuous convexity is often referred to as secondary recrystallisation^{[64] [63]}.

3.5 Corrosion of Aluminium

3.5.1 Formation of an oxide layer on aluminium

Aluminium has considerable corrosion resistance despite its relatively low standard electrode potential of -1.68V ^[66]. The metal will create a thick layer of Al_2O_3 in a sticky amorphous oxide film in a neutral to a slightly acidic environment and moist air. By acting as a passive coating, this layer functions as a barrier against additional corrosion^[36]. Unlike steel, the aluminium covering will repair itself after being damaged mechanically. When solid Al reacts with H_2O or O_2 , the chemical processes that result in Al_2O_3 are shown in Reactions 3.20 and 3.21, respectively.



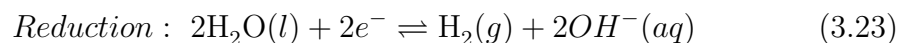
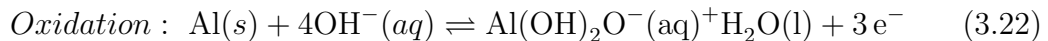
In contrast to the steady circumstances of alumina in air, the oxide coating in water will be unstable and undergo many alterations. $\text{Al}_2\text{O}_3\text{(s)}$ will be changed to pseudo-boehmite (AlO(s)) in the first phase before being transformed into bayerite crystals ($\alpha\text{-Al(OH)}_3\text{(s)}$) in the second phase. Boehmite (AlOOH(s)) can also occur due to higher temperatures. Figure 3.12a shows a picture of Boehmite taken with SEM.

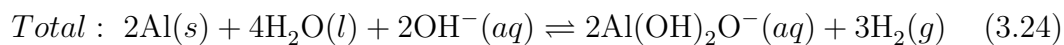
Creating an amorphous black and porous oxide/hydroxide layer when Al_2O_3 comes into contact with H_2O is another mechanism that can occur. This is referred to as blackening^[67]. Alloy elements in aluminium have an impact on the oxide layer's stability. The alloy metals will either increase or reduce stability due to the varying electrochemical characteristics of the individual metals in the alloy. When new stable oxides are generated, they increase the stability by either shield the metal surface or interact with existing aluminas to improve stability and resistance of the alloy.

When the electrochemical characteristics of the alloys are sufficiently dissimilar, the passive layer is reduced resulting in intergranular corrosion, exfoliation, or stress corrosion fractures development^[36]. Si and Mg are two alloys that improve the resistivity of the protective oxide layer. Because Mg and Si are on each side of Al in the periodic table, their chemical characteristics will be similar. This indicates that SiO_2 and MgO can be mixed with Al_2O_3 to increase the alloy's passivity. Cu is one example of an alloy that decreases the passivity of an Al surface. The presence of Cu in Al alloys reduces the durability of the oxide coating due to considerable variations in atomic structure and chemical characteristics between Al and Cu^{[68][69]}.

3.5.2 Corrosion of aluminium in strong alkaline environments

In strongly alkaline environments, aluminium loses its corrosion resistance, observable by following the aluminium corrosion rate line in Figure 3.6. Because aluminium is an amphoteric metal, and hence can react both as an acid and base, the protective coating will dissolve when exposed to very acidic or alkaline substances. In a highly alkaline environment, such as OPC, alkali hydroxides will remove the Al_2O_3 layer, resulting in additional corrosion^{[9][38]}. Reactions 3.22-3.24 shows the the active corrosion mechanism for Al in strong alkaline environments.





Under these conditions, aluminium metals will be as active as their position on the Galvanic series (-1.68 V) suggests. They will cause active corrosion by making hydrogen and highly soluble aluminates, even without oxygen. Moreover, $\text{Al}(\text{OH})_2\text{O}^-$ -ions in contact with H_2O can precipitate as Gibbsite $\text{Al}(\text{OH})_3(s)$ at the interface between aluminium and cement, distinguishable as a white corrosion product. Figure 3.12b shows a picture of Gibbsite taken with SEM.

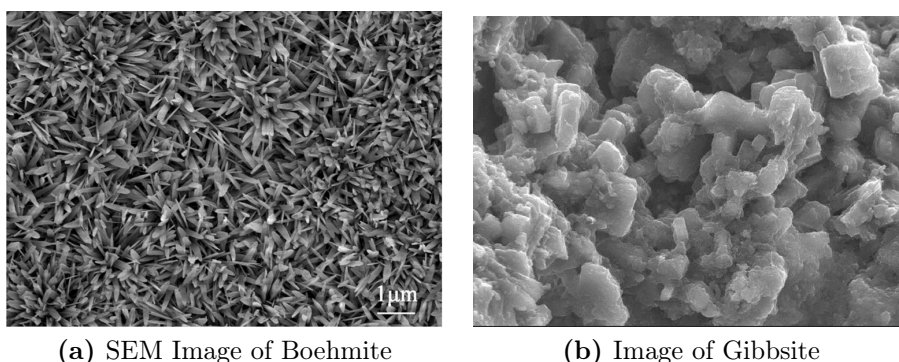


Figure 3.12: Images of morphology of Boehmite and Gibbsite^{[70][71]}.

3.5.3 Pitting corrosion

Pitting corrosion is the most common type of corrosion in aluminium alloys. The process is caused by aggressive ions (anion or cation), which degrade the protective oxide coating, leading to local corrosion. There are two phases to the corrosion process: the *Initiation phase* and *Reproduction phases*.

During the *Initiation phase*, ions such as the chlorine ion (Cl^-) will replace the O atom in the oxide layer and trigger breakdown. The replacement of the O atom with the Cl^- -ion is due to the adsorption of Cl^- at localized inhomogeneous locations on the surface of the outer layer of the film^[72]. This adsorption can be explained by the point defect model, which postulates that the Cl^- -ions are integrated into the passive inhomogeneous film by migrating to and filling unoccupied anion sites with a positive potential^[73]. Reduction in free anions leads to an increase in cation-free spaces, which, when accumulated at the metal interface, results in the film's collapse. Inhomogeneous oxide layer will thus be more prone to pitting corrosion. Thus, pitting corrosion will be more common along grain boundaries and intermetallic phases.

During the *Reproduction phase*, aluminium oxidizes to aluminium ions, resulting in the creation of a pit. After the oxide layer has been broken and pit nucleation has occurred, owing to the dissolution of metal ions, the oxidation of aluminium ions at the bottom of the pit will result in a decrease in pH, as seen by Reaction 3.25. As the Al^{3+} -ions undergo hydrolysis, the generated aluminium hydroxide

Al(OH)_2^{2+} will react Cl^- and subsequently with H_2O , resulting in acidic conditions. The acidic conditions at the bottom of the pit will result in the diffusion of Cl^- ions, which will lead to the creation of a salt film and an acceleration of the dissolving process^[74]. The Cl^- -ion diffusion capability will thus regulate the mechanism. At the edges of the pits, the aluminium chlorides will be hydrolyzed into the aluminium hydroxide Gibbsite $\text{Al(OH)}_3(\text{s})$. The development and position of Gibbsite will diminish the diffusion opening, hence decreasing the chloride ion supply. Eventually, this will block ion exchange and end the corrosion process^{[68][75]}. Figure 3.13 illustrates the pitting mechanism graphically^[76].

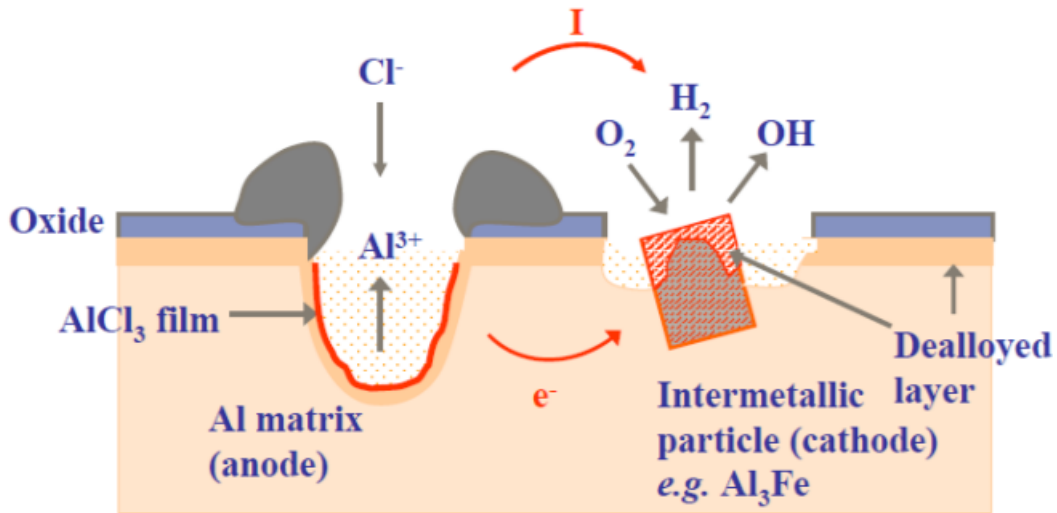
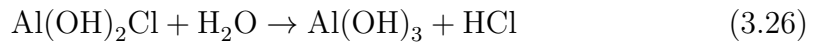
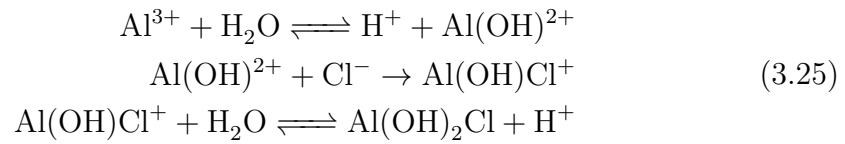


Figure 3.13: Mechanism for pitting corrosion in aluminium alloys (left) and creation of a rough surface at intermetallic interfaces (right)^[76].

3.6 Innovation of a paste suitable with aluminium

When developing a cement paste compatible with aluminium reinforcements, it is essential to prevent reinforcement corrosion, which causes the most significant challenge in service life and mechanical defects in the concrete structure. Central to the development of cement paste for aluminium reinforcements will thus be to reduce the pH, which results in a protective effect. According to Justnes^[9], implementing cement with pozzolanic SCM will be the industry's fastest and most straightforward approach.

This section presents the formation of a cement paste that is compatible with aluminium reinforcements by presenting SCMs and their classification before illustrating the SCM mechanism in a cementitious environment. In addition, CC and hyaloclastite are suggested as possible candidates for use in concrete structures. At the end, calcium chloride (CaCl_2) is provided as a potential additive in cement compositions with inhibitive qualities.

3.6.1 Supplementary cementitious materials (SCM)

Supplementary cementitious materials (SCM) are soluble mineral addition powders consisting of aluminium-containing, silicon-containing or calcium-aluminium siliceous materials that can replace the clinkers in cement in concrete structures^[77]. Many of the SCMs used today are bi-products from other industries or natural minerals, consequently having a much lower energy consumption in the production than Portland cement. The use of SCMs avoids the additional clinking process necessary for forming cement clinkers, which leads to a significant reduction in CO_2 -emissions^[78]. By comparing the thermal energy of production for Portland cement clinkers with calcination of kaolinite clay to metakaolin SCM, the formation of metakaolin SCM uses 0.35 GJ/h. In comparison, the production of the cement clinkers uses 3.5 GJ / h. Thus, the calcination of kaolinite is only 10% of Portland cement clinker^[79]. Furthermore, the energy in the production of SMCs that are uncalcined natural pozzolans or fly ash will be even lower^[80].

In addition, the replacement of cement material per concrete unit leads to an increased production volume for the cement plant and, consequently, a reduction in CO_2 -emissions. An additional advantage of using SCMs in concrete structures is that the resistance to degradation mechanisms increases compared to Portland cement at an equal water-to-cement ratio (w/c). A degradation mechanism where this does not occur is carbonation, which can be counteracted by reducing the w/c ratio^[9]. Due to the advantages mentioned above, the use of SCM as a partial clinker replacement is considered the CO_2 reduction strategy with the lowest performance and economic impact on cement and concrete production^{[81][82][83]}.

3.6.2 Classification of SCMs

SCM is divided into two main categories; latent hydraulic and pozzolan, based on the reaction of the material.

Latent hydraulic SCMs consist of inorganic compounds, forming cementitious binders directly with water (H_2O) upon activation. SMCs with latent hydraulic properties will be, for example, painted, granulated blast furnace slag (GGBS), high-class liquid and synthetic calcium aluminate glass^{[8][84][85]}.

Pozzolanic SCMs are minerals which form the cementitious binders calcium silicate hydrates (CSH) and calcium aluminate hydrates (CAH) by reaction with CaO and moisture. Pozzolanic minerals are found both naturally and synthetically. Examples of the occurrence of naturally pozzolanic minerals are in clayey

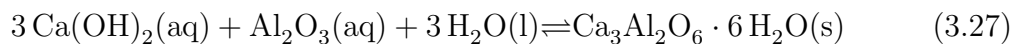
soils and bauxite, volcanic tuffs and diatomaceous earth. Synthetic pozzolanic minerals come mainly from industrial bi-products such as rice ash, silica fume and liquid. Pozzolanic SCM is further categorised based on the material's main oxide in alumina, silicates and aluminosilicates. SCM carbonates are categorized into a separate class, although they are pozzolanic SCMs, due to the mineral's dependence on aluminate hydrate (AH) to react. Since there usually are relatively small amounts of aluminate that are not bound to sulphates in cement clinkers, it has previously been challenging to observe the carbonate reactivity, leading to carbonates only recently being categorized as SCM^[86]. The effect of SCM carbonates was first observed in ternary systems at a macro level as the addition of flight fluid led to a further increase in strength due to the formation of calcium carbonates^[87].

3.6.3 SCM mechanism

SCM influences the hydrogenation of composites and mixed cement by having a "filler effect"^[88] and by forming a chemical reaction to form hydrogenation products in the form of (meta)stable hydrates^{[78][89]}. The chemical reaction performs a solution precipitation mechanism, in which the resulting hydrogenation products are similar to those formed during the OPC hydrogenation. This is because SCM and OPC consists of the same chemical elements.

Nevertheless, compared to cement hydration, hydration from SCM has a slower reaction rate. A high pH and OH^- concentrations activate both latent hydraulic and pozzolanic SCMs. Consequently, $\text{Ca}(\text{OH})_2$ will act as a buffer in this reaction where depletion of $\text{Ca}(\text{OH})_2$ leads to a decrease in pH in the pozzolanic reaction. As mentioned in Subsection 3.6.2, the difference between latent hydraulic SCM and pozzolanic SCM is the reaction with $\text{Ca}(\text{OH})_2$. Since the development of compressive strength prefers pozzolanic SCM, the use of this SCM will be advantageous^{[8][23]}.

Alumina (Al_2O_3) and silica (SiO_2) are the subgroups of pozzolanic SCM with the most significant reactivity. Reactions 3.27 and 3.28 represent the reactions between Al_2O_3 and SiO_2 with H_2O and $\text{Ca}(\text{OH})_2$, respectively.



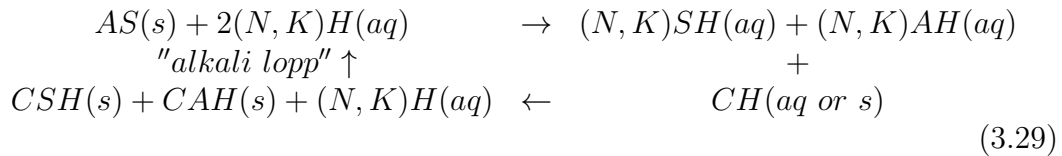
The Reactions 3.27 and 3.28 show a tripling in molar bonding with $\text{Ca}(\text{OH})_2$ and H_2O for Al_2O_3 compared to SiO_2 . Consequently, high Al_2O_3 pozzolanic SCM is recommended for maximum effect. Furthermore, the bonding difference to the H_2O increases considerably when carbonate or sulphate is added to the alumina environment.

Pozzolanic SCM consumes formed calcium hydroxide ($\text{Ca}(\text{OH})_2$), produced by hydrogenation of clinker materials in Portland cement, which results in a reduc-

tion in pH and passivation of the aluminium reinforcement. Aluminium silicate (AS) is the most common SCM in calcined clay.

Reaction 3.29 describes the chemical reaction between alkaline cement and SCM. Cement card hand notation is used to describe reaction, where $A = Al_2O_3$, $S = SiO_2$, $N = Na_2O$, $K = K_2O$, $H = H_2O$ and $C = CaO$. The reaction starts with the alkali hydroxides((N,K)H) being dissolved by the aluminosilicate(AS) of the individual components, aluminium((N,K)AH) and silicon((N,K)SH). Furthermore, the dissolved aluminium silicate reacts with calcium hydroxide(CH), resulting in amorphous calcium silicate hydrate (CSH) and crystalline calcium aluminium oxyhydrate (CAH), which acts as a binder in the cement paste. After the oxides and calcium hydroxide reaction, the alkali hydroxides are regenerated to proceed.

It is thus essential to have an excess of SCM compared to $Ca(OH)_2$ (CH) to prevent corrosion so that stable aluminates and silicates are formed when soluble alkalis react with aluminium or calcium ions. Studies have shown that SCM should replace at least 35% of the cement to create passive reinforcement of aluminium^[8].



3.6.4 Calsined clay (CC)

Clay is the most common sediment on Earth and is composed primarily of fine-grained minerals and phyllosilicates, which harden and acquire a flexible quality upon drying or burning^[90]. Clay minerals typically have a size 2 μm , and clay calcination at 600-800°C results in significant pozzolanic activity and active metastable material production. The chemical composition and specific surface area of mineral clay grains determine the reactivity of pozzolanic clay. The quantities of Al_2O_3 and SiO_2 assess the reactivity of clay, as mentioned in sub Section 3.6.3. Moreover, the particular surface area of the mineral clay granules plays an essential effect in the reactivity. A smaller grain size results in a larger specific surface, giving the clay a larger surface to react on^{[91][92]}.

3.6.5 Hyaloclastite

Hyaloclastite is a volcanoclastically hydrated tuff-like breccia. Hyaloclastite is formed by volcanic eruptions under glaciers, ice sheets, subterranean currents in the ocean or other bodies of water when the magma is not hot enough to melt through the overlying cooling mass and solidify. Hyaloclastite can have an amorphous and crystalline form and usually exists as a combination of these structures. Minerals found in the hyaloclastite mass include palagonite, olivine,

pyroxene, magnetite, quartz, hornblende, biotite, hyper store, plagioclase and calcite, which depend on the type of lava, the amount of lava fragmentation and the cooling rate of the individual mass. Hyaloclastite deposits are found worldwide, including in Alaska, Hawaii, British Columbia and Iceland. Furthermore, hyaloclastite is deposited in the world's oceans on sea mountains and the resulting oceanic islands, found on the mid-Atlantic ridge, among other places.

Since the chemical properties of hyaloclastite depend on the level of silica and alkali, the volcanic mass is classified based on the content of these minerals. Hyaloclastite is grouped into basaltic, intermediate, andesitic, dacitic and rhyolitic from low to high silica levels. The basaltic hyaloclastites are classified into the alkaline synthesis levels of tholeiite, intermediate and alkaline.

Research has shown that hyaloclastite acts as SCM in concrete structures^[19]. Although hyaloclastite does not work as hydraulic cement, it will be activated by $\text{Ca}(\text{OH})_2$ produced by hydration of hydraulic cement, such as OPC (Subsection 3.1.2). Furthermore, the size of the hyaloclastite powder leads to the pozzolanic properties of the volcanic deposit. In addition, mixing hyaloclastite and cement will increase the cement core formation process resulting in an accelerating cement hydration process, short curing time, accelerating hydration and previous compressive strength. This is due to the particle size of hyaloclastite and the crystalline and chemical composition of the volcanic deposit.

A advantage of using hyaloclastite as SCM in concrete structures is that the material does not have to be calcined before use, which means less energy consumption in the production process and a more environmentally friendly concrete product^{[19][20]}.

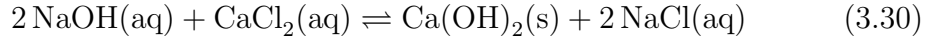
3.6.6 Calcium chloride (CaCl_2)

Calcium chloride is a white inorganic compound with high solubility and the chemical formula CaCl_2 . The salt is used to de-ice roads and preserve food^[93].

One of the drawbacks of using SCM to substitute significant cement components is that the concrete's early strength is reduced. As a result, the inclusion of a hardening accelerator will be required. CaCl_2 has previously been employed as a hardening accelerator since it was the most cost-effective and efficient option.

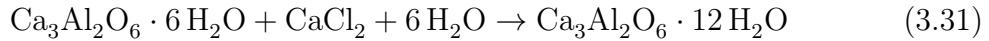
The accelerating qualities are attributed to the soluble calcium ions (Ca^{+2}), which result in an earlier supersaturation of $\text{Ca}(\text{OH})_2$, which further commences the *Acceleration phase* (Section 3.1.2). Experiments have also revealed that Cl^- ions exhibit accelerating capabilities, albeit the cause remains unknown. CaCl_2 has been outlawed as a hardening accelerator in concrete constructions in recent years, mainly to chloride corrosion on steel reinforcement. This will no longer be a concern when aluminium reinforcements are applied since the metal is more resistant to chlorides^[94].

Another benefit of utilizing CaCl_2 is that it lowers the pH of alkaline solutions, reducing the corrosion of aluminium reinforcements. As shown in Reaction 3.30, this is due to the common ionic effect of CaCl_2 and $\text{Ca}(\text{OH})_2$.



Ca^{2+} -ions from dissolved $\text{CaCl}_2(\text{aq})$ react with the OH^- -ions to form crystalline $\text{Ca}(\text{OH})_2(\text{s})$, decreasing the pH of the solution. The solution becomes less alkaline due to the addition of CaCl_2 , and the pH drop from above 13-10.5. Because the generation of CAH removes chlorides from the solution by binding as Friedel's salt, the problem of introducing Cl^- -ions is balanced by utilizing SCM.

Friedel's Salt ($\text{Ca}_3\text{Al}_2\text{O}_6 \cdot \text{CaCl}_2 \cdot 12 \text{H}_2\text{O}$) production is an additional process CaCl_2 preform. Friedel's salt inhibits chlorine attack and, as a result, reduces the incidence of aluminium surface corrosion. Friedel's salt is produced either by the reaction of CaCl_2 with calcium aluminate hydrate (CAH) and H_2O or by the substitution reaction of sulphate in AFm with the chloride. Equation 3.31 represents the creation of Friedel's salt by the reaction of CAH, CaCl_2 , and H_2O . Compared to AFm and CAH, Friedel's salt is more stable and binds more water, resulting in reduced porosity and increased strength^[22].



3.6.7 Silicate layer mechanism

A hypothesis that attempts to explain the corrosion-reducing properties of CaCl_2 for aluminium reinforcements in concrete structures is based on the assumption that the addition of CaCl_2 to the cement paste results in the formation of a protective silicate layer. The hypothesis's mechanism is based on the fact that CaCl_2 causes the dissolution of amorphous silicon from OPC and SCM, which then settles as a protective layer in the reinforcement-cement paste interface. This hypothesis is based on the findings of the two research groups, Jonathan P. Icenhower et al. and Tiany Zheng et al.^{[95][96]}. They respectively looked at the solubility of amorphous silica in alkali chloride solutions and the anti-corrosion effect of sodium silicate on 2024-T3 aluminium alloy in a NaOH medium.

Jonathan P. Icenhower et al. showed that the dissolution rate of amorphous silica increased at a rate of 21x by adding 0.05 molar NaCl compared to deionized water and predicted that the same effect would occur for other alkalies and iodine alkali chlorides. The significant increase in dissolution rate is due to an increase in the surface reactivity of amorphous silica. Silica polymorphs will have a net negative surface charge in aqueous solutions with a pH above 3-4. Dissolved cations will consequently be attracted to the surface, which follows that solvated cations reside within the interface area. Furthermore, the introduction of the cations imparts its solvating properties to the interface area, which results in an increase in Si-O hydrolysis reactions and consequently increases the dissolution of the silicate^[95].

The research group of Tiany Zheng et al. showed that the inhibition efficiency of a 0.01 mol/L Na_2SiO_3 was 97.23% due to silicate molecules which induced the formation of a stable and compact coating, preventing the penetration of water

molecules (H_2O) and subsequent corrosion reaction of aluminium. The formation of the coating is due to the negative adsorption energy of SiO_3^- on the aluminium surface, which indicates that the adsorption is spontaneous. Accordingly, SiO_3^- can replace water molecules and adsorb on the surface to Al in the (111) position. Due to the compact coating, the anodic half-reaction (Reaction 3.22) is cancelled in the corrosion process, and aluminium will not dissolve. Furthermore, the low energy gap δE of SiO_3^- leads to the high stability of the molecule, which thus also propagates to the high stability of the silicate coating. Low δE corresponds to little difference between E_{HOMO} and E_{LUMO} , which means that the interaction with the reacting species becomes strong and thus improves the inhibitor's effectiveness. In addition to the silicate coating, white aggregates of silicates in the form of crystals were observed on the aluminium surface^[96].

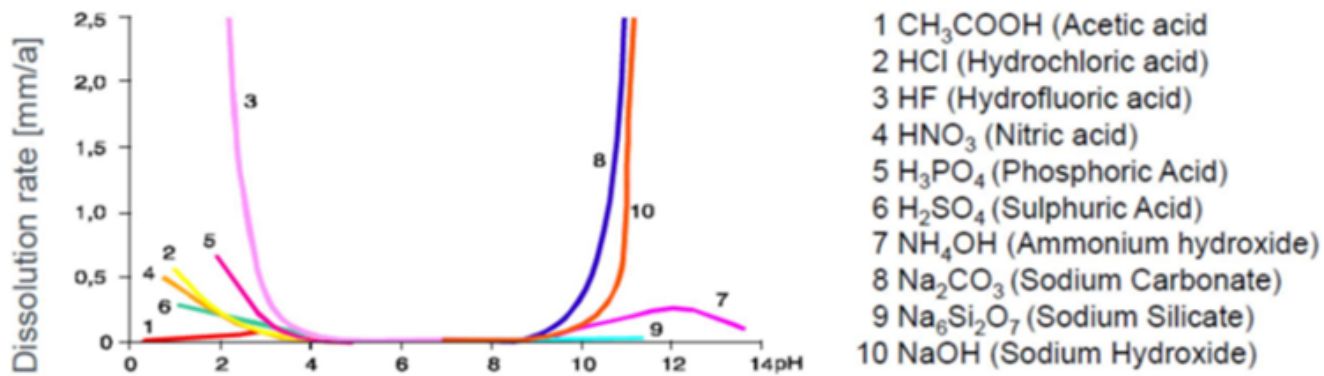


Figure 3.14: Aluminium dissolution rate in various liquids as a function of pH^[76].

Figure 3.14 shows the dissolution rate of aluminium in different solutions based on pH. The figure depicts a high aluminium dissolving rate in alkaline conditions where sodium hydroxide is present (10). In contrast, the dissolution rate is modest in an environment containing sodium silicate (9) at the same pH^[76].

3.7 Mechanical properties

For new environmentally friendly concrete structure with an aluminium reinforcing to be utilised in the real world, the mechanical qualities of the structure will be crucial. The concrete construction bonding strength will be one of its most critical mechanical qualities. This subsection tackles the mechanical principles essential to the master's thesis by addressing the bonding strength of concrete structures.

3.7.1 Bond strength of concrete constructions

The most important mechanical criteria for reinforced concrete as a composite building material is that concrete and reinforcement have an adequate bond strength^[97]. Consequently, it is crucial to comprehend this mechanism. Combining the advantages of concrete, which has strong compression and relative

durability, with the reinforcement, which is strong and ductile in the stretch, is the most significant advantage of employing reinforced concrete as a building material. In order to maintain this combined effect, it will be vital to have a good load transmission between the concrete and the reinforcement. This load transfer is defined as the bond strength and is idealised as a continuously propagating stress field at the interface of the concrete and reinforcement^[98]. At the interface of concrete and reinforcement, friction and adhesion contribute to the bond strength. It is influenced by axial stress and pressure across the reinforcement, tension and compression in the reinforcement, concrete strength, reinforcement surface condition, and transverse reinforcement^[99].

The pull-out test is a method for evaluating the bonding strength of concrete constructions. The principle of the test is to apply a tensile force to the end of a reinforcing bar that is not embedded in a cube of concrete. The test measures the ratio of the concrete structure's tensile strength to the amount of slip before it collapses.

The bond strength in concrete structures is often expressed in a bond-slip diagram, where the bond stress is given as a displacement function^{[100][101]}. The bond stress (τ_{dm}) is calculated using Equation 3.32, where F_a is the tensile strength, f_{cm} is the target value of the strength, and f_c is the average concrete strength. The pull-out test on a single specimen provides the relationship given in Equation 3.33, where Δ_o is the measured slippage under the tension force F_a .

$$\tau_{dm} = \frac{1}{5\pi} \frac{F_a}{d^2} \frac{f_{cm}}{f_c} \quad (3.32)$$

$$\tau_{dm} = f(\Delta_o) \quad (3.33)$$

The experimental binding strength-slip curve can usually be divided into five stages, represented in Figure 3.15:

1. **Non-slip phase:** The initial phase consists of a non-slip phase due to chemical adhesion and friction between the concrete and the reinforcement. This results in a straight line in the diagram.
2. **Slight slip phase:** In this stage, the increased load leads to failure of chemical adhesion between reinforcement and concrete, which results in relative gliding.
3. **Splitting phase:** In this phase, the increased continuous load leads to radial splits around the reinforcement due to the radial pressure from the reinforcement and the splitting bond stress (τ_{cr}) is reached.
4. **Decreasing phase:** In this phase, the increased continuous load leads to the complete collapse of concrete around the reinforcement, which leads to a rapid reduction of the bonding stress and a subsequent rapid increase in dislocation change.

5. **Residual phase:** In this stage, the reinforcement is completely torn from the concrete. Consequently, the bonding strength will only consist of the friction between the reinforcement and the concrete^[28].

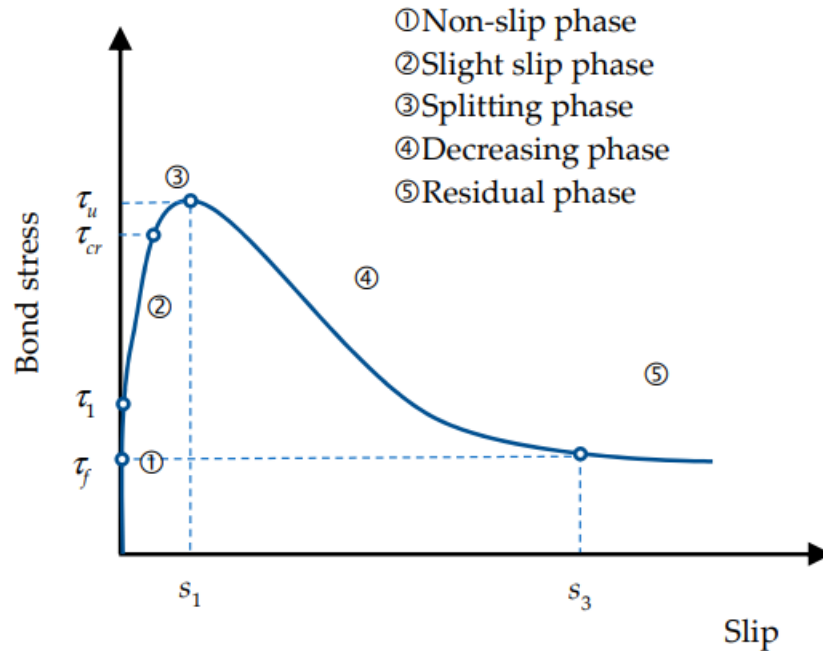


Figure 3.15: Illustration of typical bond stress-slip curve

In addition, bond stress depends on the geometry, bar type and concrete grade. Table 3.2 shows bond stress for cement grade for different bar types. Of interest in the masters thesis is the values for smooth bars in tension and concrete grade >40 .

Table 3.2: Design code (British standard BS 5400 for concrete bridge design) for bond stress for different bar type^[99].

Bar type	Anchorage bond stress (N/mm ²) for concrete grade			
	20	25	30	>40
Smooth, in tension	1.2	1.4	1.5	1.9
Smooth, in compression	1.5	1.7	1.9	2.3
Deformed, type 1, in tension	1.7	1.9	2.2	2.6
Deformed, type 1, in compression	2.1	2.4	2.7	3.2
Deformed, type 2, in tension	2.2	2.5	2.8	3.3
Deformed, type 2, in compression	2.7	3.1	3.5	4.1

3.8 Principle of SEM and EDS

This section describes the SEM and EDS instruments used in the experimental part of the master's thesis. The instruments are presented in a separate section

because it is essential to comprehend their operation during and after use to interpret the results.

3.8.1 Scanning Electron Microscope (SEM)

A **Scanning Electron Microscope (SEM)** is a microscope that uses a focused electron beam to scan the sample's surface to form a high-resolution image. Although the light microscope (LM) is the most common, the microscope is limited by a resolution limit. The resolution is defined as the ability of the microscope to distinguish two points at a defined distance and is set at 0.1 mm ($1 \cdot 10^6$ nm) for the LM^[102]. The resolution limit is due to the wavelength λ of visible light, which is between 400 nm (blue) to 700nm (red).

Compared with visible light, radiation from the electromagnetic spectrum has smaller wavelengths λ from, among other things, X-rays (10pm-10 nm) and ultraviolet (100-400 nm). Using radiation from electrons will thus be possible to reach a higher resolution than using visible light. By further utilising accelerating voltages of 200-300 keV, it is possible to reach an image resolution down to less than 0.1 nm (100 pm), which is a drastic change in resolution compared to optical microscopy^[103].

In SEM, a point on the desired surface is examined by focusing a thin electron beam on the point of the area. When the electron beam hits the sample surface, it results in the detection of detectable signals. The most commonly used signals in SEM are secondary and backscattered electrons and X-rays. The signal intensity is further used to modulate a corresponding image pixel. By scanning the surface of the desired sample with the electron beam, SEM will thus be able to reproduce an image at high resolution. The backscatter signal further provides information on relative differences in atomic numbers between different phases in the sample, with heavier elements resulting in a lighter-coloured SEM image. Furthermore, the emission of secondary electrons will vary as a function of the topography of the sample surface, which gives a good depth of field in SEM and has a three-dimensional effect.^{[104][105]}

3.8.2 Energy-Dispersive X-ray Spectroscopy (EDS)

Energy-Dispersive X-ray Spectroscopy (EDS) is used to identify and quantify the composition of elements on the surface of a sample. EDS is the most widely used chemical analysis tool due to the short analysis time and is often used as an appendix to SEM. Like SEM, EDS uses an electric beam to excite the atoms on the surface. Excitation involves the emission of X-rays with specific wavelengths that are individual to the atomic structure of specific elements. The X-ray emissions are detected by an energy scattering detector that can distinguish between different X-ray energies and analyse them. The results from the analysis are presented in an EDS spectre with identified elements and a table that reproduces weight percent (wt%) and atomic percent (at %) of the elements detected^{[106][107]}.

4 Experimental

This section highlights the experimental part of the master's thesis. This is achieved by introducing the experimental materials before describe the following three experimental parts:

1. Investigation of chemical corrosion qualities for the concrete construction
2. Analysis of the concrete structure
3. Investigation of the mechanical bonding properties for the concrete structure

The chemical corrosion qualities of the concrete structure are implemented by detecting H_2 , a bi-product of the corrosion reaction (Equation 3.24). Gas chromatography (GC) is used to detect H_2 . In addition, this experimental section is subdivided into two subcategories, the first of which focuses on the H_2 development of concrete structures containing industrial cement (ICEM) or hyaloclastite. Experiments are conducted to explore the potential of hyaloclastite and ICEM, as hyaloclastite is an exceptionally environmentally friendly SCM, and ICEM is significant from a practical and economic standpoint.

Additionally, the H_2 -emissions of a 6082 alloy in NaOH and NaSi solutions both with a pH=11.5 are examined. This experiment aims to obtain quantitative data for the hypothesised anti-corrosion silicate layer. The second section focuses on developing a new detection Flow system setup to detect H_2 -emissions more precise.

Concrete structure analysis is further subdivided into reinforcing surface analysis and cross-sectional interface analysis. These are accomplished utilising stereo microscope or light microscopy (LM), SEM, and EDS.

Using pull-out tests, the mechanical bond strength qualities of the concrete constructions are assessed experimentally. These tests map the mechanical potential of the concrete construction, since bond strength quantifies the ability of a reinforced concrete structure to combine the mechanical properties of the reinforcement and the concrete.

The section is divided into two parts. The first compares the bond strength conducted on concrete structures with 6082 reinforcement bars to those undertaken on concrete structures utilising stainless steel bars. In part two, two distinct geometries of the 6082 reinforcement are used, one of which employs smooth bars and the other L-shaped profiles.

The experimental components are depicted in a flow chart in Figure 4.1.

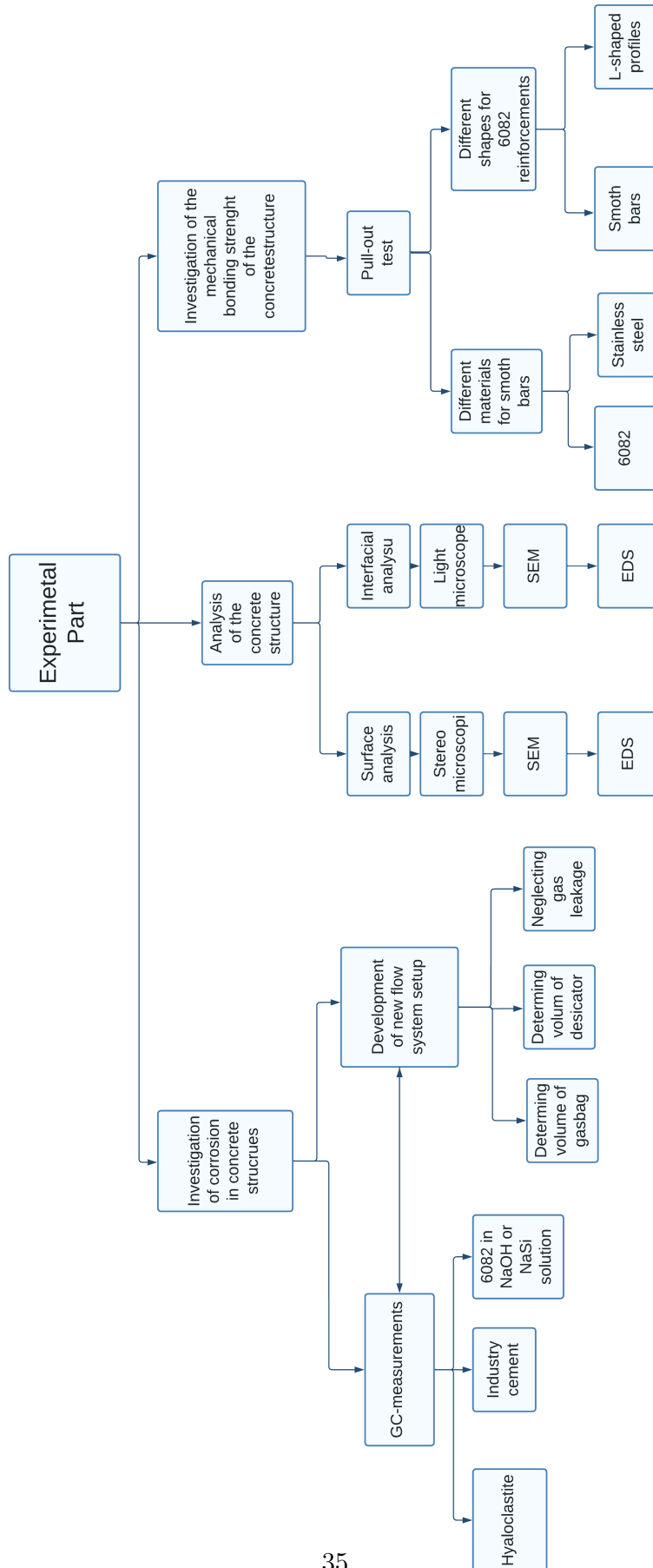


Figure 4.1: Flow chart of experimental part

4.1 Materials used in the experiment

4.1.1 6082 and 4xxxA alloys

The **6082** aluminium alloy belongs to the Al-Mg-Si alloy class known as AA6xxx. The chemical composition of the main elements for 6082 alloy is listed in Table 4.1. The alloy show further trace of Cr, Ti, Ga, V, Zn, Ni, B, Zr, Pb, Sn, Na, Ca, Bi, Be, Co, Sb, P, Ag and Sr^[108]. Fagermo ram extruded the alloy into profiles in the spring of 2020. Before being extruded, the ingots were homogenised for 2 hours and 15 minutes at 575 °C. In addition, the extrusion blocks were preheated to enhance their extrudability by overheating the ingots to 560 °C and then cooling them to 500 °C. After extrusion, water was used to quench the profiles. Prior to the experiment, 6082 was heat-treated to increase the thickness of its oxide layer. Table 4.2 describes the thermal treatment. 6082 was subjected to 530 °C for 10 minutes prior to being quenched with water. Then, the alloy was aged for 9 hours at 175 °C before being quenched with water once more. Due to the processing of the alloy, 6082 has a heterogeneous structure with recrystallized tiny grains on the surface and fibrous grains in the core. Consequently, 6082 offers high corrosion resistance, formability, and machinability, moderate strength, and adequate weldability^[109].

4xxxA is a member of the 4xxx alloy class and has the formula AlSi_9Cu_2 . Although 4xxxA is typically a cast alloy, the 4xxxA alloy utilised in these tests is distinct since it is extruded. Prior to extrusion, the 4xxxA ingot was homogenised for three hours at 500°C. In addition, the ingot was preheated to 143 °C to enhance the alloy’s extrudability. Like the 6082 alloys, 4xxxA was water-quenched following extrusion. In addition, the oxide layer of 4xxxA was improved by heat treatment. The heat treatment is detailed in Table 4.2 and begins with subjecting the 4xxxA alloy to 525 °C for 5 hours before quenching it in water. The alloy is then aged for 12 hours at 180 °C before being quenched in water once more. Since the high Si and Cu concentration in 4xxxA boosts the alloy’s wear resistance and strength, it is commonly utilised in engine block construction. Moreover, will engine blocks frequently employ secondary alloys with a high level of impurities. Therefore, in this experiment, 4xxxA is used to map the possibility of reusing existing engine blocks as reinforcement in concrete. Table 4.1 depicts the main element composition of the 4xxxA alloy utilised in the experiment. Furthermore Ti, Ni, Sn, Ca, Bi, V, Co, Sb, P, Sr, Zn, Cr, Pb, B, Zr, Cd and Ga where found as trace element in the alloy.

Table 4.2: Heat treatment procedure for 6082 and 4xxxA alloy.

Alloy	Solid solution	Quenching	Aging	Quenching
6082	530[°C] for 10 [min]	Water	175[°C] for 9[hour]	Water
4xxxA	525 [°C] for 5 [min]	Water	180[°C] for 12 [hour]	Water

Table 4.1: List of the main alloying elements of the 6082 and 4xxxAl alloy.

Alloying element	6082 [wt %]	4xxxAl [wt %]
Al	97.68	87.48
Si	0.96	9.18
Cu	0.01	2.15
Mg	0.63	0.28
Mn	0.49	0.11
Fe	0.18	0.41

4.1.2 Ordinary Portland Cement (OPC)

Ordinary Portland Cement (OPC) is the most commonly used and widely distributed cement globally and is the primary component of construction cement concrete structures. The cement is primarily composed of calcined limestone and clay minerals, which are then ground into a fine powder. The chemical composition of the OPC used in the experiments are listed in Table 4.3^[110].

Industry cement (ICEM)

Industry cement (ICEM) is a speciality OPC used for concrete elements and concrete products. Furthermore, the ICEM's rapid strength development makes it suitable for Norwegian construction practice during the winter. ICEM further differs from Construction Cement (CCEM) in that it contains twice as many alkalis. Table 4.3 gives the oxide composition of the ICEM used in the experiments^[24].

4.1.3 Calcined clay (CC)

Due to its advantageous pozzolanic characteristics, Calcined Clay (CC) is a desirable choice for SCM. The experiment uses CC imported from Estonia. Table 4.3 shows the oxide composition of the used clay.

4.1.4 Hyaloclastite

Hyaloclastite is a volcanoclastic deposit formed by the fragmentation of lava flow surfaces during subglacial or underwater extrusion^[20]. Hyaloclastite is an attractive SCM candidate due to its pozzolanic characteristics. Table 4.3 shows the oxide composition of the hyaloclastite used in the experiment.

Table 4.3: Oxide composition of OPC, ICEM CC and Hyaloclastite found by XRF, as well as corresponding loss on ignition (LOI), chloride concentration and the material density. The composition was found by HC Global RD and Norcem^[111].

Oxide	OPC [wt%]	ICEM [wt%]	CC [wt%]	Hyaloclastite [wt%]
SiO ₂	21.12	19.6	62.57	47.80
Al ₂ O ₃	4.60	4.70	18.50	14.37
Fe ₂ O ₃	3.77	3.20	3.94	11.89
CaO	63.21	63.10	0.21	11.84
K ₂ O	0.40	1.10	3.77	0.31
Na ₂ O	0.35	0.40	0.08	1.82
MgO	1.71	2.30	0.48	9.16
TiO ₂	0.31	0.30	0.39	1.54
P ₂ O ₅	0.18	0.10	0.10	0.16
Mn ₂ O ₃	0.06	-	-	-
MnO	-	0.1	0.01	0.16
SO ₃	3.39	3.7	0.01	0.04
Na ₂ O Eq.	0.61	-	-	-
LOI	1.26	1.3	2.03	0.41
Chloride	0.025	0.04	0.00	0.02
Density(kg/dm ³)	3.15	3.14	2.61	2.87

4.2 Investigation of chemical corrosion qualities for the concrete construction

An investment in corrosion resistance of concrete construction was performed, using Gas Chromatography (GC) to detect H₂. This was accomplished by measuring the H₂-development of concrete structures with various compositions and reinforcing materials. In addition, the H₂-development of 6082 reinforcements in a solution of NaOH and a solution of NaSi with pH = 11.5 was determined. A Stationary system and a Flow system were used for the experimental procedure. Table 4.4 outlines the testing conducted on each system. In this part of the experimental section, the standard procedure for creating the concrete structure will be presented before the two systems are described. The experimental section will also outline how the volume of the new Flow system was determined.

Table 4.4: Specification of the composition of each GC sample performed on a Stationary and Flow system setup, respectively. The OPC used in the experiments was a CCEM.

Stationary setup	Flow system setup
Concrete construction samples	Concrete construction samples
Hyaloclastite, OPC, CaCl ₂ , 6082 CC, OPC, CaCl ₂ , 6082	Hyaloclastite, OPC, CaCl ₂ , 6082
	CC, OPC, CaCl ₂ , 6082
	CC, ICEM, CaCl ₂ , 6082
	CC, ICEM, 6082
	CC, ICEM, CaCl ₂ , 4xxxA
	CC, ICEM, 4xxxA
	Reinforcement and solution samples
	6082, NaOH
	6082, NaSi

Table 4.5: Specific surface area [m²/kg] of the SCMs used in the thesis.

SCM	Specific surface area [m ² /kg]
CC	1111
Hyaloclastite	733

4.2.1 Procedure

This section presents the procedure for the formation of the cement paste. Each test consisted of preparing a 200 mL cement paste. Table 4.6 provides the weight ratios of the components that make up the cement paste. Before carrying out this experiment, extruded cylindrical aluminium pieces of 40 mm in length and Ø 10 mm were cut using Labotom-15 cutting machine (Figure 4.9c). Table B.1 details the length of each specimen throughout the experimental phase, whereas Figure 4.2 illustrates the length, diameter, and shape of the reinforcements used. In addition, a mix master and laboratory scale were utilised to mix and weigh components, respectively. The procedure is reproduced step by step as described below;

1. Start the GC recording while disconnected from the desiccator to stabilise the recording at atmospheric concentration.
2. Weigh 9.44 g CaCl₂ salt.
3. Weigh 118 g of H₂O and pour the H₂O into the mixing bowl.

-
4. Pour CaCl_2 into the mixing bowl with the added H_2O and mix the solution until the salt is dissolved with a spoon.
 5. Weigh out 118 g of the SCM and 106 g of the cement. Gently mix the powders with a spoon until a "well mixes" powder has formed. Keep the dust formation to a minimum.
 6. Carefully and step wise, pour the cement/clay mixture into the aqueous solution, stirring constantly.
 7. Assemble the mixer by tying the mixing bowl and the mixer together. Then mix cement mixture for 1 minute at full speed.
 8. Disassemble the mixer and pour the cement paste into a plastic cup.
 9. Tamp the cup 10 times.
 10. Place the aluminium sample centrally in the plastic cup with the cement paste to cover the sample entirely.
 11. Insert the plastic cup into the desiccator. Close the desiccator, and connect the GC to the connector up the top of the desiccator. Register the starting point.
 12. Wait at least 20 hours before removing the plastic cup with the cement paste and the aluminium piece from the desiccator. Then turn off the GC.

For samples consisting of a 6082 alloy and an alkaline NaOH or NaSi solution, the alloy piece with the same diameter described above and in Figure 4.2 was inserted in a plastic cup. Furthermore, the alkaline solution was poured into the cup such that the solution was in excess. The cup containing the solution and the alloy piece was then put in the desiccator and connected to the GC to record H_2 -emissions for at least 20 hours.

Table 4.6: The table provides the percentages by weight of the cement paste's components.

Component	Amount(Part per weight)
CEM	0.292
SCM	0.358
H_2O	0.324
CaCl_2	0.026

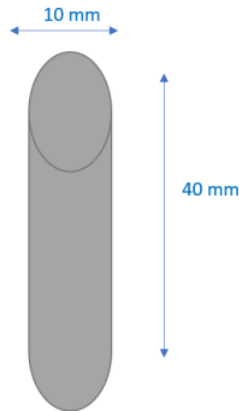


Figure 4.2: Illustration showing the dimensions of the experimental reinforcements.

4.3 Experimental setup

The GC used in the experiments was an Agilent 990 Micro GC which used a double-column to register the gas emission. Column A (MS5A SS 10MX0.25MMX) analysed and registered lighter elements, while column BB (PORAPLOT Q UM 10MXO) classified heavier elements. Further parameters are prepared in Table 4.7.

Table 4.7: GC parameters for Columns A and B. Each measurement used a sample flow of 10-20 mL/s and an injection interval of either 180 or 600 s.

Parameters	Column A	Column B
Injection Heating [°C]	90	90
Column Heating [°C]	110	70
Injection Time [ms]	50	50
Backflush Time [s]	40	-
Column Pressure [Psi]	22.0	22.0

4.3.1 Stationary setup

Regardless of which experimental parallel was conducted, the experimental Stationary setup remained the same. Figure 4.3 depicts the experimental Stationary setup, with the various pieces A, B, C, and D representing ;

- A Represents the aluminium sample embedded in a cement/clay-past inserted in a plastic cup. The cup is inserted into a desiccator.
- B Represents a desiccator connected to a GC through an airtight glass tube.
- C Represents the Agilent 990 Micro GC.
- D Represents the pressure gauge, indicating that when the inner water column rises, the system's pressure rises.

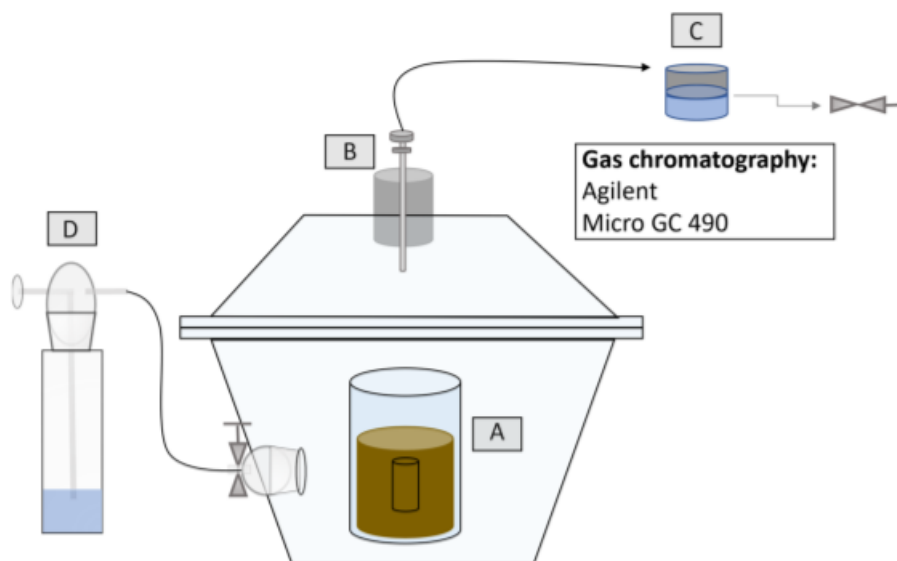


Figure 4.3: Illustration of the Stationary GC setup, with A, B, C, and D representing the various components of the system.

Small gas samples were sucked out of the outlet to be analysed by the GC using a sampling flow of around 10-20 mL/min, an injection interval of 600 seconds, and a sampling period of 5 seconds. To eliminate residual H_2 -gas from earlier measurements, the GC was started without the desiccator before each measurement to reset to ambient concentration. The starting point for each test was the environmental concentration. Figure 4.5a offers an image of the actual Stationary GC-setup.

4.3.2 Flow system setup

Figure 4.4 depicts an illustration of the experimental Flow system setup. The GC setup was identical and independent of the experimental parallel performed. The different setup parts of the GC system A, B, C, D, E and F represent;

- A Illustrate the plastic cup with the embedded aluminium sample in the cement/clay paste.
- B Illustrates the desiccator and the connected distillation column, where the cup is placed inside.
- C Illustrates the external pump, which causes an airflow before each concentration measurement.
- D Illustrates the GC Agilent 990 Micro GC.
- E Illustrate the check valve that prevents and closes air emissions when inflating the gas bag.

F Illustrates a gas bag that holds an extra volume and prevents the formation of negative pressure and leakage during the experiment.

Prior to each experiment, the external pump cleaned the system by pumping out earlier gas concentrations, before the gasbag was pumped up to obtain a volume of 1,7 L to counteract negative pressure.

During the experiment, GC analysed the current system's concentration by sucking small gas samples out of the outlet using an injection interval of 180 seconds and a sampling time of 5 seconds. For this, a sampling current of approx. 10-20 ml/min was used. Before each concentration analysis, the external pump was turned on with a current of 854 mL/L for 30 seconds to smooth out any accumulations of H₂ molecules in the upper part of the system and thus cause the GC to register a more realistic value of the actual H₂-emission.

To remove unwanted residual H₂ gas from previous experiments and clean the system, the system was reset to atmospheric concentration by starting the GC and external pump before each experiment.

In each measurement, the atmospheric concentration was used as the zero point at the beginning of the experiment. To further prevent negative pressure during the experiment caused by exhaust from the GC, the gas bag was inflated with the external pump for 120 seconds with atmospheric air. Table 4.7 shows additional parameters used in the layout.

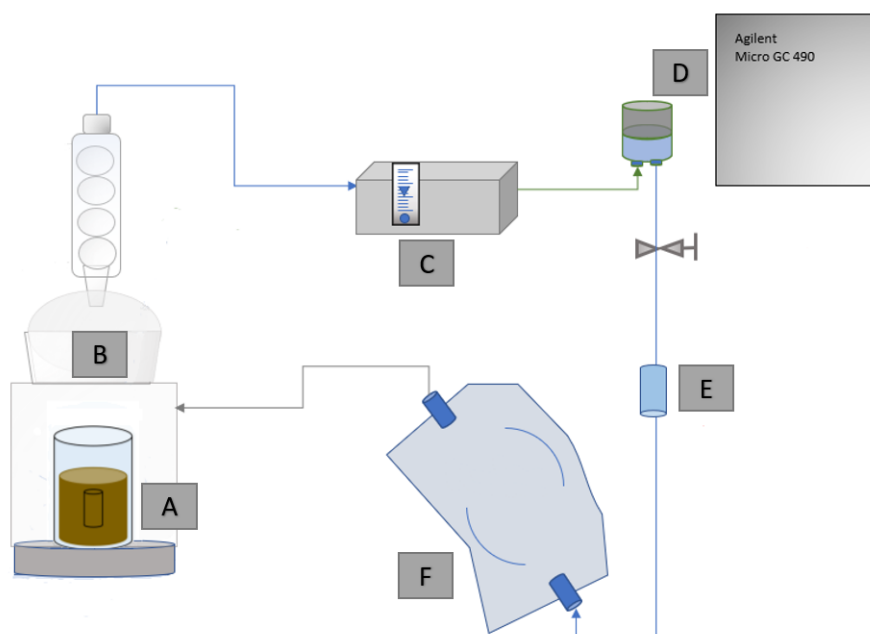


Figure 4.4: Illustration of the Flow system setup, where the different parts of the setup are respectively represented by the letters A-F.

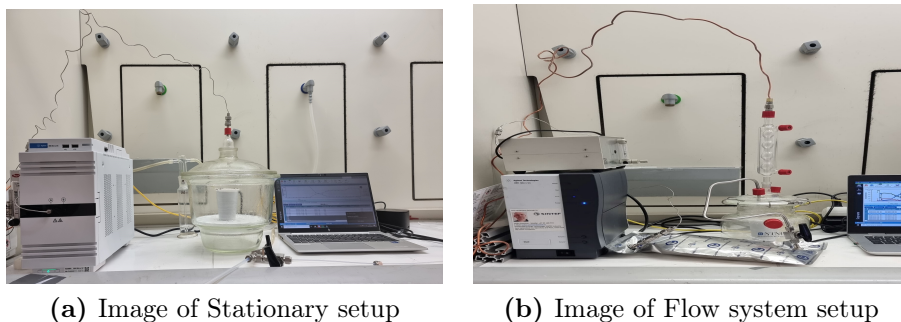


Figure 4.5: Images of the Stationary and Flow system setup.

4.4 Measurements conducted prior to GC measurements of the Flow system

Before the first GC measurement in the new Flow system, the volume of the new system was found, and measurements were carried out to ensure against leaks. The volume of the Flow system was determined by finding the volume of the atmospheric gas in the gas bag and the volume of the desiccator. The remaining volume from transitions between the various Flow system components was neglected because the diameter of the pipes constituted to a neglecting volume. The volume of the desiccator was found by the Archimedean method, while the volume of the atmospheric air in the gas bag was found by determining the air-flow to the external pump. The sections below present methods used to find the volume of the new system and the procedure for insuring against leaks in the system.

4.4.1 Determining the desiccator and distillation tube's volume

The volume of the desiccator and the distillation column were found by measuring the difference in weight before and after the components were filled with water. The method is based on the Archimedes method and the very definition of density (ρ). The Archimedean method states that the weight of the liquid displaces equal to the force lifted^[112]. Furthermore, density (ρ) is defined as mass per volume (Equation 4.1). Since water became the starting point for determining the metric mass unit SI, one cubic centimetre (1 cm³) of water weighs one gram (1 g), which results in one litre of water(1 L) weighing one kilogram(1 kg)^[66]. Consequently, the weight change (kg) before and after filling the desiccator and distillation tube with water will correspond to the volume (L) of the system.

$$\rho = \frac{m}{V} \quad (4.1)$$

4.4.2 Determining the volume of air in the gas bag

The volume of atmospheric air in the gas bag was found by determining the airflow to the external pump. Figure 4.6 shows the layout for determining the airflow. Before the experiment, the tube into the gas bag was placed in a measuring cylinder that was turned upside down and partially filled with water. The tube and measuring cylinder were placed in beakers filled with water. The experiment was based on reading the height of the water level (and consequently the volume change) before and after the pump had run for a specific time and filled the measuring cylinder with air. The airflow was further found by dividing the change in volume (water surface height) by the pumping time. The experiment started by turning on the external pump for 10 seconds and registering the height difference to the water surface. The procedure was repeated 3 times before the same procedure was repeated 3 times with a pumping time of 13 seconds.

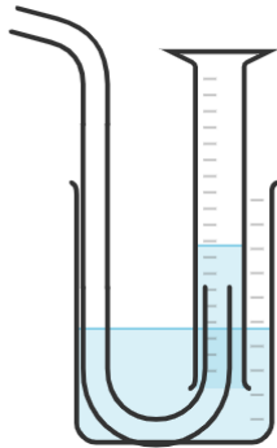


Figure 4.6: Illustration of setup for determination of the air flow from the external pump.

4.5 Analysis of the concrete construction

This subsection presents the procedure for analysis of the concrete structure. The analysis is divided into the two subsections:

1. Surface analysis of reinforcement
2. Cross-sectional interface analysis between the reinforcement and the concrete.

For the surface analysis, stereo microscope, SEM and EDS were used to analyse the samples. The cross-sectional interface analysis took advantage of LM, SEM and EDS.

The analyzed samples are listed in Table 4.8. The analysis was conducted on 8 samples with varied compositions. The adjusted parameters entail:

1. Use of 6082 or 4xxxA as reinforcement

2. Use of freshwater or seawater as a curing agent
3. Use of added CaCl_2 to the cement paste

The samples were collected from the author's prior project work.

Table 4.8: Samples and their components utilised in the analysis of concrete construction.

Sample	Composition
1	6082, Seawater, CaCl_2
2	6082, Seawater
3	6082, Freshwater, CaCl_2
4	6082, Freshwater
5	4xxxA, Seawater, CaCl_{20}
6	4xxxA, Seawater
7	4xxxA, Freshwater, CaCl_2
8	4xxxA, Freshwater

4.5.1 Sample preparation for surface and interface analysis

Before analysis, the samples were prepared for the method of analysis. Figure 4.7 depicts a surface and cross-sectional interface analysis road flow chart. The preparation process begins with removing the reinforcement from the concrete mass that has solidified in a plastic cup. This was done by chopping out the reinforcement using a hammer and chisel.

The reinforcement was then examined using a stereo microscope for surface examination. Figure 4.9a depicts a picture of the utilised stereo microscope Lectropol-5. After examining the reinforcement using a stereo microscope, the surface was subjected to SEM and EDS analysis. Before SEM analysis, the samples were treated to improve their conductivity and, consequently, their picture quality. The conductivity of the samples was increased by covering the reinforcement with aluminium foil, leaving only a small region of uncovered reinforcement where the analysis was conducted. In addition, a carbon tape was adhered between the unmodified reinforcement area and the aluminium foil to establish electrical contact between the portion of the sample being tested and the aluminium foil. Figure 4.8a depicts the samples after aluminium and carbon tape were applied. To further enhance the conductivity of the sample, a thin carbon coating was sprayed onto the surface of the reinforcement. Figure 4.9e shows the Cressington 208 Carbon Coater used to coat the samples with the desired carbon coating.

For cross-sectional interface surface analysis, the carved reinforcement was cut to form a cross-section before being embedded in epoxy and analysed using a LM, SEM, and EDS. The reinforcement was cut with a Labotom-15 cutting machine to create a 1 cm long reinforcement sample with a cross-section. The Labotom-15 cutting machine is depicted in Figure 4.9c. After the reinforcement was cut, it was placed and cured in epoxy with a 15 mm diameter, forming a cylinder. After

the epoxy had cured, the samples were polished with the Tegramin-30 polisher to ensure good contact with the interface's cross-section. Figure 4.9d depicts the polishing machine Tegramin-30 polisher where the Sigurd 20 application was implemented. After the reinforcement was cut, placed in epoxy, and polished, the sample was analysed using a LM (Figure 4.9b). Furthermore, the cross-sectional interface analysis was performed by studying the samples in SEM and EDS. As for the surface analysis, the samples were embedded in an aluminium foil, and a carbon tape was adhered between the reinforcement and the aluminium to improve conductivity. Figure 4.8b depicts the ready-for-SEM and EDS analysis specimens. Additionally, a carbon coating was put on the cross-sectional contact surface to increase conductivity.

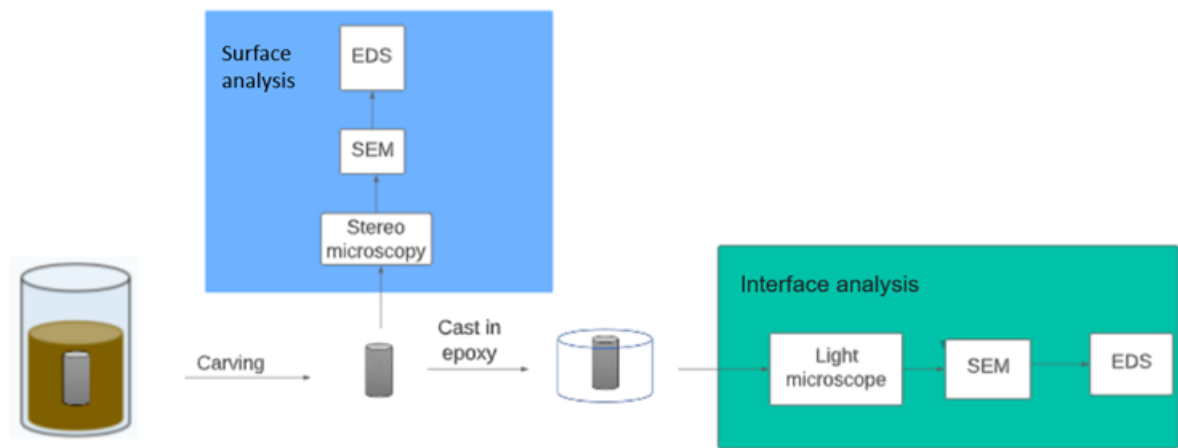


Figure 4.7: Flow chart of sample preparation and method used for the analysis of concrete construction



(a) Image of SEM and EDS prepared samples for surface analysis.

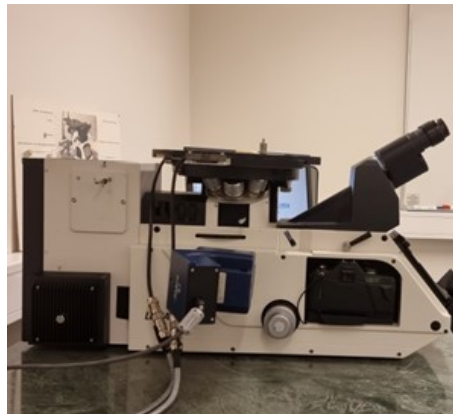


(b) Image of SEM and EDS prepared samples for interfacial analysis.

Figure 4.8: Images of SEM and EDS prepared samples for surface and interface analysis.



(a) Image of the stereomicroscope Lectropol-5



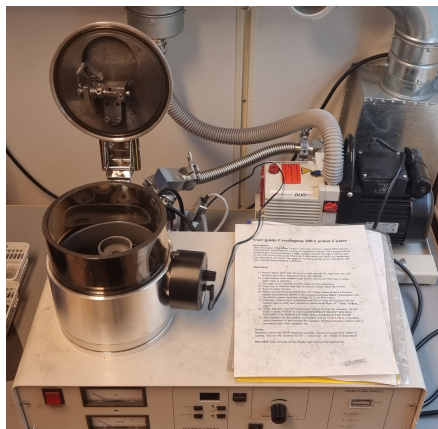
(b) Image of the LM Leica MeF4M.



(c) Image of the cutting machine Labotom-15



(d) Image of the polishing machine Tegramin-30 polisher.



(e) Image of the carbon coater Cressington 208



(f) Image of the SEM-EDS machine Zeiss-Ultra 55

Figure 4.9: Images of the instruments used for the analysis procedure.

4.6 Mechanical properties

This subsection deals with the experimental part that were carried out to determine the mechanical properties of the concrete structure. The mechanical properties of the concrete structure were based on carrying out pull-out tests, where bond strength of the the concrete structure was found by pulling the reinforcement out of the concrete mass.

Since the concrete structure and the 6082 alloys with which the pull-out tests were carried out has a larger order of magnitude and heat treatment than the experiments for GC, the sub-chapter will first present the preparation of the 6082 alloys and formation of the concrete structures for the pull-out tests. Then the pull-out test will be presented.

4.6.1 Preparation and heat treatment of the 6082 reinforcements

The pull-out tests were based on pulling out **3** 6082 aluminium rods, **3** 6082 L-shaped 6082 profiles and **3** stainless steel rods, all 1 meter long and $\text{\O} 20$ mm.

The L-shape was created by cutting a 6082 alloy as illustrated in Figure 4.10 with a bandsaw. The dimensions of the L-shape are shown in Figure 4.11. Furthermore the rods where cut by usage of the cutting machine depicted in Figure 4.9c.

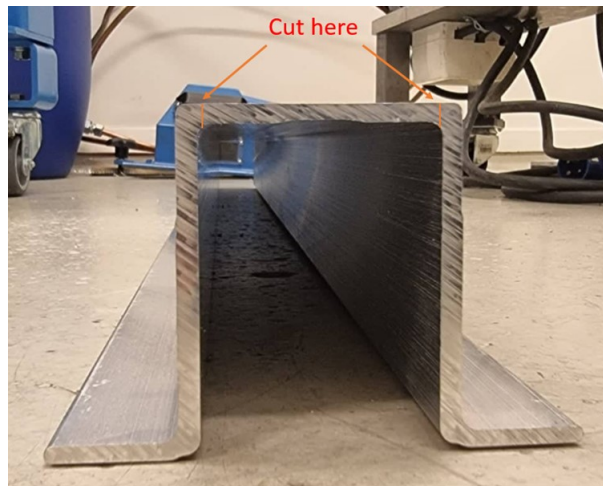
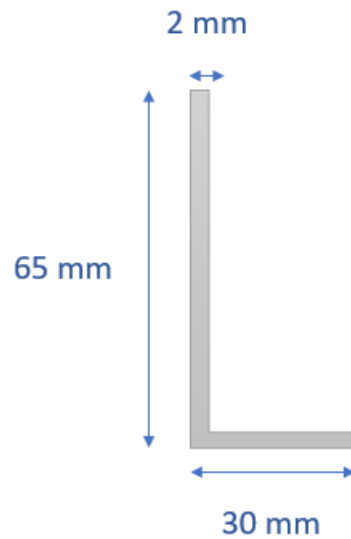


Figure 4.10: Specifies where the 6082 alloy was cut to get the appropriate L-shape

Before casting the aluminium reinforcements, these were heat-treated to increase their oxide layer. Table 4.9 lists the heat treatment. The heat treatment was carried out using SINTEF's oven. In the first step of the heat treatment, the 6082 alloys were heated from RT to 185 °C within 1 hour. This was followed by an aging process in which the alloy were exposed to an constant temperature of 185 °C maintained for 5 hours. The aging process was the ended by air-cooling the alloys.

Table 4.9: Heat treatment procedure for 6082 previously to the pull-out test.

Alloy	Heating	Aging	Quenching
6082	From RT to 185 C within 1 hour	185 for 5 hours	Air

**Figure 4.11:** Illustration showing the dimension of the experimental L-shape profile.

4.6.2 Pull-out test

Preparation of the pull-out samples started with the heat-treated aluminium profiles being cast in concrete by SINTEF. Table 4.10 displays the concrete mix composition given for 57 L which is based on the same concrete composition as described in Subsection 4.2.1. The casting was based on producing 200m × 200m × 200m blocks. Figure 4.13 displays the test specimen, consisting of a reinforcing bar with one end embedded in the centre of a concrete cube. In addition, 10 mm of the end of the reinforcing bar protrudes on the opposite side of the concrete cube.

3 6082 smooth rods, 3 6082 smooth L-shaped profiles and 3 stainless steel rods were cast in a 200mm x 200mm x 200mm concrete cube. Before the bond strength of the concrete systems was examined using the pull-out test, the samples were cured for 28 days following casting.

Figure 4.12a shows the concrete structure right after the smooth bars were cast in the cement paste, while Figures 4.12b and 4.12b show the smooth bars and L-shape profile concrete structures after 28 days of hardening, respectively.

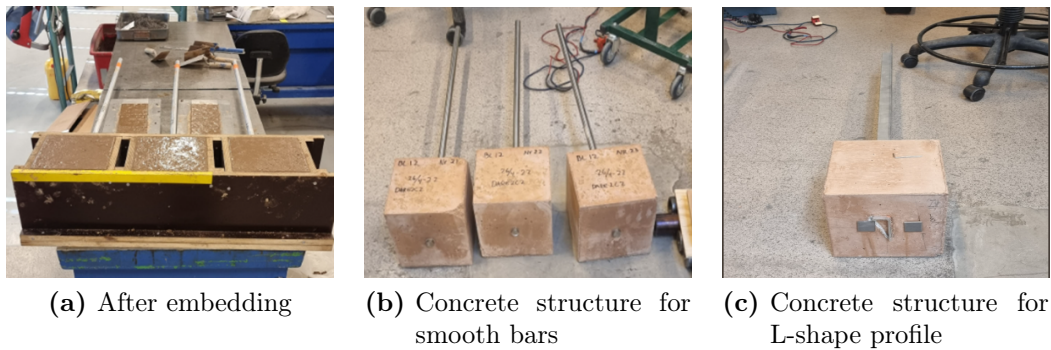


Figure 4.12: Concrete structure before pull-out test.

The bond strength testing was conducted by SINTEF, which based the pull-out test on NS-EN 10080. Figure 4.14 depicts a image of the pull-out test setup. A linear variable differential transformer (LVDT) was attached to the side with the short rod to detect the displacement of the reinforcement. This was done by gluing magnets to the side. Furthermore, the load rate was computed using Equations 3.32 and 3.33.

Table 4.10: Cement paste composition utilised during bond strength tests. The recipe corresponds to a volume of 54 L.

Material	Weight [kg]
Norcem Anlegg SR A-5319	10.2
Calcined clay, A-5269	12.5
Free water	9.7
Absorbed water	0.3
0-8 Årdal A-5709(Aggregate)	53.9
8-16 Årdal A-5709(Aggregate)	39.0
Sika Viscocrete 6225, A-5724((Superplasticizer))	0.66
CaCl ₂	0.91

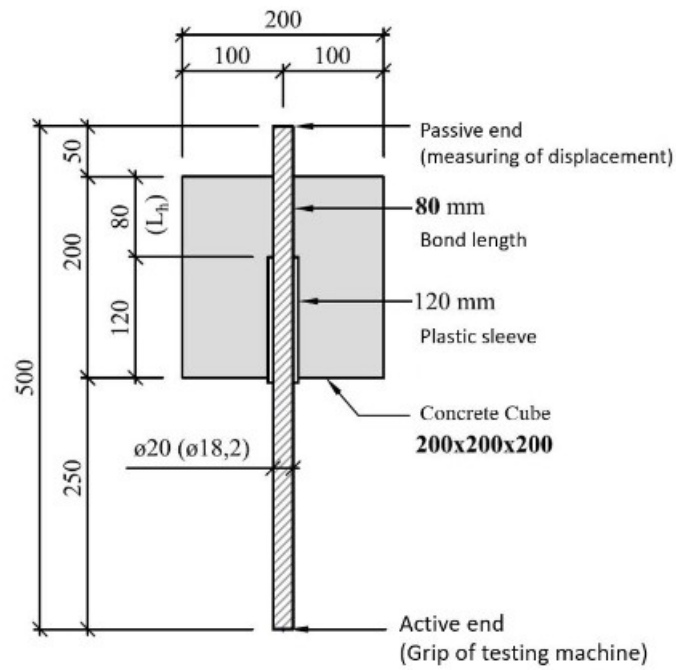


Figure 4.13: Design of a concrete system for $\varnothing 20$ mm rods used in pull-out test^[99].

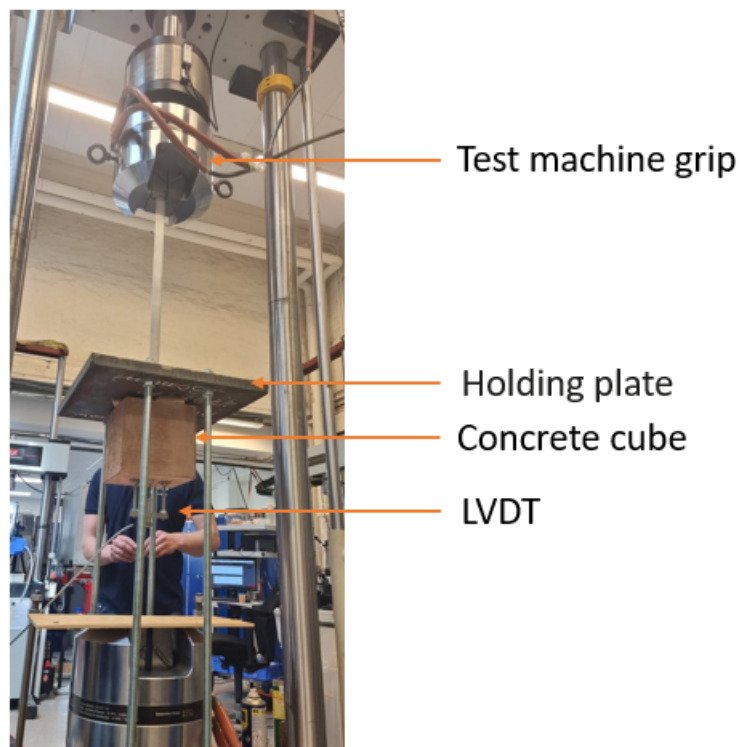


Figure 4.14: Image of pull-out test set-up.

5 Results

This section presents the experimental results from the master thesis. The results are divided into the sections investigation of chemical corrosion qualities for the concrete construction, Surface analysis results, interface analysis results and mechanical results.

Furthermore, Investigation of chemical corrosion qualities for the concrete construction are divided into result from Stationary and Flow system setup. The results from the Stationary setup include measurements from hyaloclastite and estonian CC. The results for the Flow system start by presenting finding from the setup development, before presenting the results from hyaloclastite, ICEM and measurements from NaOH and NaSi solution. The ICEM section is further divided into results from 6082 against 4xxxA reinforcement and a comparison of ICEM against CCEM.

The surface analysis will first present finding from stereo microscope before results from SEM and EDS are shown. The Interface analysis starts by exhibit LM and SEM results before results from the EDS interfacial analysis are presented. The mechanical results involves data from pull-out tests for smooth bars and L-shape profiles. The section is divided into pull-out test results for 6082 and stainless steel smooth bars as well as pull-out test result for 6082 smooth bars and L-shape profiles.

5.1 Investigation of chemical corrosion qualities for the concrete construction

5.1.1 Stationary setup

Stationary setup: Hyaloclastite and Estonian CC

Figure 5.1 displays the reported H_2 -emissions per area ($\frac{H_2\%}{mm^2}$) for 6082 reinforced concrete structures that used hyaloclastite or estonian CC as SCM. Table 5.2 and Figure 5.1 reveal that the hyaloclastite mixture emits initial H_2 after 50 minutes. A nearly exponential increase follows this H_2 -emission that lasts for 150 minutes. The emission curve for H_2 then begins to approach a limit value and stabilises. The experiment finishes with a final H_2 concentration of $4.41 \cdot 10^{-5} \frac{H_2\%}{mm^2}$ after 23 hours. Figure 5.1 and Table 5.2 indicate that the concrete structure, including estonian CC, emits no H_2 until 250 minutes (4 hours and 10 minutes). The concentration of H_2 then increases at a nearly exponential rate until 370 minutes have passed. When the curve has stabilised, and the H_2 concentration has been adjusted to a limit value, it logs a H_2 -emissions of $4.256 \cdot 10^{-5} \frac{H_2\%}{mm^2}$.

A further observation from Figure 5.1 is significant variations in subsequent measurements beyond the experiment, which are observed as a notched curve. Both samples present this phenomenon, especially during the conversion and stabilisation phase.

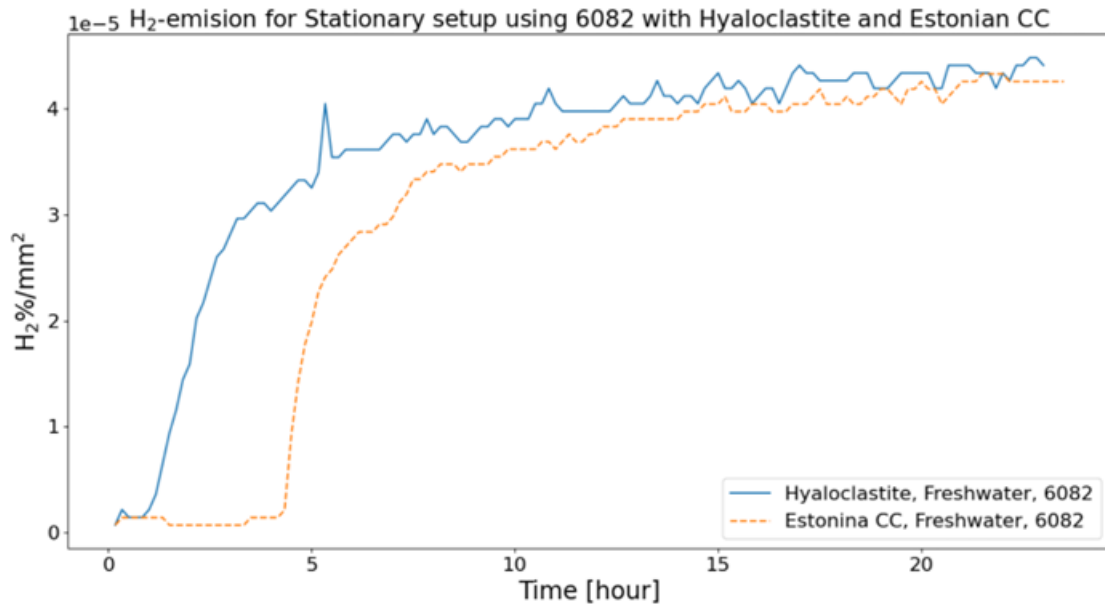


Figure 5.1: GC measurement of H₂-emission when using hyaloclastite and Estonian CC as SCM and 6082 reinforcements.

5.1.2 Flow system setup

Setup development

Table 5.1 show the found volume of the desiccator and distillation column and the airflow to the pump used to pump up the gas bag. The weight difference of the desiccator and the distillation column when filling with water(H₂O) was 2.59 kg which corresponds to 2.59 L, while the airflow to the pump was measured at 854mL/L. By pumping the gas bag up for 2 minutes (Section 5.1.2), the volume of the flow system will correspond to 4.298 L.

Table 5.1: Results for determining the new volume of the Flow system

Desiccator and column without H ₂ O	1.734 kg
Dessicator and column with H ₂ O	4.324 kg
Weight difference	2.59 kg
Airflow of external pump	854 mL/min
Gained volume after 2 min	1.708 L
Volume of flow-system	4.298 L

Hyaloclastite

Figure 5.2 shows the H₂-emissions for samples with hyaloclastite and CC, where both samples use 6082 reinforcement and CaCl₂-added cement paste. The figure shows that hyaloclastite has a lower final H₂-emission and a previously first registered H₂-emission than the sample with CC. Table 5.2 quantifies the H₂-emission development of the samples.

Figure 5.2 shows a first detected H_2 -emission after 39 minutes for the sample with added hyaloclastite. A subsequent rapid increase in H_2 -emissions lasts for 141 minutes before the H_2 curve begins to convert. The H_2 -emission is stabilised after 450 minutes and shows a final H_2 concentration of $7.70 \cdot 10^{-5} \frac{H_2\%}{mm^2}$. When using CC, the sample shows a first registered H_2 -emission after 135 min. A subsequent increase in H_2 lasts until 804 minutes have passed when the curve begins to convert. The sample shows a final H_2 concentration of $10.66 \cdot 10^{-5} \frac{H_2\%}{mm^2}$.

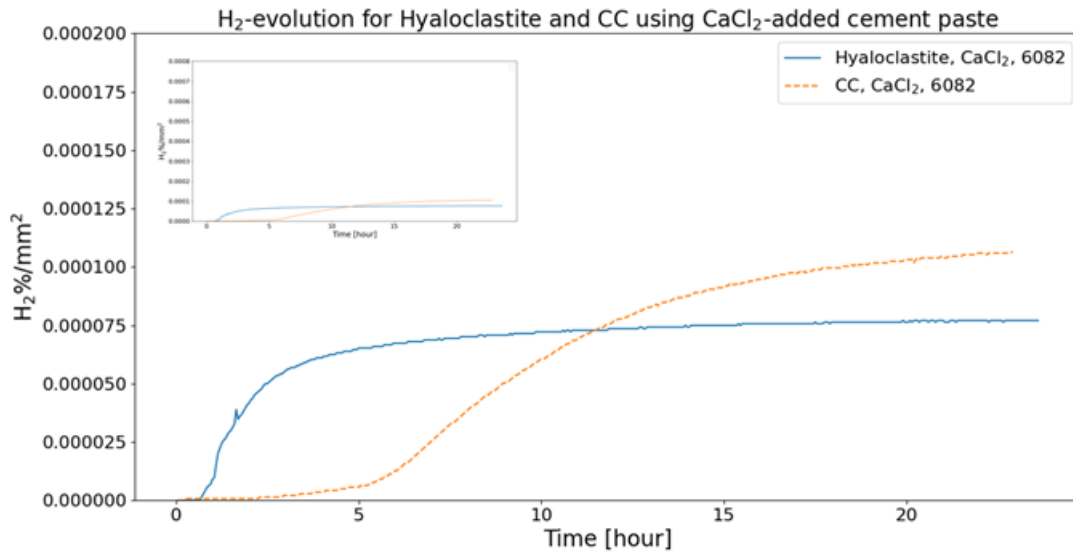


Figure 5.2: H_2 -emissions for samples with hyaloclastite and CC, with 6082 reinforcement and $CaCl_2$ -containing cement paste. The graph in the upper corner shows the same order of magnitude as Figure 5.3

ICEM

6082 against 4xxxA Figure 5.3 depicts the H_2 -emissions for samples produced with 6082 or 4xxxA alloys and ICEM. $CaCl_2$ has also been added to one of the 6082 and 4xxxA alloys.

Figure 5.3 and Table 5.2 show that 4xxxA alloys emit less H_2 . In addition, it is noted that the addition of $CaCl_2$ reduces H_2 -emissions substantially. The addition of $CaCl_2$ to 6082 alloys reduces H_2 -emissions by a factor of 2.74, whereas adding $CaCl_2$ to 4xxxA alloys reduces H_2 -emissions by 12.7.

Figure 5.3 demonstrates further that sample 6082 without additional $CaCl_2$ differs from the other samples in that its H_2 -emission is not stable at the end of the experiment.

Figure 5.3, and Table 5.2 show the H_2 development using ICEM and 6082 reinforcement, with and without the addition of 4 wt% $CaCl_2$. Figure 5.3 shows that the sample without added $CaCl_2$ has its first registered H_2 -emission after 42 min. A subsequent sharp rise in H_2 concentration persists for about 5 hours before the H_2 concentration begins to convert. The H_2 -emission is not yet stabilised at the end of the experiment and shows a final H_2 concentration of 8.19

$\cdot 10^{-5} \text{H}_2\%/\text{mm}^2$. When CaCl_2 is added, the first H_2 -emission is registered after 45 minutes. The H_2 concentration then follows the upward trend of the sample without added CaCl_2 for the first 2.5 hours before the concentration converts to a greater extent towards a final concentration. The H_2 concentration has stabilised after 5 hours and maintains a concentration of $2.99 \cdot 10^{-5} \text{H}_2\%/\text{mm}^2$ until the end of the experiment.

For the sample consisting of 4xxxA without added CaCl_2 , the first H_2 -emission is registered after 30 min. An almost exponential increase in H_2 emissions follows the next 5 hours before the H_2 -curve stabilises and ends at a final H_2 concentration of $56.89 \cdot 10^{-5} \text{H}_2\%/\text{mm}^2$. For the 4xxxA sample with added CaCl_2 , the first H_2 -emission is registered after 75 minutes. A slight increase in H_2 -emissions follows until 5 hours have passed. The sample shows a final H_2 emission of $4.48 \cdot 10^{-5} \text{H}_2\%/\text{mm}^2$.

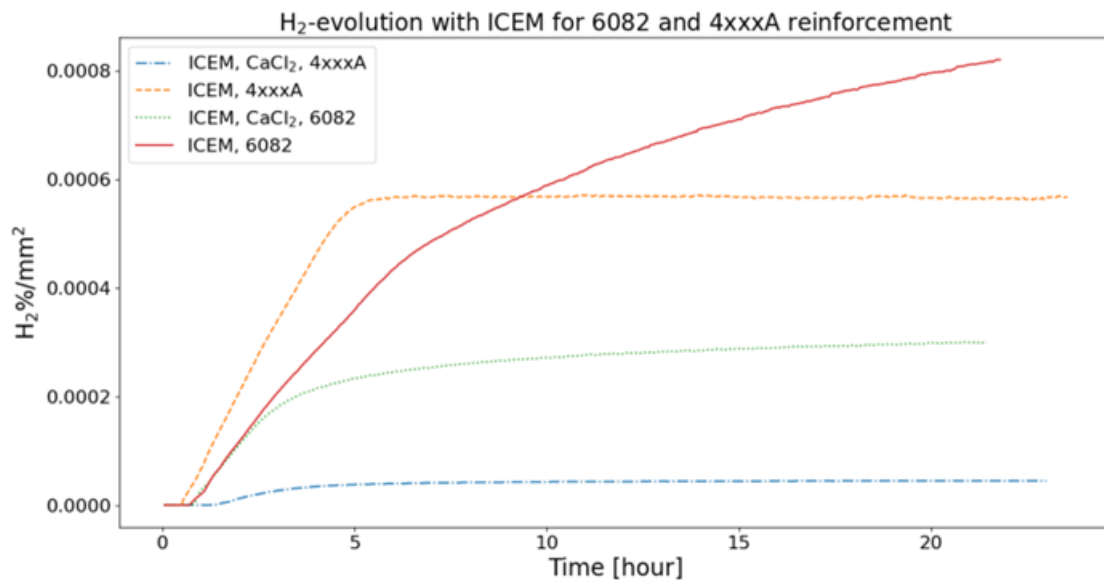


Figure 5.3: H_2 -emission for samples using ICEM. Reinforcement used are 6082 and 4xxxA where one of each sample has added CaCl_2 to the cement paste.

ICEM against CCEM Figure 5.4 compares the H_2 -emission for ICEM and CCEM, using samples where CaCl_2 has been added to the cement paste. The figure and table shows a lower H_2 -emission when using CCEM.

For CCEM, no H_2 -emissions are detected until 5 hours and 3 minutes have passed. This is followed by a gradual increase in H_2 -emissions over the next ten hours. The H_2 -emission curve reaches its reversal point after 10 hours of experimentation and begins to convert. After 15 hours, the H_2 -emission is stabilised, and a final concentration of $1.06 \cdot 10^{-5} \text{H}_2\%/\text{mm}^2$ was determined at the end of the experiment. The H_2 -emission for the ICEM is identical to that described above. Further information of the samples are given in Tabel 5.2.

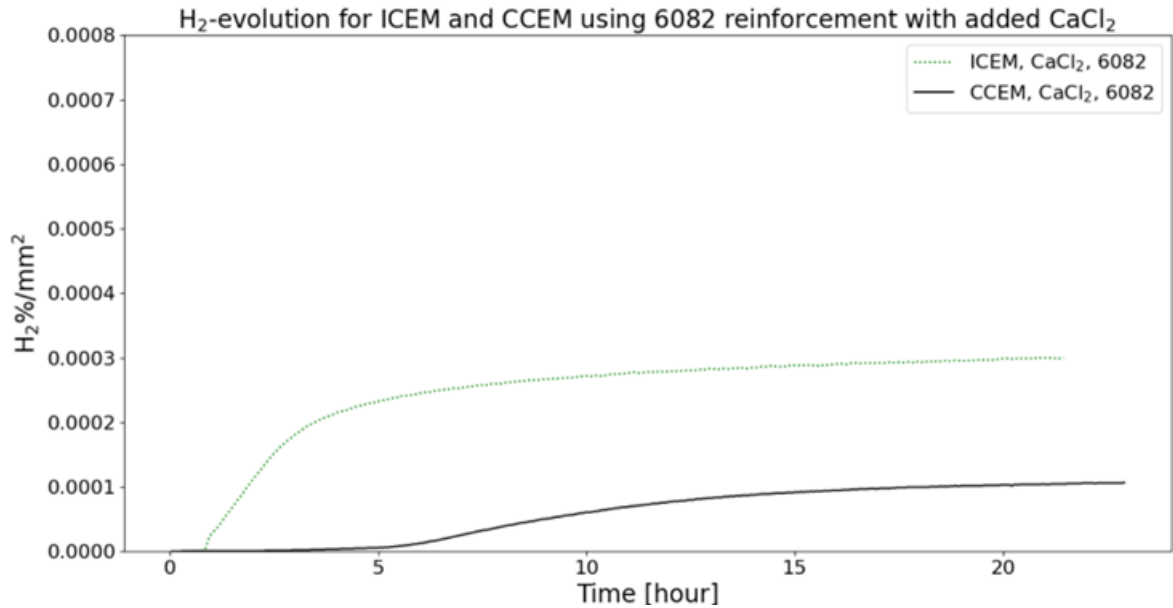


Figure 5.4: GC measurement of H₂-emission for ICEM utilising 6082 reinforcements with and without CaCl₂ as well as H₂-emission for CCEM with added CaCl₂ to the paste.

Comparing H₂-evolution for NaOH and NaSi at pH=11.5

Figure 5.5 shows the H₂ developments for a 6082 reinforcement in a NaOH and NaSi solution with pH = 11.5. The experiments are performed using a Flow system setup. Relevant data are given in Table 5.2.

Figure 5.5 and Table 5.2 illustrate that the 6082 reinforcement develops H₂-emissions in a NaOH solution with pH = 11.5, while H₂-gas is not emitted when the reinforcement is in a NaSi solution with the same pH. Table 5.2 shows that the 6082 reinforcement has its first H₂-emission after 24 minutes in a NaOH solution. After an initial exponential H₂ registration, the GC registers a gradual development in H₂-emissions over the next 13 hours. After 13 hours and 24 minutes, the H₂-emission curve stabilises at a value of $2.58 \cdot 10^{-5}$ H₂/mm² where it remains until the end of the experiment.

In contrast to the 6082 reinforcement NaOH solution, the reinforcement in the NaSi solution shows no registered H₂-emissions during the experiment.

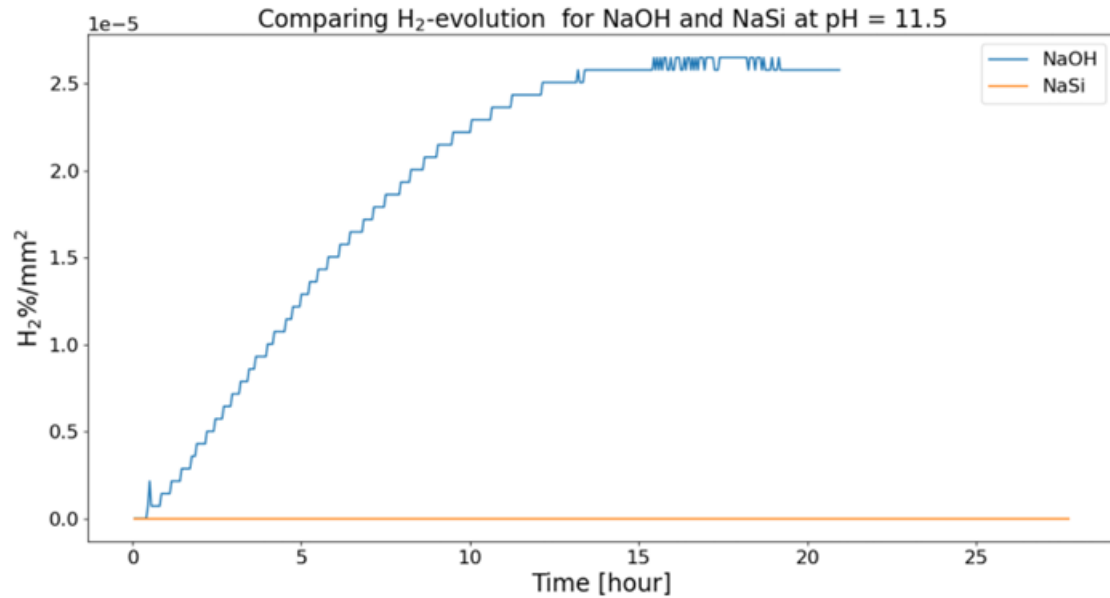


Figure 5.5: GC measurement of H₂-emission for a 6082 reinforcement in NaOH and NaSi solution at pH=11.5, respectively.

Table 5.2: First detected H₂-emission and Final H₂-emission for the GC samples

Samples	First H ₂ -emission[<i>min</i>]	Final H ₂ -emission [<i>H₂%/mm² · 10⁻⁵</i>]
Stationary setup		
Hyaloclastite, CaCl ₂ , 6082	50	4.41
Estonian CC , CaCl ₂ , 6082	250	42.6
Flow system setup		
Hyaloclastite, CaCl ₂ , 6082	39	7.70
OPC (CCEM), CC, CaCl ₂ , 6082	135	10.66
ICEM, CaCl ₂ , 6082	45	29.96
ICEM, CaCl ₂ , 4xxxA	75	4.48
ICEM, 6082	42	81.99
ICEM, 4xxxA	30	56.89
NaOH (pH=11.5), 6082	24	2.58
NaSi (pH=11.5), 6082	-	0

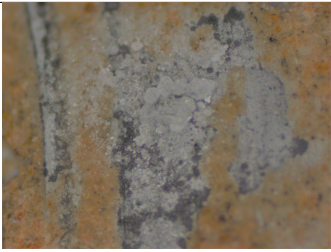
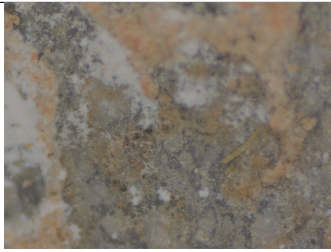
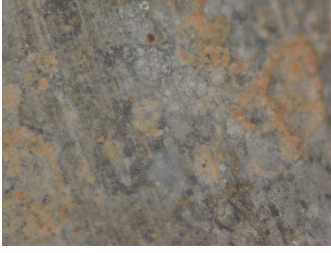
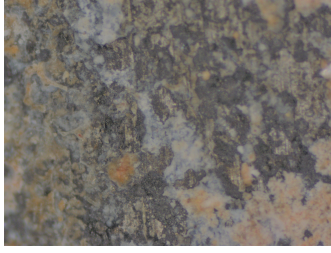
5.2 Surface analysis

5.2.1 Stereo microscope

Table 5.3 shows stereoscopic images from the reinforcement surface of the 6082 and 4xxxA reinforcements, respectively, after curing in cement paste with and without added CaCl₂ for 28 days. The photos were taken at a magnification of 5X after the reinforcements had been cut out of the concrete structures. The grey colour in each image is the surface of the reinforcement metal, while the brown colour is due to residues of the cement on the reinforcement surface. The white colour in the pictures is due to the formation of products at the interface between reinforcement and cement. The images in Table 5.3 show differences in emitting based on the use of CaCl₂ in the form of :

1. The addition of CaCl_2 results in the development of crystalline material at the reinforcement-cement interface. The white crystalline substance was not present in samples to which CaCl_2 had not been added.
2. The reinforcing surface of samples cured in cement paste for 28 days without the addition of CaCl_2 had a deeper shade of grey. Furthermore a white product was observed on the reinforcement interface.
3. Samples with added CaCl_2 had a larger proportion of concrete residues on the surface.

Table 5.3: Stereo microscope images of the surfaces of 6082 and 4xxxA reinforcement after 28 days of cure in cement pastes with and without added CaCl_2 .

	CaCl_2	Without CaCl_2
6082, H_2O		
4xxxA, H_2O		

5.2.2 SEM surface analysis

Figure 5.7 depicts considerable alterations in the surface topography and characteristics of samples to which CaCl_2 has been added. SEM image 5.7a reproduces an overall picture of the surface of the reinforcements taken at a magnification of 100x. From the SEM image in 5.7a, it is evident that the topography of the surface varies significantly between different regions. The regions in the upper right corner of the SEM image and the middle depict surfaces with a significant topographical variation that portrays a mountainous appearance.

500x magnification SEM pictures 5.7b and 5.7c both depict surfaces with identical characteristics. When CaCl_2 is applied to reinforcing surfaces, the formation of a surface with pronounced topographical variances is a reoccurring phenomenon. In contrast to areas with significant topographical differences, a flat area is identified in the SEM image reproduced in 5.7a in the lower right part of the image. A further frequent observation for reinforcing surfaces with CaCl_2 added to the cement mix is the presence of aggregates. In the centre of SEM picture 5.7a, examples of such aggregates are visible.

Figure 5.8 shows pictures of the surface of reinforcements where CaCl_2 has not been added to the cement paste. The SEM images reproduce a surface with slight variations in character. The SEM image in Figure 5.8a taken at a magnification of 100x presents an overall image of the surface of reinforcements hardened in CaCl_2 -free cement paste. The image depicts a flat surface with small snake-shaped slopes. In contrast to the remainder of the surface seen in Figure 5.8a, small white spots are visible in the centre of the SEM picture, along the left edge, and in the upper right corner. The SEM image 5.8c reveals that these white regions are rougher and have more topographic diversity. Cracks on the reinforcement surface are another characteristic of all reinforcements cured with CaCl_2 -free cement paste. Figure 5.8b depicts a 400x magnification SEM picture in which the crack formations are visible.

When inspecting CaCl_2 -free surfaces with a higher magnitude, a more significant variation in structure is observed. Figure 5.6 shows the SEM image of a 6082 surface without added CaCl_2 . Picture 5.6a shows a surface consisting of many small spikes. In SEM image 5.6b, on the other hand, tiny crystals are observed on the reinforcement surface.

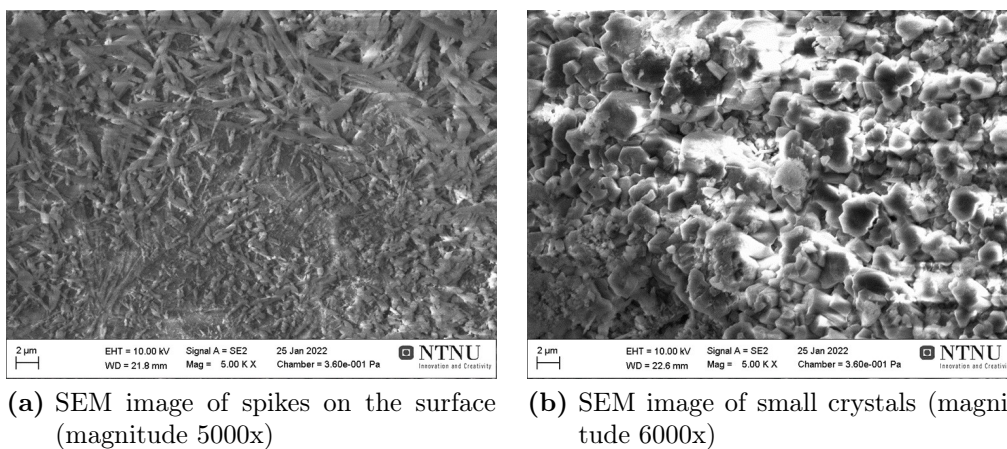
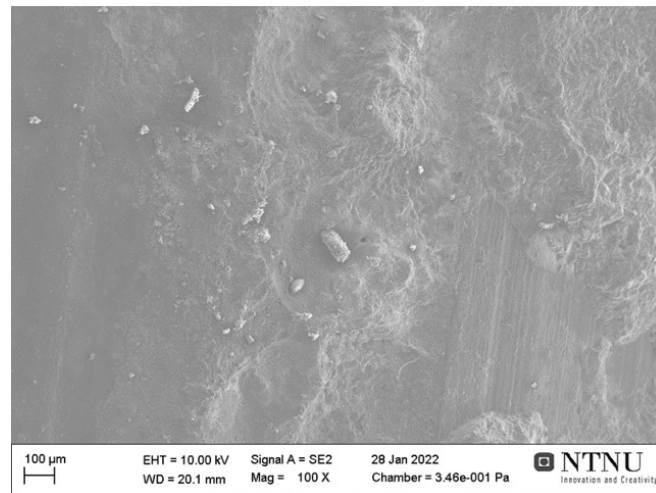
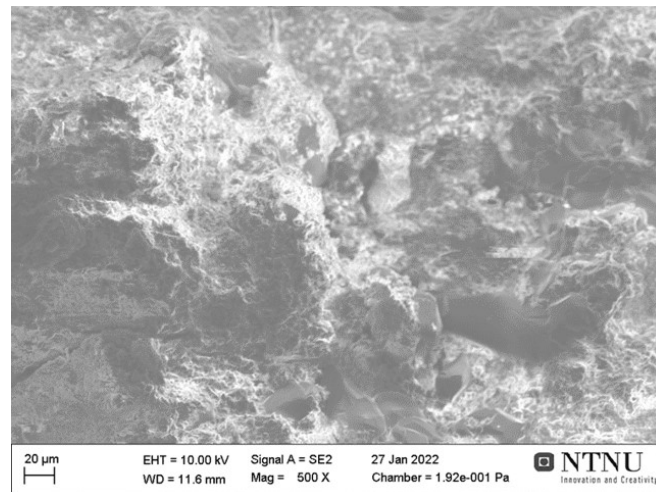


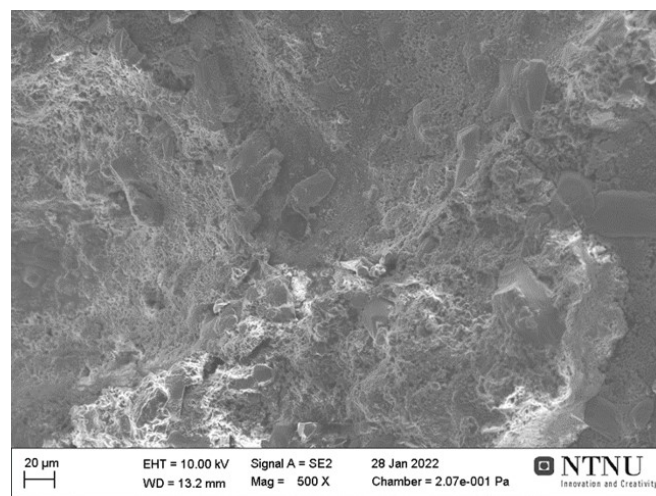
Figure 5.6: SEM images of the reinforcement in concrete structures without added CaCl_2 with a large magnitude.



(a) SEM image 100x magnitude

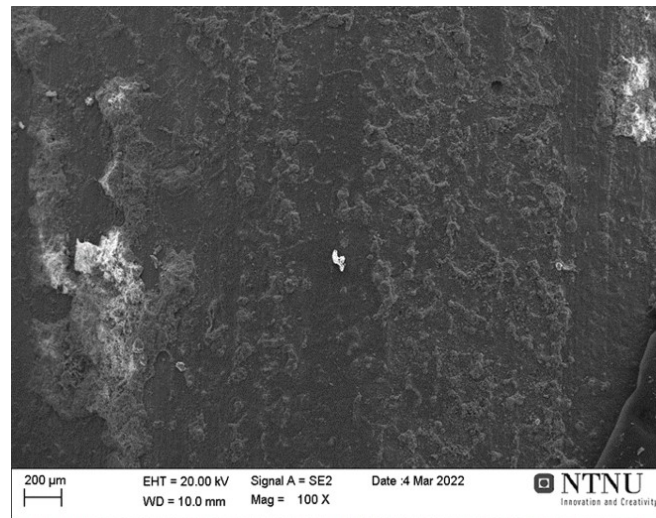


(b) SEM image 500x magnitude

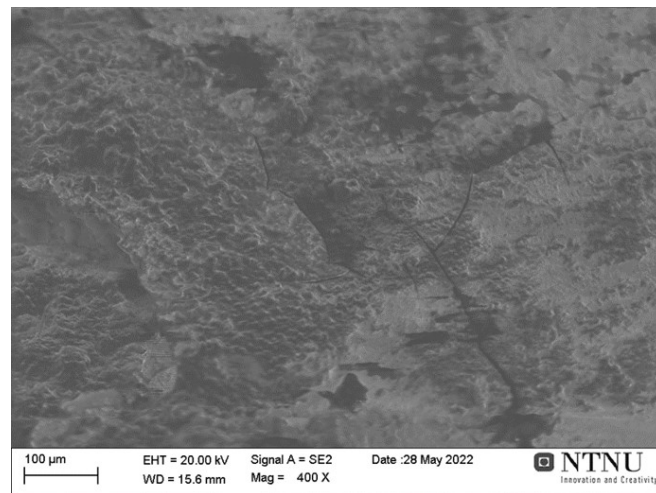


(c) SEM image 500x magnitude

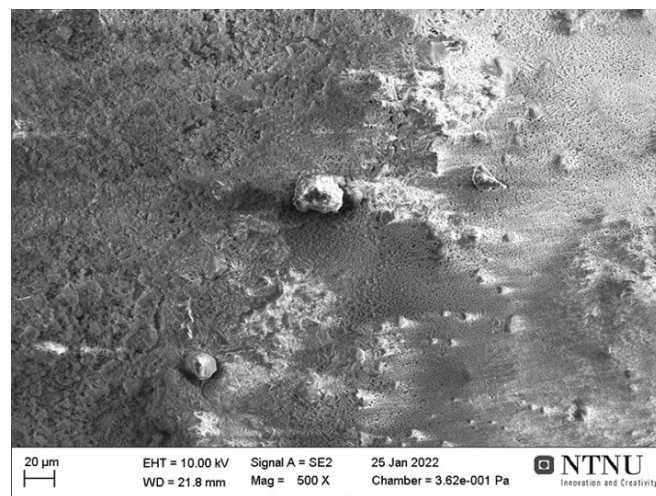
Figure 5.7: SEM images of the reinforcement in concrete structures with added CaCl_2 .



(a) SEM image 100x magnitude



(b) SEM image 400x magnitude



(c) SEM image 500x magnitude

Figure 5.8: SEM images of the reinforcement in concrete structures without added CaCl_2 .

5.2.3 EDS for surface analysis

This subsection presents the findings of the EDS-analysis conducted on the reinforcing surface. In order to provide a clear overview of the tendencies discovered by EDS, the thesis will provide in greater detail two of the EDS studies that illustrate trends observed in all samples. The initial provided EDS-analysis is performed on the surface of the 6082 reinforcement after it has been cured in a cement solution containing CaCl_2 . In contrast, the second presented EDS-analysis provides the results from the surface of the 6082 reinforcement that has been cured in a CaCl_2 -free cement paste. Appendix C.4 contains additional data from the EDS-analysis.

Figure 5.9 and Tables 5.4, 5.5, and 5.6 provide SEM pictures indicating where EDS analyses were performed and elemental compositions of a 6082 reinforcement cemented in cement paste with CaCl_2 addition. This EDS study was selected due to the fact that it shows SEM picture, which reveals significant surface area variation.

Table 5.4 reveals the element composition of Area 1 in the SEM picture represented in Figure 5.9. The studied area deals with the aggregates depicted in the SEM pictures 5.7a and 5.7c. High quantities of the elements O and Ca are reported in Table 5.4. Furthermore, the EDS analysis alludes to considerable levels of C. Also identified are Al and Si, as well as Mo, Cl, Ca, and K residues.

Table 5.6 presents the elemental composition determined by EDS analysis of region 3 in Figure 5.9. The study is based on Section 5.2.2 description of a region with significant topographical changes. Table 5.6 contains element compositions that correspond to the same composition ratios as Table 5.4. Similar to the EDS study of Area 1, Ca and O are the most abundant elements in this area. Furthermore, the EDS analysis identifies considerable levels of C, Al, and Si. The analysis further characterises minute quantities of Mo, Cl, and K.

The composition of the reinforcement's Area 2 with a flat topology is reflected in Table 5.5. The EDS analysis identifies significant quantities of O and Al. The analysis additionally characterises C.

Table 5.4: The elemental composition in Area 1 illustrated in Figure 5.9, determined by EDS-SEM for 6082 cement-hardened reinforcement with additional CaCl_2 .

Element	[wt%]	[at%]	Error (σ) [wt%]
C	19.87	31.46	8.48
O	39.93	47.46	8.60
Al	5.78	4.07	5.12
Si	5.76	3.90	5.17
Mo	2.33	0.46	17.82
Cl	2.06	1.11	10.28
K	0.99	0.48	24.81
Ca	23.29	11.05	4.76

Table 5.5: The elemental composition in Area 2 shown in Figure 5.9, determined by EDS for 6082 cement-hardened reinforcement with additional CaCl_2

Element	[wt%]	[at %]	Error (σ) [wt %]
C	16.08	24.06	10.39
O	43.84	49.24	6.10
Al	40.08	26.70	3.31

Table 5.6: The elemental composition in Area 3 depicted in Figure 5.9, determined by EDS for 6082 cement-hardened reinforcement with additional CaCl_2

Element	[wt%]	[at%]	Error (σ) [wt%]
C	10.76	18.54	9.95
O	41.29	53.41	8.60
Al	9.89	7.58	4.84
Si	5.69	4.19	5.74
Mo	2.20	0.47	24.42
Cl	3.21	1.87	8.69
Ca	26.96	13.92	4.82

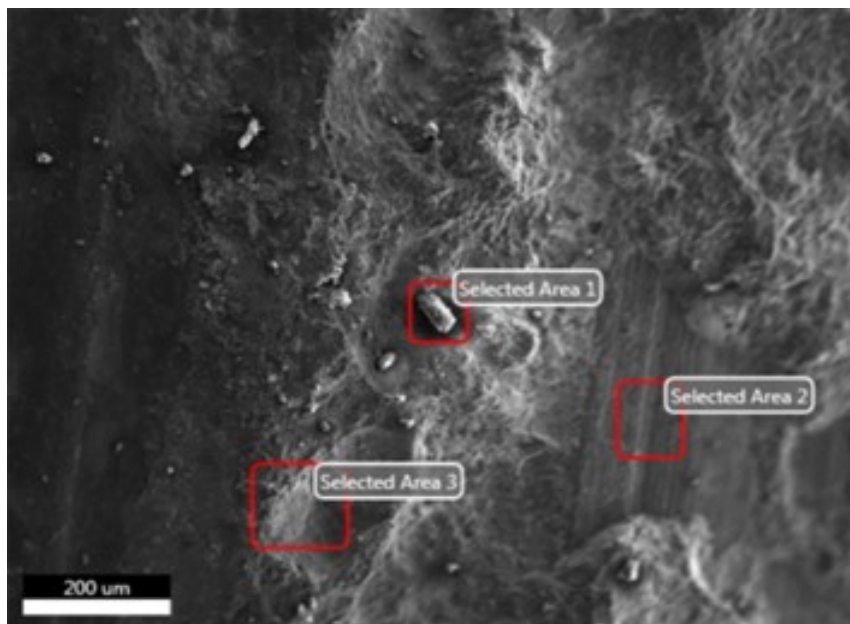
**Figure 5.9:** SEM picture depicting area for EDS analysis and accompanying EDS spectrum.

Table 5.7: Element composition from EDS-analysis taken from Point A in Figure 5.10.

Element	[wt%]	[Nor. wt%]	[at%]	Error (σ) [wt%]
O	54.37	57.09	68.85	6.45
Al	20.90	21.95	15.70	1.03
Ca	12.25	12.86	6.19	0.39
C	3.83	4.02	6.46	0.82
Si	2.84	2.98	2.05	0.15
Mg	0.47	0.49	0.39	0.06
F	0.23	0.25	0.25	0.13
Cu	0.23	0.24	0.07	0.04
Fe	0.11	0.12	0.04	0.03

Table 5.8: Element composition from EDS-analysis taken from Point B in Figure 5.10.

Element	[wt%]	[Nor. wt%]	[at%]	Error (σ) [wt%]
O	46.47	56.57	68.76	5.40
Al	33.99	41.38	29.82	1.65
Ca	0.92	1.12	0.54	0.06
F	0.56	0.69	0.70	0.20
Si	0.20	0.25	0.17	0.04

Table 5.9: Element composition from EDS-analysis taken from Point C in Figure 5.10.

Element	[wt%]	[Nor. wt%]	[at%]	Error (σ) [wt%]
O	47.20	55.27	68.54	5.64
Al	31.46	36.84	27.09	1.53
Cl	2.05	2.39	1.34	0.10
Si	1.53	1.79	1.26	0.10
Ca	1.48	1.74	0.86	0.08
K	1.21	1.42	0.72	0.07
Fe	0.46	0.54	0.19	0.05

Figure 5.10 and tables 5.8, 5.7, and 5.9 depict the EDS spectra and identified element compositions on a 6082 reinforcing surface cured in a CaCl_2 -free cement paste. The EDS study is based on the SEM image in Figure 5.8a, and involves the investigation of three surface spots. In conclusion, the EDS analysis reveals high levels of O and Al.

Table 5.7 displays the elemental composition of Point A. Point A is located on one of the bright surface regions indicated in Subsection 5.2.2. The table displays elevated levels of O and Al. Additionally, notable levels of Ca are recorded. EDS analysis also reveals trace quantities of C, Si, Mg, F, Cu, and Fe.

Table 5.8 depicts the elemental composition of Point B. The EDS analysis reveals high levels of O and Al. The study also detects Ca, Si, and F residues.

The results of Point C on snake-like slopes, which is given in Subsection 5.2.2, are displayed in 5.9. Similar to other analyses on the surface of the reinforcement, substantial quantities of O and Al are detected. In addition, the EDS analysis detects Cl, Si, Ca, K and Fe residues.

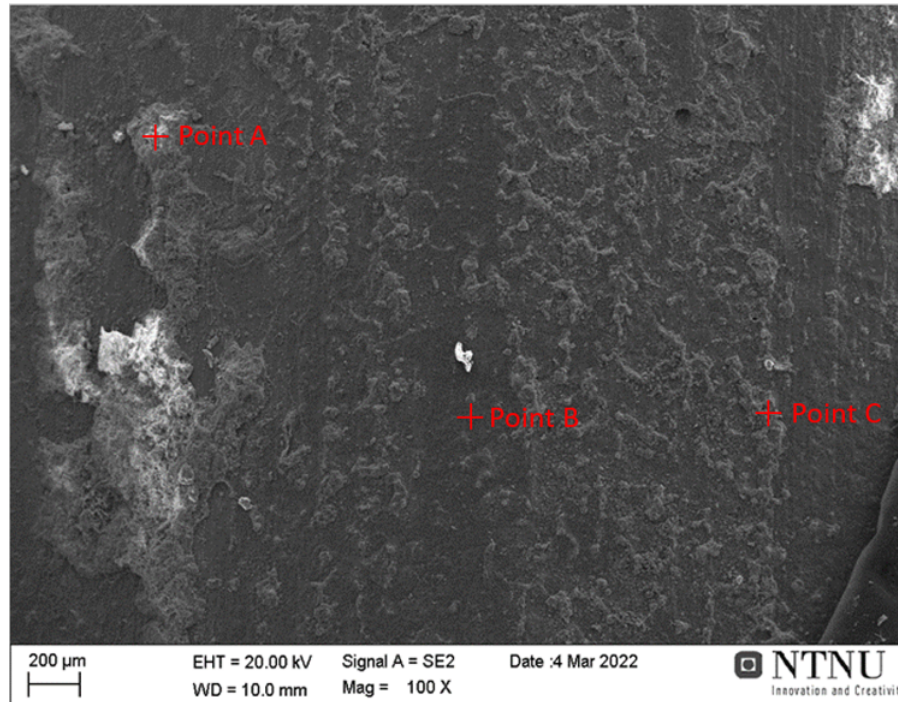


Figure 5.10: Depiction of where the analysis were taken.

5.3 Interface analysis

This subsection presents the findings of the interface analysis. These subsections contain the findings from LM, SEM, and EDS.

5.3.1 LM and SEM

Figure 5.11 shows the cross-sectional interface of the reinforcements 6082 (a and b) and 4xxxA (c and d) after curing in a freshwater cement paste, with and without added CaCl_2 . The images were taken with a LM with a magnification of 5x, where the reinforcements have been carved out of the concrete structure, cut at a cross-section and laid in epoxy, as described in Subsection 4.5.1. In Figure 5.11, the lighter parts of the image will be the reinforcement, whilst the darker grey part will be epoxy. Furthermore, the image's darkest parts will be caused by components other than reinforcement or epoxy.

Figure 5.11 reveals that reinforcements that were layered in a cement paste without added CaCl_2 (b and d) were impacted by the paste to a greater extent, as evidenced by more significant topographical differences at the cross-sectional interface. In addition, pitting is observable in the reinforcement of CaCl_2 -free

samples.

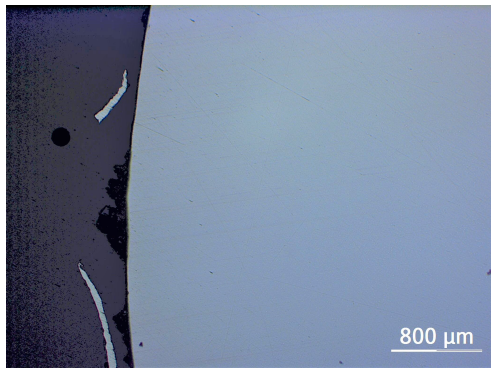
In general, the addition of CaCl_2 results in a smoother, less impacted cross-sectional interface, which reduces the topographic and pitting variations, shown in image 5.12a and 5.12c. Nevertheless, small accumulations and abnormalities are observable for both the 6082 (5.12a) and 4xxxA (5.12c) reinforcement, indicating that the reinforcement is not entirely unaffected under these conditions. Figure 5.12 depicts the same tendencies as Figure 5.11 but on a less pronounced scale. Compared to Figure 5.11, Figure 5.12 displays a more significant topographical difference for samples to which CaCl_2 was not added. However, the topographic difference is not as apparent in 5.11b and 5.11d as in 5.12b and 5.12d, and there are no apparent signs of pitting. In addition, samples 5.11a and 5.11c correspond to a cross-sectional interface that is even less impacted by the cement paste's hardening than samples 5.12a and 5.12c.

Figures 5.11 and 5.12 indicate that the absence of CaCl_2 results in a deep dark coating in the cross-section of the reinforcement-concrete interface, which cannot be observed in reinforcements to which CaCl_2 has been added. In Figures 5.12b, 5.12d, 5.11b, and 5.11d, the coating is noticed as a dark, continuous layer separating the boundary cross-section between the reinforcement, which is light in colour, and the epoxy, which is dark in colour.

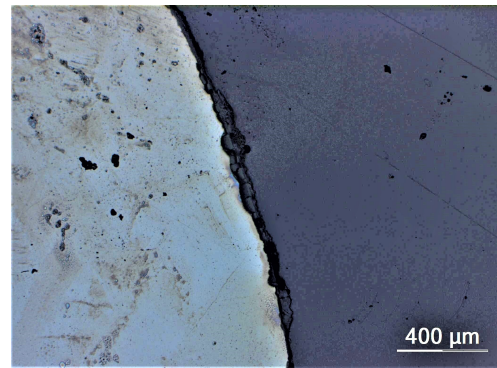
Table 5.10 shows the thickness of the coating developed at the interface of the reinforcement and the cement for samples in which no CaCl_2 was added to the cement paste. The values in the table were determined by measuring the thickness of the coating 6 times for each sample using the LM image. The measurements were conducted in reinforcing regions devoid of pitting because the coating thickness in these areas was larger than the average value. The table's average thickness and standard deviation were determined using the 6 individual measurements. Appendix C.2 depicts the locations where measurements were taken for each sample.

Table 5.10: Oxidelayer measured for the different samples.

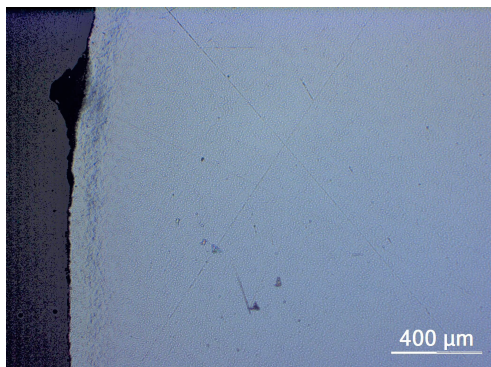
Sample	Thicknes of oxide layer [μm]
6082, Seawater	57.19 ± 9.92
6082 , H_2O	65.50 ± 8.81
4xxxA, Seawater	29.05 ± 1.39
4xxxA, H_2O	105 ± 55.31



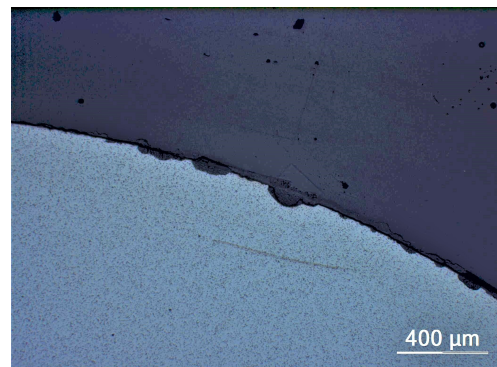
(a) CaCl_2 , Seawater, 6082



(b) Seawater, 6082

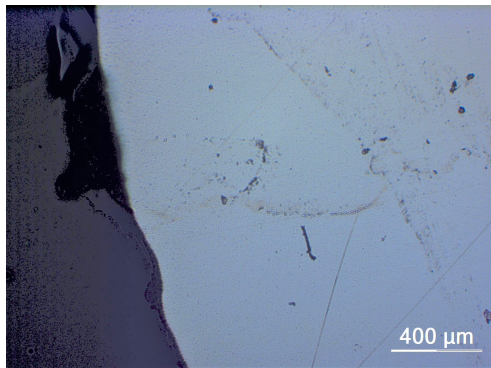
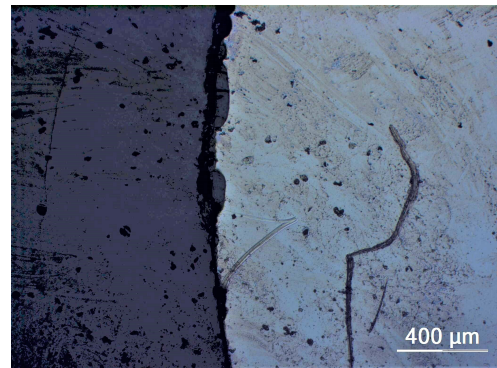


(c) CaCl_2 , Seawater, 4xxxA

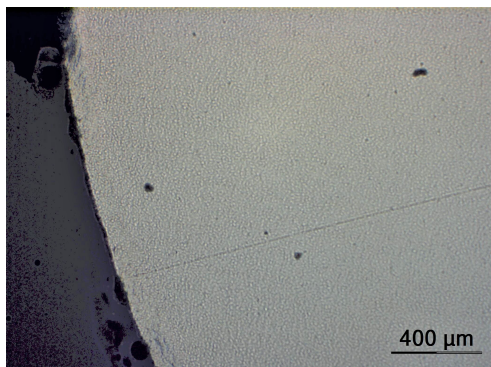
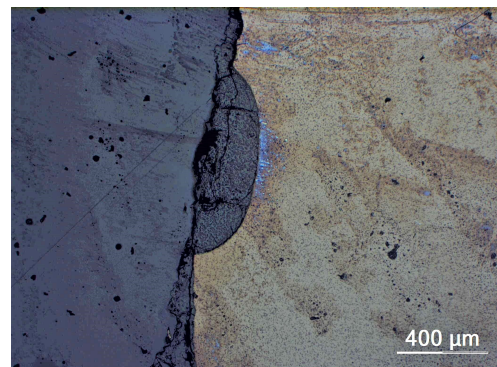


(d) Seawater, 4xxxA

Figure 5.11: Interface between the concrete and the reinforcements of the samples where seawater was used, taken with a LM at a magnification of 5x.

(a) CaCl_2 , Freshwater, 6082

(b) Freshwater, 6082

(c) CaCl_2 , Freshwater, 4xxxA

(d) Freshwater, 4xxxA

Figure 5.12: The figure shows the interface between the concrete and the reinforcements of the samples where freshwater was used, taken with a LM at a magnification of 5x.

In addition, the LM images in Figures 5.12b, 5.12d, 5.11b, and 5.11d reveal a coating with an inhomogeneous (anisotropic) characteristic in which the coating thickness changes throughout the cross-sectional interface. The SEM pictures in Figure 5.13 provide a more detailed depiction of the features of the interface coating. In Figure 5.13, the surface coat has a grey tone between the reinforcement's light grey tone and the epoxy's dark grey tone. The creation of cracks between the reinforcement and surface coating, is a repeating pattern for the surface coating depicted in Figures 5.13a, 5.13b, 5.13c, and 5.13d. In addition, the SEM images of Figures 5.13b and 5.13d reveal several vertical cracks spreading from the coating's surface to the reinforcement.

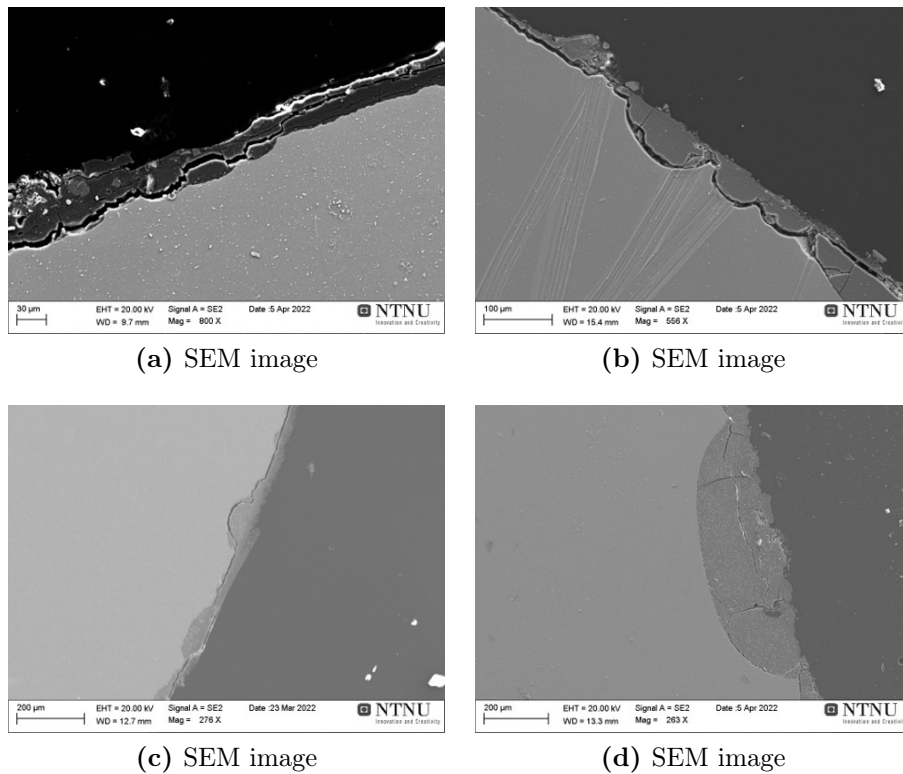


Figure 5.13: SEM Images of the cross-sectional interface between reinforcement and concrete structures without added CaCl_2

When CaCl_2 is not supplied, LM and SEM pictures reveal that clusters migrate beyond the cross-sectional interface between the reinforcement and the surface coating. From the SEM pictures in Figure 5.13, white dots can be noticed in the pitting's surface layer. Increasing the magnification of the LM (100x) and SEM images make it possible to identify these white dots as clusters. Figure 5.14 depicts the LM and SEM images of the clusters, which depict a 6082 reinforcement and a 4xxxA reinforcement, respectively, both cured in a cement paste without adding CaCl_2 . The photos captured by LM show that the clusters appear darker than the reinforcement but lighter than the surface layer (5.14a and 5.14c). The clusters more grey than both the reinforcement and the surface coating in the SEM images (5.14b and 5.14d). The activity surrounding the interface and the frequency of these clusters are more significant for the 4xxxA reinforcement than for the 6082 reinforcement, as depicted in Figure 5.14. Comparing photos 5.14a and 5.14b with 5.14c and 5.14d reveals that the cluster concentration is greater above and below the interface for the 4xxxA reinforcement. In addition, clusters were not found in samples containing CaCl_2 .

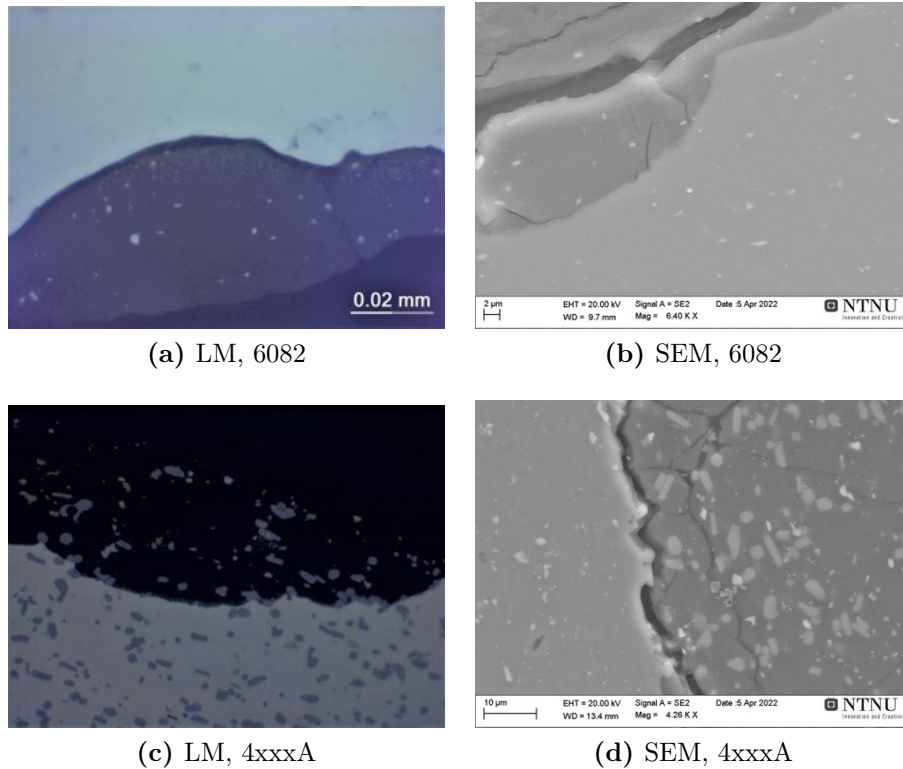


Figure 5.14: SEM Images of the cross-sectional interface between reinforcement and concrete i structures without added CaCl_2

5.3.2 EDS for interfacial analysis

This subsection covers the most significant EDS-analysis results. EDS was performed to understand the composition and distribution of components displayed in the SEM pictures.

Figure 5.15 depicts an EDS-analysis conducted on a cross-sectional interface for a sample containing 6082 reinforcement and a CaCl_2 -free cement paste. The result represented through an SEM image that specifies the location of analysis, and a table containing the element composition.

Table 5.11 provides the elemental composition at Point A, placed on the surface coating at the previously reinforcement and concrete interface. The EDS analysis indicates a high quantity of O and aluminium(Al). In addition, the EDS analysis indicates that some levels of calcium(Ca), silisium(Si), manganese(Mn), potassium(K) and natrium(Na) are present.

Table 5.11: Elemental composition found by EDS of the cross-sectional interface of 6082 reinforcement cured in CaCl_2 -free cement paste. The analysis was carried out in the point depicted Point A shown in Figure 5.15.

Element	[wt %]	[Nor. wt %]	[at %]	Error (σ) [wt%]
O	35.10	50.62	64.22	4.16
Al	29.00	41.82	31.47	1.41
Ca	2.61	3.76	1.90	0.11
Si	1.41	2.04	1.47	0.09
Mn	0.61	0.88	0.32	0.05
K	0.32	0.47	0.24	0.04
Na	0.29	0.42	0.37	0.05

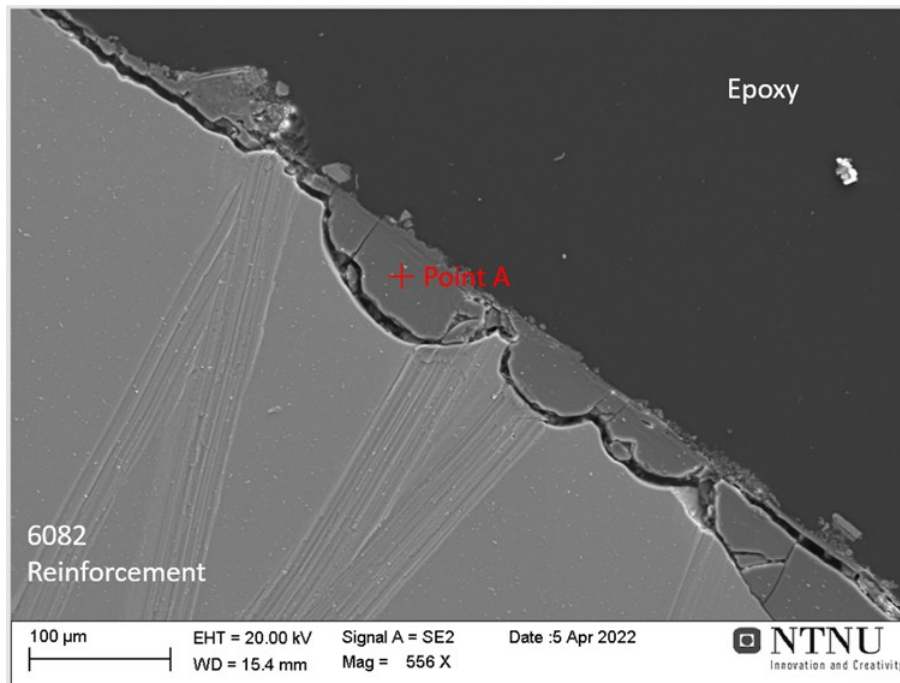


Figure 5.15: SEM image depicting the point of EDS-analysis. The EDS-analysis was taken on the layer in the interface between the 6082 reinforcement and epoxy.

EDS analysis of the clusters

Figure 5.16 depicts an EDS-analysis of the cross-sectional interface of 4xxxA reinforcement that has hardened in a cement paste free of CaCl_2 . The results are displayed as a SEM image that depicts the analysis points. In addition, Tables 5.12 and 5.13 show the element composition derived from the analysis.

Table 5.12 show the outcomes of the EDS analysis conducted at Point A of the SEM picture 5.16. The analysis is conducted on one of the observed clusters outside the reinforcement. the table reveals that the EDS-analysis detects a substantial quantity of Si at this location. In addition, quantities of O, C, and Al have been discovered. EDS also detects Cu and Fe residues.

Table 5.13 refers to the element composition found at EDS in Point B on the SEM image 5.16. The analysis was performed on one of the observed clusters in the 4xxxÅ reinforcement cured in cement paste without added CaCl_2 . At this point, the detected element composition observes a dominant Al concentration. Furthermore, considerable amounts of C are detected. The EDS-analysis also detects Fe, Si and Cu. Small amounts of O, Mn and Cr were also found in the analysis.

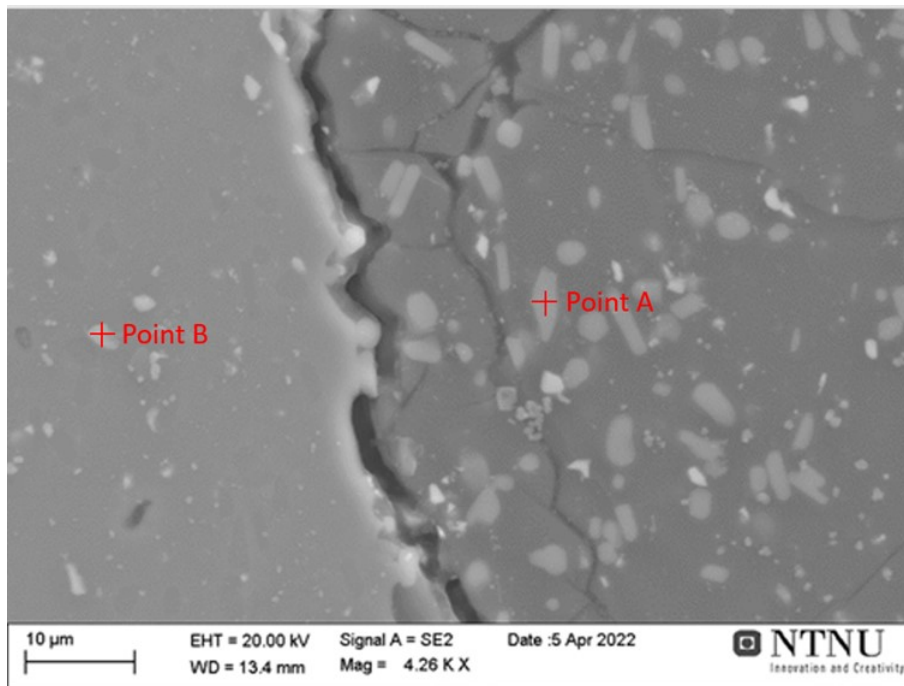


Figure 5.16: SEM image specifying location of EDS-analysis.

Table 5.12: Element composition found by EDS-analysis of the cross-sectional interface of 4xxxÅ reinforcement cured in CaCl_2 -free cement paste. The analysis was carried out in Point A depicted in Figure 5.16.

Element	[wt %]	[Nor. wt %]	[at %]	Error (σ) [wt%]
Si	52.62	63.27	49.89	2.27
O	11.46	13.77	19.07	1.51
C	10.59	12.73	23.48	1.73
Al	6.97	8.38	6.88	0.36
Cu	0.84	1.01	0.35	0.06
Fe	0.69	0.83	0.33	0.05

Table 5.13: Element composition found by EDS-analysis of the cross-sectional interface of 4xxxA reinforcement cured in CaCl_2 -free cement paste. The analysis was carried out in Point B depicted in Figure 5.16.

Element	[wt %]	[Nor. wt %]	[at %]	Error (σ) [wt%]
Al	75.58	73.18	64.95	3.63
C	13.82	13.38	26.68	2.21
Fe	4.23	4.10	1.76	0.14
Si	4.23	4.10	3.49	0.21
Cu	3.05	2.95	1.11	0.12
O	0.98	0.95	1.42	0.23
Mn	0.83	0.80	0.35	0.05
Cr	0.56	0.54	0.25	0.04

EDS-analysis for interface with added CaCl_2

Table 5.14 quantifies the elemental composition of the cross-sectional interface, while the SEM picture in Figure 5.17 indicates the exact location for the analysis of the 6082 reinforcement cured in a cement paste containing CaCl_2 . Table 5.14 displays elevated levels of C and O. In addition, accurate levels of Ca and Al are determined. EDS analysis further reveals the presence of Si residues.

Table 5.14: Element composition of Point A in Figure 5.17, found by EDS-analysis.

Element	[wt %]	[Nor. wt %]	[at %]	Error (σ) [wt%]
C	35.26	43.72	57.84	4.42
O	23.93	29.66	29.45	3.18
Ca	10.72	13.29	5.27	0.41
Al	5.96	7.39	4.35	0.30
Cl	2.34	2.90	1.30	0.12
Si	1.94	2.41	1.36	0.12
Na	0.31	0.38	0.26	0.05
Mg	0.20	0.25	0.16	0.04

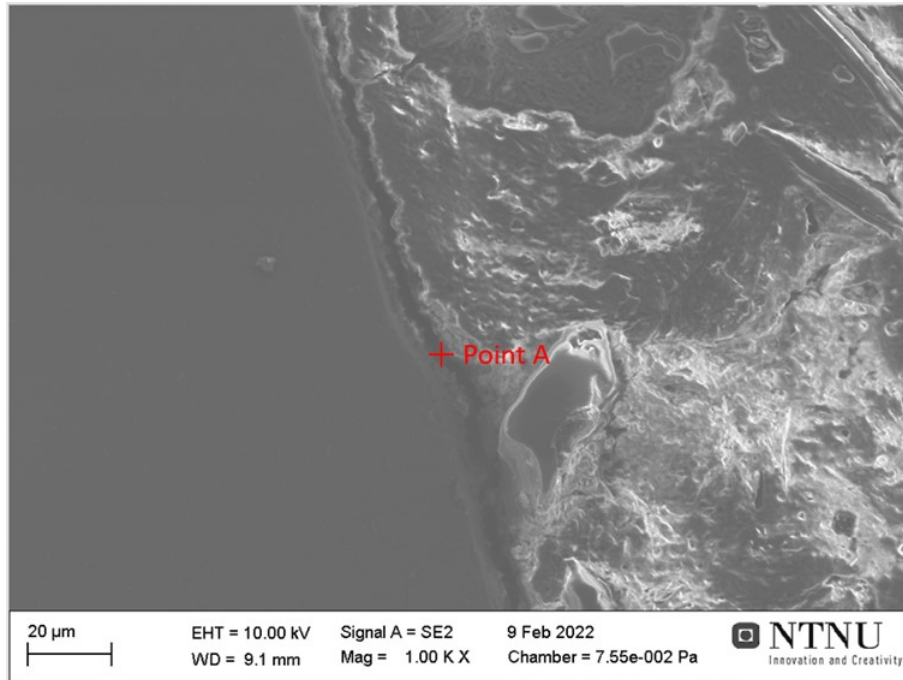


Figure 5.17: SEM image specifying location (Point A) for EDS-analysis. The analysis is taken in the interface between 6082 reinforcement and cement for samples with added CaCl_2 .

5.4 Mechanical results

This section presents the results of the mechanical tests in the master's thesis. The mechanical properties of the cement composition were found by performing pull-out tests which gave the bond strength of the concrete structure in form of a bond stress-slip diagram.

Figures 5.18 and 5.20 show that the bond stress-slip curves end at different displacement values. This is because the experiments were terminated for safety reasons after the *Decreasing phase* (descending line) was concluded, and the *Residual phase* (horizontal line) had begun.

5.4.1 Pull-out test for 6082 and stainless steel smooth bars

Figure 5.18 illustrates the bond stress results from pull-out tests for smooth bars made of 6082 and stainless steel. The splitting bond stress values (τ_{cr}) for each parallel are listed in Table 5.15. The results demonstrate that the smooth 6082 rods have a higher bond stress value than the stainless steel bars, where each parallel 6082 rod has a higher bond stress value than the values obtained from stainless steel. In addition, Figure 5.18 illustrates that the bond stress of the 6082 samples decreases rapidly when the reinforcement is displaced. *6082 Parallel 1* differs from the other two parallels due to its lower bond tension.

Stainless steel Parallel 3 corresponds to the same displacement pattern as the 6082 samples, whereas the bond stress value of *Stainless steel Parallel 1* reduces

marginally with displacement. *Stainless steel Parallel 2* has the lowest bond stress values and differs from the other parallels in that the bond stress does not decrease as the reinforcement is moved.

Figure 5.19 depicts rods of 6082 and stainless steel surface following the pull-out test. The surface appearance of 6082 and stainless steel rods differ significantly, as depicted in the images.

In contrast to the stainless steel rods, the surface of the 6082 bar is covered with a uniform covering of light brown concrete. An undamaged surface is observed in spots where the concrete layer has been scraped away. In terms of surface roughness, there were no discernible variations between the concrete-hardened and unhardened portions of the rod. The surface of 6082 bar is shown in Figure 5.19a.

After being exposed to the pull-out test, the stainless steel bar's shining surface is essentially unaffected. The surface roughness of concrete-laid and non-concrete-laid rod components was not discernible when inspected by touch. Small amounts of unevenly dispersed concrete residues are observable upon closer inspection of the surface of the stainless steel bar. The stainless steel rod surface is depicted in Figure 5.19b.

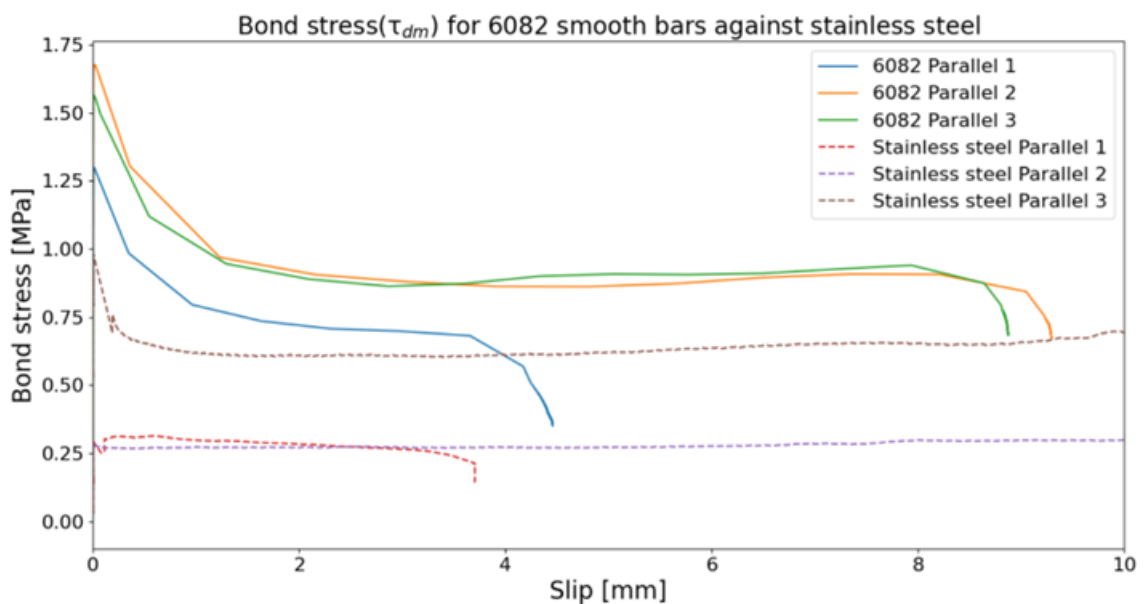


Figure 5.18: Bond stress τ_{dm} for smooth bars of 6082 and stainless steel.

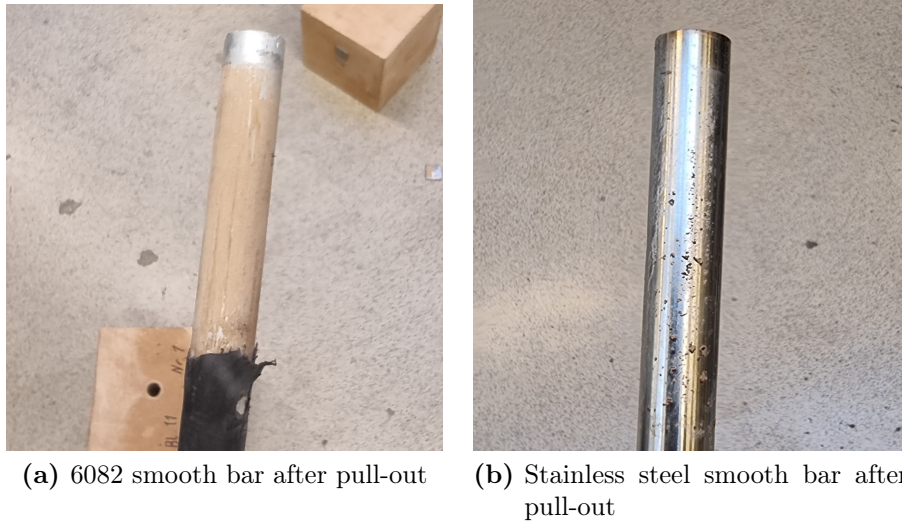


Figure 5.19: Surface of 6082 and stainless steel smooth bars after pull-out.

5.4.2 Pull-out test for 6082 smooth bar and L-shape profiles

Figure 5.20 illustrates the bond stress dependency of reinforcement shape by contrasting 6082 reinforcements of smooth bars with an L-shaped profile. The highest registered bond stress for each sample is further given in Table 5.15. The figure indicates that smooth bars have higher bond stress than L-shaped profiles, with all smooth bar parallels having a higher bond stress value than L-shaped profiles. In contrast to the smooth bar, the L-shaped profile does not have the same bond stress reduction when the reinforcement is displaced.

In addition, the development of bond stress during the movement of L-shaped profiles differs from that of smooth bars in that bond stress increases before progressively decreasing, resulting in a concave bond stress curve. Furthermore, the bond stress values of *L-shape profile Parallel 3* are higher than those of the other parallels.

To better understand the interplay between the reinforcement and the concrete cube, the cube was split, and the imprint was examined. Figure 5.21a depicts the reinforcing and concrete impression of the 6082 bar and L-shape. Figure 5.22, which illustrates the concrete imprint of the 6082 bar and the L-shape reinforcement, allows for a deeper examination of the concrete imprints. Observations from the impressions include a change in colour to a lighter brown at the interface of the reinforcement and concrete, as well as the observation of large and small air bubbles.

Figure 5.21a demonstrates a significant change in colour between the portion of the reinforcement that was in direct contact with the concrete and the part of the bar that had tape between it and the concrete. In Figure 5.21b, areas of the split concrete block that have been in direct contact with the L-shaped reinforcement exhibit different colour difference as parts of the block that have

not been in contact with the reinforcement. Regarding the reinforcing bar, it is seen that the split sample positioned on the image's left has a more pronounced colour difference.

Numerous large air bubbles can be seen in the impressions of the bar and the L-shaped reinforcement. Large air bubbles are most prevalent on the right imprint for the rod(Figure 5.22a), while the left imprint for the L-shape reinforcement contains the majority of air bubbles(Figure 5.22b). Tiny air bubbles are observed upon closer examination of the concrete impressions. Tiny air bubbles are evenly distributed on both sides of the imprint for the rod and L-shaped reinforcement.

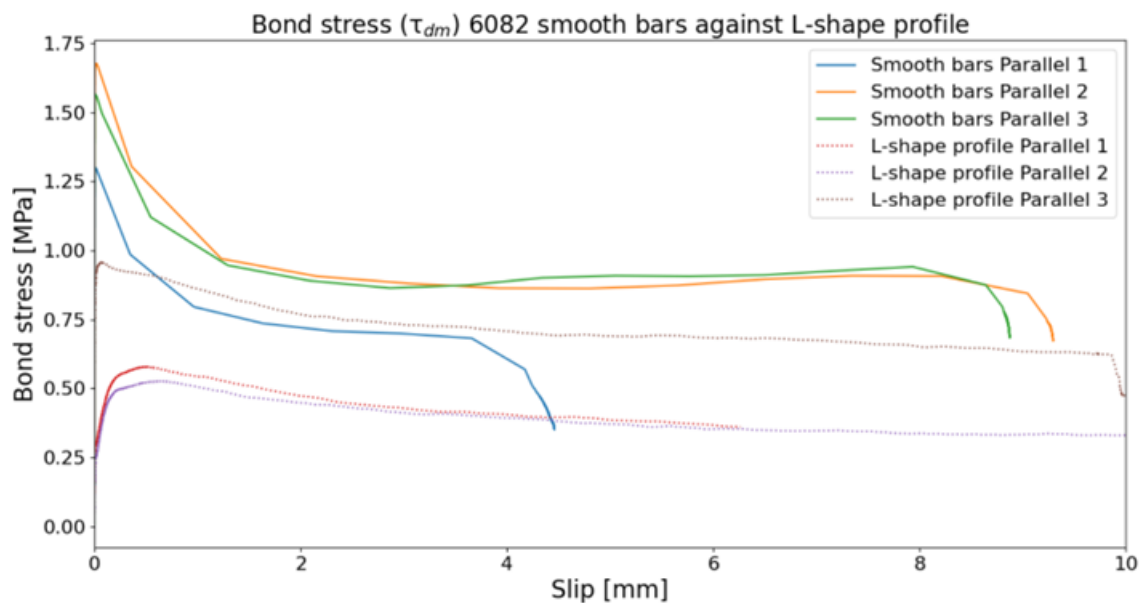


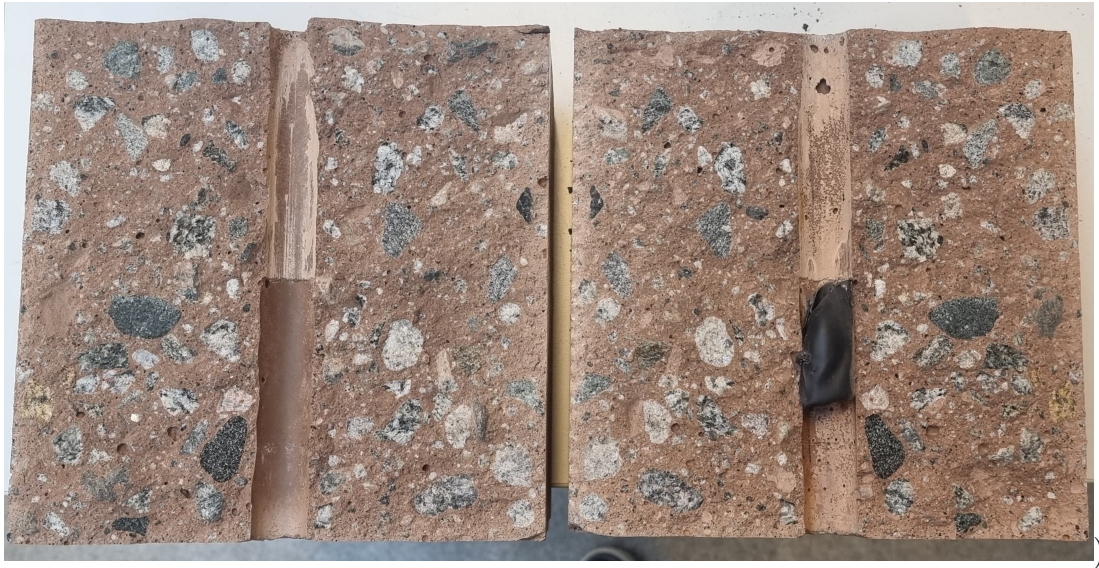
Figure 5.20: Bond stress (τ_{dm}) development comparison between smooth bars and L-shape profiles.



(a) 6082 bar after pull-out and corresponding cement imprint



(b) L-shape bar and corresponding cement imprint



(a) Cement imprint for bar reinforcement



(b) Cement imprint for L-shape reinforcement

Figure 5.22: Cement imprint for bar and L-shape reinforcement.

Table 5.15: Splitting bond stress (τ_{cr}) [MPa] for each sample.

Sample	Splitting bond stress (τ_{cr}) [MPa]
6082, smooth bars, Parallel 1	1.299
6082, smooth bars, Parallel 2	1.677
6082, smooth bars, Parallel 3	1.566
Stainless steel, smooth bars, Parallel 1	0.3154
Stainless steel, smooth bars, Parallel 2	0.298
Stainless steel, smooth bars, Parallel 3	0.981
6082, L-shape profile, Parallel 1	0.578
6082, L-shape profile, Parallel 2	0.526
6082, L-shape profile, Parallel 3	0.957

6 Discussion

6.1 Corrosion preventing qualities for generated environmentally friendly concrete constructions

This section discusses the potential for using hyaloclastite and ICEM in environmentally friendly concrete structures. The discussion is based on the GC results in Section 4.2 and will consequently be based on the chemical corrosion inhibiting potential of the concrete constructions.

6.1.1 Potential of hyaloclastite as SCM

Figures 6.1, 5.2 and Table 6.1 show the H_2 -emissions of hyaloclastite and CC in the GC experiments and the corresponding chemical composition. The GC measurements for the CC in Figure 6.1 are taken from previous work by the author. Figure 6.1 shows that the graph of hyaloclastite has a higher degree of noise than the graphs of the CC. The reasons for the high noise of hyaloclastite are probably due to different GCs were used to carry out the H_2 -measurements, and the sensitivity of the two GCs is different. Nevertheless, the remaining parameters of the stationary setup are identical. It would thus be reasonable to compare the stationary hyaloclastite measurements with stationary measurements from the CC.

From the two figures, two major observations can be made. First, as the first H_2 -emission is detected earlier for hyaloclastite, the corrosion reaction commences at an earlier stage when hyaloclastite is used. Second, an equal or slightly lower final H_2 -emission suggests that hyaloclastite is a corrosion-inhibiting material that is equal to or slightly superior to CC.

The observation of an earlier first H_2 -emission for hyaloclastite can be traced back to the specific surface of the materials. Table 4.5 reveals that CC particles' specific surface area is larger than that of hyaloclastite glass particles. As a result, the CC will have a greater propensity to react with $Ca(OH)_2$, hence delaying the corrosion response and first registered H_2 -emission^[9].

Examining the compositions of the SCMs can provide a chemical explanation for the slightly better or equivalent H_2 -emission of hyaloclastite compared to CC. The concentration of alumina and silica in hyaloclastite is shown in Table 6.1. The Al_2O_3 and SiO_2 concentration of hyaloclastite is slightly less than that of CC but is of the same magnitude. As described in Subsection 3.6.3 and illustrated by Reactions 3.27 and 3.28, Al_2O_3 and SiO_2 bind calcium hydroxide ($Ca(OH)_2$) to calcium aluminium hydrates ($Ca_3Al_2O_6 \cdot 6H_2O$) and calcium silica hydrates ($CaSiO_3 \cdot H_2O$), which will lower the pH and passivate the aluminium reinforcement. As a result, hyaloclastite will be able to passivate the reinforcement and minimise corrosion to a similar degree as CC.

In addition, the oxide composition of hyaloclastite includes alkalis (K_2O and Na_2O) that are nearly halved in comparison to the compositions of CC. This

results in a less alkaline environment, which aids in the passivation of the reinforcement.

However, because hyaloclastite has a lower Al_2O_3 content, fewer chlorides will react to the creation of Friedel's salt, as described in Section 3.6.6. Since Friedel's salt is more stable and binds more water, resulting in less porosity and increased strength, lower Al_2O_3 values in hyaloclastite can impact the longevity and strength of the concrete construction.

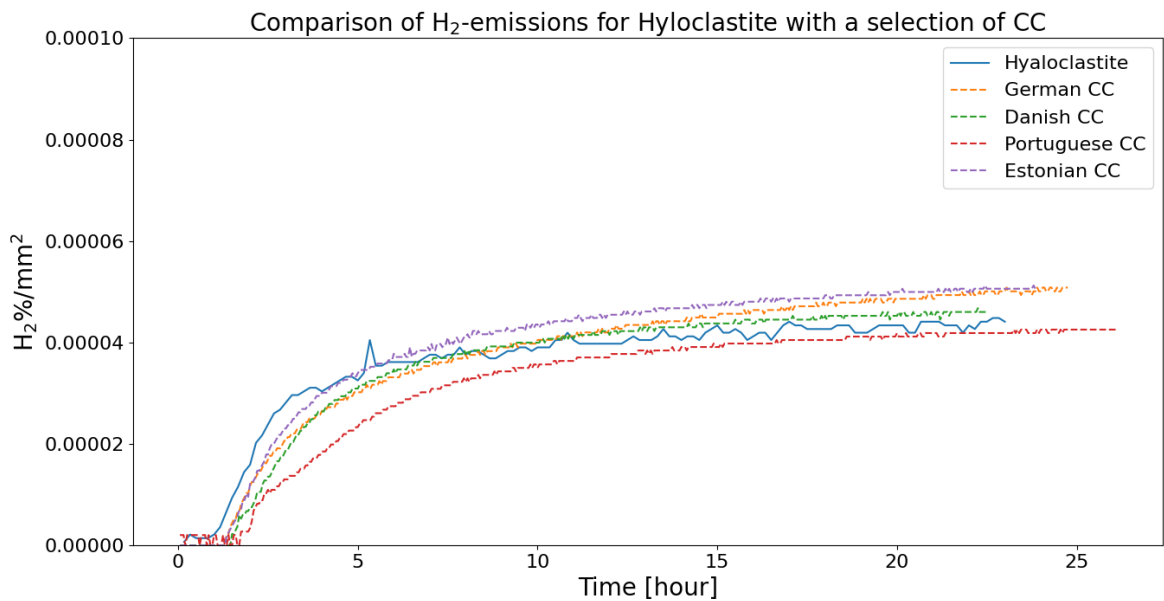


Figure 6.1: H_2 -emissions for hyaloclastite compared with other SCMs in the form of CC from Germany, Denmark, Portugal and Estonia. Data from the CC are taken from previous work by the author.

Table 6.1: The oxide composition of alumina(Al_2O_3) and silica(SiO_2), as well as the alkalis K_2O and Na_2O , for hyaloclastite and estonian CC.

Oxides	Hyaloclastite [wt%]	Estonian CC [wt%]
SiO_2	47.80	62.57
Al_2O_3	14.37	26.54
K_2O	0.31	3.77
Na_2O	1.82	0.08

In summary, the results found very promising chemical properties for using hyaloclastite as SCM in concrete structure with added CaCl_2 . Nevertheless, a lower Al_2O_3 content compared to CC could influence the mechanical properties of hyaloclastite supplied concrete construction. Therefore, to map the full potential, further work should look at the mechanical properties of hyaloclastite concrete structures.

6.1.2 Potential of utilising ICEM in newly created cement constructions

The concentrations of alumina(Al_2O_3) and silica(SiO_2) in CCEM and ICEM are in the same order of magnitude, as shown in Tables ?? and ?. The tables read that CCEM has a slightly higher SiO_2 concentration than ICEM, whereas ICEM has slightly higher Al_2O_3 concentrations. Based on Al_2O_3 and SiO_2 concentration, construction and ICEM are anticipated to have comparable H_2 -emissions and equally inhibitive impact.

However, Figure 5.4 and Table 5.2 show that CCEM emits less H_2 than ICEM. This discrepancy in H_2 -emissions can be traced back to the alkali content of the various types of cement. From Tables ?? and ??, it is determined that ICEM has twice the alkalinity of CCEM. Consequently, the quantity of OH^- in ICEM will be doubled, which increases the likelihood of corrosion, as stated by Reaction 3.24.

The difference in alkali, Al_2O_3 and SiO_2 for the to cements will further explain the delay in first detected H_2 -emission for the CCEM, shown in Figure 5.4. Due to a higher concentration of Al_2O_3 and SiO_2 in CCEM, will the cement be able to react with the newly generated $\text{Ca}(\text{OH})_2(\text{aq})$ during the *Acceleration phase*, preventing the formation of corrosion. As $\text{Ca}(\text{OH})_2$ is created evenly during the *Acceleration phase*, the $\text{Ca}(\text{OH})_2$ concentration will eventually predominate and initiate the corrosion process and subsequent H_2 production.

In the case of ICEM, however, Figure 5.4 and Table 5.2 show the first H_2 -emission register nearly immediately after the experiment has begun. This indicates that the paste's CaCl_2 , Al_2O_3 , and SiO_2 concentrations are insufficient to displace and suppress the $\text{Ca}(\text{OH})_2$ and corrosion response to the same degree.

Based on the preceding discussion, an increase in added CaCl_2 will be suggested for ICEM. Nonetheless, several experiments must be conducted to determine if the H_2 -emission levels may be reduced even more or if a treshold has been reached. In addition, as the dissolution of CaCl_2 is an exothermic reaction, it will be necessary to allow the water to cool down after adding the salt^[66], since the heat generated by the reaction will impede the anti-corrosion properties by accelerating the breakdown rate.

Table 6.2: The table shows the calculated corroded aluminum [mg], corroded aluminum per area [g/m^2] and mass loss [%] for samples used in the Flow system setup.

Sample	Corroded aluminium[mg]	Corrodet aluminium per area [g/m^2]	Weight loss[%]
ICEM,CaCl ₂ , 6082	13,372	9.472	1.579
ICEM, 6082	37.463	25.923	4.309
ICEM, CaCl ₂ , 4xxxA	1.960	1.414	0.236
ICEM, 4xxxA	25.797	33.082	2.988
CC, CaCl ₂ ,6082	4.774	3.371	0.561
Hyaloclastite, CaCl ₂ , 6082	3.509	2.435	0.405
(Estonian,CaCl ₂ 6082)	3.699	2.654	0.443
NaOH(pH=11.5),6082	1.138	0.815	0.0477
NaSi(pH=11.5),6082	0	0	0

Table 6.3: The table shows the calculated corroded aluminum [mg], corroded aluminum per area [g/m²] and mass loss [%] for samples used in the Stationary setup.

Sample	Corroded aluminium[mg]	Corroded aluminium per area [g/m ²]	Weight loss[%]
Hyaloclastite, CaCl ₂ , 6082	1.928	1.394	0.233
Estonian clay, CaCl ₂ , 6082	1.897	1.346	0.224

6.2 Comparing the Stationary and Flow system setup

This section discusses the quality of the registered H₂-emissions for the Stationary and new Flow system setup. The discussion will first discuss the calibration for the new setup before the standard deviation and noise levels for the two setups are presented. The standard deviations and the noise level are based on identical samples that use hyaloclastite as SCM. A similar analysis for estonian CC is presented in the Appendix C.3. Finally, the causes of noise for the setups are discussed.

6.2.1 Flow system calibration

Table 6.4 compares the gas concentrations in the air with and without an external pump, where the experiments were sampled every 3 minutes for 1 hour. The results show that the GC reports marginally higher concentrations when using a pump than measurements without a pump. The observation may be due to a higher pressure when using an external pump, which involves several molecules of each gas. Nevertheless, the increase when using a pump is in the order of one per mille, which corresponds to the size of the standard deviation in the measurements. It is therefore prudent to use the same calibration method for both setups.

A further observation is that using an external pump leads to the reporting of slightly higher O₂ and N₂ concentrations than expected in the atmosphere (Table 6.4). Further observations show that this method leads to a total concentration > 100 %. It will thus be appropriate to use normalized concentrations in the reporting.

Table 6.4: Comparison of the gas concentration of O₂, N₂, CO₂ and the total concentration for system with and without an external pump

System	O ₂ (%)	N ₂ (%)	CO ₂ (%)	Total(%)
Stationary system (without pump)	21.404 ± 0.036	79.358 ± 0.138	0.042 ± 0.001	100.804 ± 0.164
Flow system (with pump)	21.435 ± 0.023	79.459 ± 0.083	0.042 ± 0.000	100.936 ± 0.093

6.2.2 Standard deviation and noise level of the two setups

Figure 6.2 shows the H₂-development overtime to the two setups using hyaloclastite as SCM. The Figure shows that the Flow system has a earlier first registered H₂-emission and constantly higher reported concentrations compared to the measurements from the Stationary system. Furthermore, it is observed that

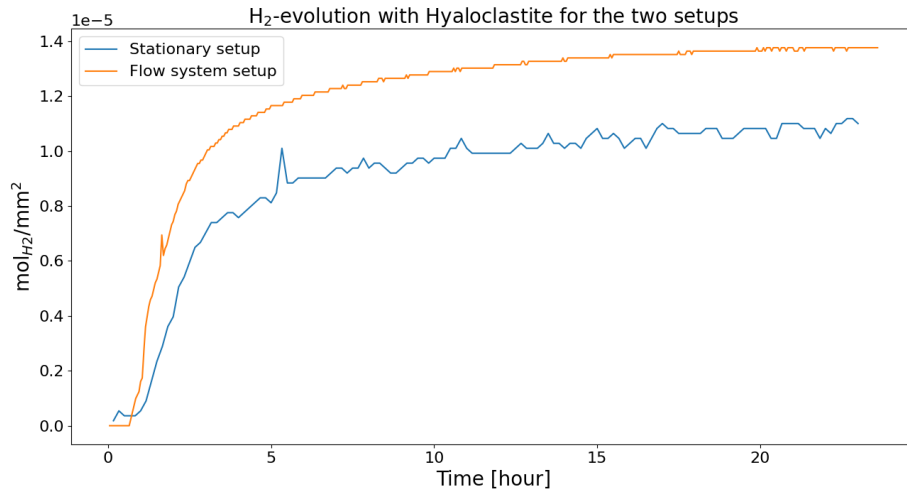


Figure 6.2: Comparing H_2 -development per area ($\frac{mol[H_2]}{mm^2}$) over time [hour] for the Stationary and Flow system setup when using hyaloclastite as SCM. mol_{H_2} is used due to different volumes for the setups.

the Stationary system has a greater degree of noise and variation in the measurements than the Flow system by having significant concentration differences between two subsequent measurements.

In order to be able to determine the standard deviations and the noise level of the reported H_2 -emissions for the Stationary and Flow system setups, respectively, the H_2 -emission curves were normalized. The normalisation was carried out on a graph where each measurement (y_n) was plotted against the next measurement (y_{n+1}), shown in Figure 6.3. Figure 6.3 shows a more extensive linear relationship for the Flow system setup measurements compared to the stationary setup.

By performing linear regression, the deviations from the linear regression will give the noise level to the original H_2 -emission curves. Upon further calculation of the standard deviation, values of the noise level curves are calculated and listed in Table 6.5.

The table show that the Stationary setup has a higher standard deviation and noise level than the Flow system, which decreases the noise level by a factor of 2.43

Table 6.5: Standard deviation (σ) for the two setups using hyaloclastite as SCM.

System	Standard deviation [$\sigma \cdot 10^{-8}$]
Hyaloclastite, Stationary setup	12.06
Hyaloclastite, Flow system setup	4.96

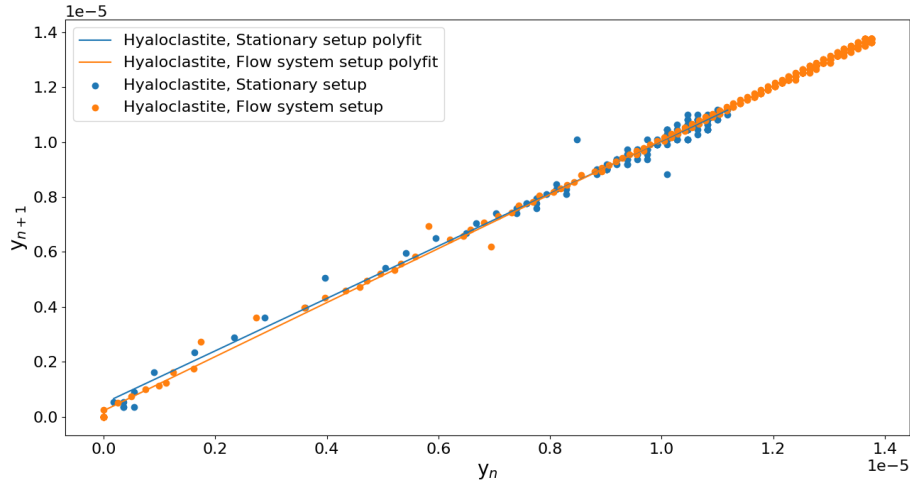


Figure 6.3: Normalising of the two setups

6.2.3 Registration of H_2 for the setups

Comparing the H_2 -emission curves of the Stationary and Flow system setup, shown in Figures 6.2, should be done with caution since changing the setup involves adjusting several parameters. When changing the setup, both the volume and the pressure are changed, affecting different parameters such as temperature. It will thus be most appropriate to study the development of reported H_2 -emissions from the GC for each setup individually.

As mentioned in the results Section 5.1.1, the Stationary setup indicates a more remarkable noise development than the Flow system setup. Noise occurs with strong individual effects in H_2 -concentration emissions between two subsequent measurements, either increasing or decreasing registered H_2 . An explanation for noise causing an increase in concentration between two subsequent registrations is based on how the H_2 -gas is emitted in the form of H_2 bubbles. As described in Reaction 3.24, H_2 is produced as a bi-product of the corrosion reaction on the surface of the aluminium reinforcement, which is set in concrete. Formation of tiny gas bubbles of H_2 at the reinforcement concrete interface, that further rises to the surface and accumulate before cracking, will lead to an unexpected increase in H_2 concentration, which will affect the graph. The formation of such small gas bubbles was found by carving the concrete cube for the pull-out test samples, as shown in Figure 5.22a, which used the same concrete composition as in the GC measurements.

Another explanation for noise in the form of an increase in concentration for the Stationary system is based on the registration of H_2 bubbles. The H_2 molecule is the lightest molecule, and H_2 bubbles will consequently accumulate in the upper part of the desiccator. Consequently, the concentration reporting of H_2 , which sucks in air from the upper part of the desiccator, will be higher than the average concentration. Unlike the Stationary setup, where H_2 gas dispersion

is dependent on normal diffusion, the Flow system setup will avoid increased H_2 -emissions from H_2 bubbles due to the airflow created by the external pump before each measurement.

Further reactions of the H_2 -molecule can explain noise in case of individual decreases in concentration. A decrease in H_2 concentration will not be possible in an ideal setup, since this indicates that H_2 disappears. One possible explanation may be leakage, but since this causes a constant decrease in H_2 -concentration, the figures shows that this is not a possible cause.

On the other hand, further reactions of the H_2 molecule will lead to a decrease in concentration measurements. H_2 molecules may be subjected to phase transitions and condensation formation in the column or desiccators. The formation of negative pressure in the Stationary setup due to extraction during sampling can accelerate the condensation reaction. Negative pressure will not be as widespread in the Flow system setup since air from the gas bag evens out the pressure differences during sampling. Consequently, condensation will not be as prevalent in the system. On the other hand, the fact that the Flow system is more extensive and has a larger surface area will increase the likelihood of condensation forming. Figure 6.4 shows a picture taken after the experiment, which show clear signs of condensation.

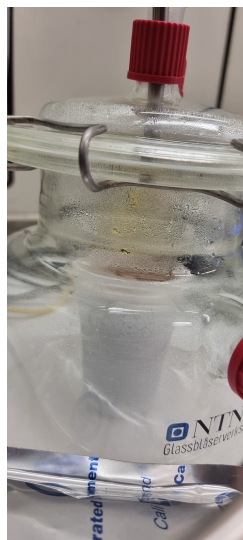


Figure 6.4: Image of observed condensation in the desiccator during and after the experiment.

A further point that is important to be aware of is that the most significant decreases in reported H_2 -concentration correspond to values that approach the sensitivity of the GC. The sensitivity of the GC depends on the thermal conductivity of the components in relation to the thermal conductivity of the carrier gas, which for H_2 is argon (Ar). The sensitivity of H_2 in this GC is estimated to be around 5-10 ppm. The most prominent individual reductions in H_2 -concentration from the Stationary setup corresponded to a decrease of 20 ppm. Concentration changes which cause noise thus remain at the limit of what the GC can register,

and registration errors should thus not be neglected.

As mentioned in procedure 4.2.1, the Flow system setup has a sampling interval of 180 s, while the Stationary system samples every 600 seconds. Consequently, the Flow system will be able to detect changes in H_2 concentration with an accuracy factor of 3.33 over the Stationary system. Based on this, the use of the Flow system should be preferred. As mentioned above, the Flow system setup also refers to less noise (Table 6.5) than the Stationary setup, and the data will consequently also be more credible.

6.3 Analysis of the reinforcing-concrete interface

This section discusses the results of analysing the boundary between reinforcement and concrete. The section will first discuss the aluminiumoxide layer formed for samples without added $CaCl_2$ before differences between the 6082 and 4xxxA reinforcements are explained. Furthermore, the section will discuss the results of samples with added $CaCl_2$ and the formation of the hypothesised silicate layer. Observation of a higher Ca concentration with added $CaCl_2$ will be further discussed. Finally, errors in the analysis method will be discussed and how these affect the quality and credibility of the results.

6.3.1 Aluminium oxide layer for samples without $CaCl_2$

The EDS analysis reveals a significant increase in Al and O for $CaCl_2$ -free samples both in the surface and interface analysis, where a layer between the concrete and reinforcement is formed.

Oxidation of aluminium is also observed by stereo microscope as a change surface colour, as well as creation of a white corrosion product. The blackening process, mentioned in Section 3.5.2 may explain the deeper grey colour on the reinforcing surface of samples without $CaCl_2$ due to the additional oxidation of Al_2O_3 by H_2O . In addition the observed white product on the reinforcement surface could be the corrosion product Gibbsite($Al(OH)_3(s)$).

The stereo microscope finding is supported by EDS-analysis, indicating a more considerable amount of O on the surface of $CaCl_2$ -free samples. Therefore, the reinforcement's colour shift indicates more oxidation reactions in samples lacking $CaCl_2$.

Based on the results of SEM and EDS, it is difficult to identify the aluminium corrosion product precisely. In addition, the SEM and EDS examinations of the surface reveal considerable variations in composition and morphology between different sections of the reinforcement surface. Thus, it will be challenging to identify a common denominator that applies to the entire system.

Some of the SEM pictures obtained from the surface investigation reveal a striking similarity in morphology with the oxidation result illustrated in Figure 3.12.

Comparing Figure 5.6a SEM picture to Figure 3.12a, which depicts the aluminium corrosion product Boehmite, reveals significant morphological similarities. Furthermore, Figure 5.6b may show the aluminium corrosion product Gibbsite presented in Figures 3.12b. Nevertheless, these findings are qualitative and should therefore only be used to give an indication of which reactions and products have been formed^[67].

Using Table 5.11, the EDS analysis's at% indicates an O concentration nearly twice as high as Al. Based on these values, Boehmite AlOOH(s) would be a plausible contender. A second option is that it is binary alumina composed of an equal amount of Al_2O_3 and Gibbsite (Al(OH)_3). This oxide's brittleness can be attributed to the temperature at which the oxide was created. Since the corrosion process during cement hardening does not surpass 70°C , it is thermodynamically advantageous for Al_2O_3 to exist as a porous and brittle material. Furthermore, the fact that the oxide layer is likely to be composed of many alumina elements will result in a porous and brittle structure.

In addition to Al and O, the interface EDS analysis taken on the oxide layers identifies Ca, Si, Mn and Na.

Although the amount of identified bi-elements corresponds to wt% below 3, these elements can impact the oxide layer and leading to its brittleness.

The bi-elements in the aluminates can originate either from the cement paste or from the alloy itself.

Highly soluble aluminates from aluminium corrosion, such as $\text{Al(OH)}_2\text{O}^-$ (Reaction 3.24), may react with ions Ca^{2+} , Na^+ and Mn^{2+} in the cement pore solution, creating the brittle products and a multi-component layer. Identified elements such as Si may originate from the alloy itself. Due to various corrosion-induced disintegration, Si remains in the oxide layer after the alloy has corroded away, forming clusters of the component in the oxide layer, as depicted in Figure 5.14d.

6.3.2 Corrosion resistance of 6082 and 4xxxAl reinforcement

An interesting and unexpected result from the H_2 -emission measurements to GC is that the 4xxxAl alloy refer to lower H_2 -concentrations than the 6082 alloy. However, SEM and LM indicate more significant pitting formation for the 4xxxAl alloy.

Observations in LM indicate that 4xxxAl alloy corrode more than 6082 alloy, and seawater inhibits the corrosion process. Table 5.10 reveals that 4xxxAl reinforcements have a larger layer thickness, with higher derivation at the contact between reinforcement and concrete. Based on the theory stated in 3.5.1, this can be explained by the fact that the 4xxxAl alloy is less noble and more susceptible to corrosion due to a more significant amount of Cu (Table 4.3). This discovery is also shown in Figure 5.11, where the surface pictures of the 4xxxAl alloy reveal a more considerable prevalence of pits compared to the 6082 alloys. These pitting pits further explain the greater diversity in coating thickness seen on the 4xxxAl reinforcement.

The capacity of seawater ions to precipitate $\text{Ca}(\text{OH})_2$ and diminish the cement paste's alkalinity will explain why concrete structures that include seawater have thinner coatings. Justnes et al. demonstrated that Mg^{2+} -ions in seawater passivate cement paste by precipitating $\text{Mg}(\text{OH})_2$ hydroxide^[10].

Increased Si content in 4xxxAl alloy compared to 6082 can explain the lower detected H_2 -emission measurement for 4xxxAl alloy compared to 6082 alloys, given in Figure 5.3 and Table 5.2. Figure 5.14c shows the LM image taken of the cross-sectional interface of a 4xxxAl alloy. Grey clusters with similar morphology and size above and below the interface surface are identified to a higher extent for 4xxxAl sample, and gave a high Si concentration by EDS-analysis. A possible mechanism for the passage of the Si-clusters past the interface is that the Si-particles do not react as quickly during the decomposition of an aluminium layer and are therefore present in the created layer. Furthermore, as shown in Equation 3.28, the Si-clusters will reduce the corrosion mechanism, since SiO_2 will bind H_2O , and $\text{Ca}(\text{OH})_2$, from the pore water, and thus act as an inhibitor of the corrosion reaction. Observations from SEM and LM, given in Figure 5.14, have shown that the Si-clusters near the reinforcement surface occur to a much greater extent for 4xxxAl alloys and in situations where CaCl_2 is not added than in situations where 6082 reinforcement is used. As a result of the high Si concentration in 4xxxAl alloys, concrete structures reinforced with these materials are more resistant to corrosion than those reinforced with 6082.

Based on the contradicting results from SEM and LM against GC, the crucial question will be which of these results should be relied upon. The primary distinction between the results of the SEM and LM and the results of the GC is that the SEM and LM results are qualitative, whereas the GC results are quantitative. The results of SEM and LM are based solely on single images and measurements derived from LM research. As a result, the images merely illustrate the tendencies identified throughout the investigation, and additional ways of analysis are required to facilitate the findings. On the basis of this logic, it would be prudent to depend on the results of the GC measurements.

In contrast, the corrosion values predicted from GC measurements are quite low for both the 4xxxAl and 6082 alloys when CaCl_2 is added. Although the 4xxxAl alloy exhibits significantly lower values by a factor of 6.7, the corrosion quantities for both reinforcements are so minimal that they will not be noticeable in practice.

Finally, the crucial question will be what the corrosion inhibiting potential of 6082 and 4xxxAl as reinforcement materials are. According to the data in Table 6.2, both 6082 and 4xxxAl alloys exhibit minimal corrosion and weight loss values. Although there is currently no standard governing which corrosion processes in concrete structures are authorised, 6082 and 4xxxAl alloys with added CaCl_2 exhibit good inhibitory capabilities. Thus, both the 6082 and 4xxxAl alloys have good chemical characteristics for application as reinforcement.

6.3.3 Silica layer

This master's SEM and EDS studies could not identify the corrosion-inhibiting silicate layer between the reinforcement and the concrete interface, which were assumed in a CaCl_2 -added environment. Table 5.14 and the following EDS spectra provided in Appendix C.4.3, reveal low levels of Si. In addition, none of the SEM images reveals a coating on the surface of the reinforcement.

However, the fact that the pure silicate layer might be as thin as a mono layer makes it challenging to detect using SEM and EDS. Mono layers can exist in the size of 0.33 nm, placing them at the edge of what SEM can detect^[102]. On the other hand, dissolved silica ($\text{SiO}_2(\text{aq})$) will create a network of silicates in the first pure mono layer, resulting in a multi-component layer consisting of silicon and other oxides. Such multiple component layers will have a thickness that should be identifiable by EDS^[102]. Nevertheless, such a multi-component layer should include a higher Si concentration than that discovered in the interface analysis. Based on the Figure 5.17 and Table 5.14, one can thus not conclude that such a multi-component layer has been found.

Contrary to SEM and EDS observations, GC studies of reinforcements in NaSi-solution indicate the creation of a protective silica layer. In contrast to the NaOH solution, the NaSi solution emits no H_2 . Since both solutions had a pH=11.5, the results indicate that Si inhibits corrosion process. High amounts of dissolved Si from OPC and SCM will result in an anti-corrosion effect. In addition, the results validate the corrosion rate graph for sodium silicate ($\text{Na}_6\text{Si}_2\text{O}_7$) in Figure 3.14.

As a result, it is concluded that even though SEM and EDS did not find the silicate layer, will Figure 5.5 quantitative demonstrates the Si inhibitory effect on the reinforcement by creating a protective layer.

Uncertainties regarding the NaSi and NaOH GC measurements

An unexpected development experiment of 6082 reinforcement in NaOH solution shows the stabilisation of H_2 emissions. Since the solution has a pH = 11.5, the Pourbaix diagram in given in Appendix A.1 and Figure 3.14 shows that the aluminium reinforcement at this pH is in the active area, leading to uncontrolled corrosion and H_2 -emissions. One would thus expect the H_2 concentration to rise regularly throughout the experiment. The stabilization of H_2 emissions thus indicates that the development of corrosion has stopped. At first glance, a possible explanation for this development would be the formation of a protective corrosion coating on the reinforcement. Based on the Pourbaix diagram, this hypothesis will not be true since the reinforcement cannot form passive layers at this pH. The formation of a passive layer can thus only be explained by a change in pH. Based on the reasoning above, a possible explanation for stabilizing the H_2 evolution in the experiment of reinforcement in NaOH solution will thus be that the pH is lowered to a level where the reinforcement is passive. Since pH is defined by the concentration of H_3O^+ and the OH^- ion consumed in the corro-

sion process, an increase in H_3O^+ ions will reduce pH. Since the experiment uses a solution volume of 100 mL, the number of OH^- ions may be too low to keep the pH stable during corrosion reaction over time.

6.3.4 Samples with added CaCl_2

Samples with added CaCl_2 indicate lower H_2 -emission, lower corroded material and EDS registers a higher proportion of Ca on the reinforcement surface.

Table 6.2 lists the proportion of corroded material for each test and shows that added CaCl_2 significantly reduces the corrosion rate for both the 6082 and 4xxxAl alloy, as mentioned in Section 4.1.2. The formation of the silicate layer described above, as well as Ca^{2+} ability to precipitation of hydroxides, described in Section 3.6.6, will explain the change in corrosion product.

An obvious explanation for higher amount of Ca for reinforcement surfaces that have been cured in cement pastes with added CaCl_2 is that the Ca concentration originates from cement paste residues. As shown in Table 4.3, OPC refers to higher concentrations of CaO compared to the concentration in the reinforcement, where it is only found as a trace element. Furthermore, adding CaCl_2 to the cement paste will increase its Ca concentration. The hypothesis of increased Ca coming from the cement paste is supported by experimental observations from stereo microscope, SEM and EDS.

Lighter regions in SEM pictures contains larger amount of Ca, since Ca has a higher atomic number than Al, Si, O and C. Consequently light sample in Figures 5.9 and 5.10 will frequently be attributable to products from Ca which can be led back to concrete leftovers. The EDS analysis on surfaces cured in a CaCl_2 environment further showed that the Ca composition was higher in the areas with mountainous appearance and high topography differences. Based on the morphology and oxygen composition found in EDS, a credible hypothesis may be that these are the concrete residues observed in stereo microscopy.

Although stereo microscope analysis cannot verify the mechanisms, reactions and elements on the reinforcement surface, the observations will provide a good indication of the mechanisms that occur on the reinforcement-concrete interface. Crystalline $\text{Ca}(\text{OH})_2(\text{s})$, as stated in Section 3.6.6, is a probable explanation for the observed crystalline white compounds on the reinforcing surface of CaCl_2 samples. In contrast, at% from the EDS analysis performed on one of these crystals, as shown in Figure 5.9 and Table 5.4, reveals an O at% that is more than double the reported Ca at%. Since pure $\text{Ca}(\text{OH})_2$ would result in an O at% twice as high as Ca, the analysis demonstrates that other oxides are present. The same holds true for oxides such as Friedel's Salt ($\text{Ca}_3\text{Al}_2\text{O}_6 \cdot \text{CaCl}_2 \cdot 12\text{H}_2\text{O}$) and the precipitates from SiO_2 ($\text{CaSiO}_3 \cdot \text{H}_2\text{O}(\text{s})$) and Al_2O_3 ($\text{Ca}_3\text{Al}_2\text{O}_6 \cdot 6\text{H}_2\text{O}(\text{s})$), where at% denotes different compositional conditions than a pure precipitate. Thus, the concrete residues on the reinforcing surface will be a combination of the previously stated precipitates and unreacted OPC and SCM.

Regardless of the precise composition of the residual concrete, it is crucial to understand why the addition of CaCl_2 results in such a dramatic shift in adhesion to the reinforcement surface.

Using the reasoning for creating a protective silicate layer, a convincing explanation for the more exceptional adhesion of concrete residues to CaCl_2 -added reinforcing surfaces may be that chemical interactions via silicate lead to chemical adhesion improvement. The composition and gelatinous structure of the silicate layer make it thermodynamically favourable for SiO_2 and other oxides in OPC and SCM to bond to the silicate layer as opposed to the aluminium surface. As a result, the silicate layer will produce a multi-component layer on the surface of the reinforcement, which, under SEM and stereomicroscope, appears as concrete residues on the reinforcement surface. Thus, the adhesion of concrete residues on the surface of the reinforcement supports the formation of a silicate layer.

6.3.5 Errors from EDS-analysis

The most prominent sources of inaccuracy in EDS studies are the inability to detect H and the detection of very high quantities of C. Furthermore, the fact that EDS identifies the individual elements and not the molecular composition will make it challenging to map the precise composition for the interface of aluminium reinforcement.

EDS's inability to detect H or determine the detected area's molecular composition propagates on the results' quality. In the analysis, this will mean that it is impossible to know the exact aluminium oxide generated at the contact between the reinforcement and the concrete. As mentioned in Section 6.3.1, it is hard to tell whether $\text{Al}(\text{OOH})$ is the oxide product or if the oxide contains a 50:50 Al_2O_3 : $\text{Al}(\text{OH})_2$ composition.

A sources of error from the EDS analysis performed in the experiments is the concentration of carbon (C). Based on the tables for the reinforcement and cement composition (Tables 4.1 and 4.3), the EDS analyses show unexpectedly high values for C. This applies to the surface analyses (Tables 5.4-5.9), as well as the interface EDS analyses carried out on the created layer. The addition of the carbon coating during the preparation of the samples before SEM and EDS analysis can withdraw the high C concentration.

For the interface analysis, the solidification in epoxy will further result in additional amounts of C and chlorine (Cl) that were not present before the preparation of the samples. Epoxy has the chemical formula $\text{C}_{21}\text{H}_{25}\text{ClO}_5$ and will cause samples in contact with the compound to have an increased C and Cl concentration. Due to the brittle and porous structure of the oxide layer, epoxy will be absorbed into the coating. C is the lightest atom in this system and will have the darkest colour in SEM. Since the cracks in Figure 5.13d appear as black lines the SEM image it shows that epoxy is absorbed and drawn into the oxide layer along the cracks.

Additionally, uncertainty from the EDS analysis is the detection of elements not present in the concrete composition or reinforcement. One of these elements is fluorine (F). The presence of F might come from using freshwater in the production of concrete or from impurities in the cement and reinforcement manufacturing processes. Small concentrations of (58 $\mu\text{g/L}$) have been added to fresh water in Norway and may affect the EDS analysis^[113]. Furthermore, contaminants will originate from the flux in the melt of the rotary kiln, during cement production or come from impurities in the kiln during heat treatment of the reinforcements.

A further challenge of using EDS and SEM for cross-section samples encapsulated in epoxy is that the electron beam causes the epoxy to heat up, which negatively impacts the image quality of the SEM. Consequently, it will not be optimal to conduct EDS analyses at these magnifications. Further work should therefore use instruments like X-ray Raman spectroscopy to get more reliable and accurate results.

6.4 Mechanical bonding properties for concrete construction determined by pull-out test

This section discusses the bonding strength results from the pull-out tests. The tests for the bonding strength were carried out to map the ability of the new concrete structures to function as a unit.

The discussion begins by discussing the impact of the reinforcing material on bond strength by referring to the results from 6082 and the stainless steel smooth bars reinforcements. The impact of the geometry on bond strength is then discussed by comparing the results from 6082 smooth bars and L-shape profiles. Finally, the information found by analyzing the reinforcement imprints is discussed.

Although Figures 5.18 and 5.20 depict the entire evolution of the bond stress-slip curve, as illustrated in Section 3.7.1 the essential information from these curves will be the curve's vertex, which reflects the system's splitting bond stress (τ_{cr}). The τ_{cr} value will be the most relevant, indicating the maximum allowable stress for a concrete structure. In addition, the displacement value for τ_{cr} will be noteworthy since it indicates the structure's resistance to stress after creating cracks.

Table 6.6: The average bond stress (τ_{dm}) [MPa] at 0.05 mm slippage for \varnothing 20mm 6082 smooth bar, \varnothing 20mm stainless steel smooth bar, and L-shaped 6082 profile obtained from the pull-out test.

Specimen	Bond stress(τ_{dm})[MPa] at 0.05 mm slippage
20mm \varnothing 6082 smooth bar	1.488 \pm 0.162
20 mm \varnothing stainless steel smooth bar	0.266 \pm 0.007
L-shaped 6082 profile	0.472 \pm 0.009

6.4.1 Comparing bond strength of 6082 and stainless steel reinforcements

Figure 5.18 refers to higher bond stress values for 6082 smooth rods compared to stainless steel smooth rods. The high values of the 6082 rods thus imply that the first three phases of the bond stress - slip curve; *Non-slip phase*, *Slight-slip phase* and *Splitting phase* are more dominant for these parallels^[28]. Consequently, chemical adhesion and friction which are the mechanisms dominating in the three mentioned phases will be more prevalent for 6082 smooth rods.

Using the same reasoning as in Section 6.3.4, the silicate layer's production will enhance the concrete's adherence to the reinforcing surface. This will result in elevated bond stress values following reinforcement pullout. The enhanced adhesion of the 6082 bar is also seen in Figure 5.19, where a more significant proportion of concrete adheres to the reinforcing surface of the 6082 reinforcement compared to stainless steel.

The mechanical enhancements of the 6082 reinforcement may be the result of a rougher surface. From the interface cross-sectional examination, LM and SEM pictures reveal an interface surface with minor topographical changes, resulting in a more uneven reinforcement surface. In pull-out tests, the roughness will increase resistance and friction, leading to a more significant bond stress. Unlike the 6082 reinforcement, the stainless steel reinforcement will not undergo chemical reactions at the interface between the reinforcement and the concrete, as depicted in Figure 5.19b. As a result, the bonding stress to the steel reinforcement will be less than that of 6082 reinforcement.

Furthermore, Figure 5.18 shows higher values for the 6082 reinforcement in the *Decreasing* and *Residual phases*. Higher values in the *Residual phase* imply a more significant collapse between concrete and reinforcement. Since the concrete composition is equal in all parallels, the more widespread collapse will be due to a higher load being added when the system collapses. Higher values in the *Residual phase* for the 6082 reinforcement are due to higher friction values when pulled out after the reinforcement has been completely torn from the concrete. In addition, Figure 5.18 demonstrates a more gradual transition between the *Decreasing* and *Residual phases* for stainless steel profiles. Since friction is the only mechanism responsible for bond stress in these phases, the figure illustrates that friction accounts for a more significant proportion of bond stress in stainless steel than in 6082 bars.

The pull-out tests for *Stainless steel Parallel 3* produced unexpectedly high bond stress values compared to the other two parallels, which differ by a factor of 3.2. Based on the theory, the dissociation described above, and the inspections conducted after the pull-out test, one would anticipate that *Stainless steel Parallel 3* bond stress values would be comparable to those of the other parallels. The sample of *sStainless steel Parallel 3* was collected four days after the other two samples, which may account for its high bond stress value. Consequently, the

curing period of the cement, adhesion, and friction between the reinforcement and concrete would be enhanced for this parallel. However, the effect of the longer curing time will not be sufficient to account for such a substantial change. Therefore, the discrepancy must be attributable to experimental error, and additional pull-out tests should be conducted to comprehend the system's potential better.

Based on the discussion and results comparing smooth bars for 6082 and stainless steel reinforcements, silicate layers and minor corrosion formation result in more adhesion and friction between reinforcement and concrete for 6082, increasing the mechanical bond strength. As a result, 6082 will be more suited for concrete construction.

By comparing the results with the values given in Table 3.2, where the results are compared with concrete class > 40 for smooth bars in tension, the results are within the expected range. In light of the pull-out tests, the 6082 smooth bar has therefore high application potential in concrete constructions.

6.4.2 Comparing bond stress of bars and L-shape profiles for 6082 reinforcements

Given that both the bars and the L-shaped profiles are 6082 reinforcements that have been heat-treated using the same process and put in the same concrete composition, one would anticipate that the bond stress values of the two reinforcements would be identical. This is because bond stress (N/mm^2) is anti proportional to the profiles area (mm^2).

However, considerable differences are detected between the two profiles regarding τ_{cr} and its location. The τ_{cr} of the L-shape is located to the right of the smooth bars. This suggests that the *Slight slip phase* (phase 2) is more prevalent in L-shaped structures, which is dominated by relative slippage prior to the collapse of the concrete.

Different geometries for the smooth bars and L-shape profiles can explain the difference in bond stress and bond stress-slip curve development for the two reinforcements. Since the smooth bar is symmetric, will the circumferential adhesion be uniform when the bar is pulled out. This will lead to a high equal collapse, which results in high bond stress before a significant decrease occurs, as shown in the figure. In contrast, the L-shape profile will likely have variable adhesion around its perimeter. Consequently, the adhesion will collapse at different times for different areas on the profile. Hence the adhesion collapse happens gradually, which results in a lower τ_{cr} and offset to the right of the diagram.

Large air bubbles at the interface of the reinforcement and concrete in the L-shaped profile can further explain the lower bond stress values. As observed in the result in Figure 5.22b, large air bubbles are identified in the concrete imprint of the L-shape reinforcement. These air bubbles reduce the contact surface between the reinforcement and the concrete and minimise the system's ability to form adhesion and friction between the components. As shown in

Equation 3.32, bond stress depends on the contact area. The area used in the calculation is based on the total area of the reinforcement, and the calculated bond stress will consequently give a lower value than in reality.

Figure 5.20, similar to Figure 5.18, depicts a more dominating *Decreasing phase* for the smooth bars than for the L-shaped profile, indicating that the adhesion forces and concrete collapse are larger for constructions that employ bars. Furthermore, the L-shape profiles shows a more gradual transition between the *Decreasing* and *Residual phase* as well as a lower bond stress value in the *Residual phase* (horizontal line). As discussed in Section 6.4.1, this implies that friction constituted to more of the bond stress for L-shape profiles, but that the total friction force is larger for smooth bars.

Friction between the reinforcement and the holding plate will increase the detected bond stress for individual parallels. Figure 5.20 depicts that *L-shape parallel 3* has higher bond stress values than the other two parallels by a factor of 1.73. Contact between the reinforcement and the holding plate during this individual pull-out test could have increased friction and, consequently, the bonding stress value.

In conclusion, the results and discussion indicate that, due to their geometry, smooth bars have a higher binding strength than L-shaped bars. The smooth bars' adherence is increased uniformly due to the uniform adhesion. In addition, the uniform geometry prevents the collection of air bubbles at the interface between the reinforcing and the concrete, preventing a reduction in bond strength by lowering adhesion and friction between the reinforcement and the concrete.

6.4.3 Analysis of reinforcement imprints

Analysis of the reinforcing imprint provides further information regarding the mechanical and chemical processes occurring prior to and during pull-out testing.

The observed colour change mentioned Section 5.4.2 might be achieved chemically or mechanically by forming new component coatings or friction at the reinforcement interface.

Chemical reactions at the interface that result in the production of new components might cause a colour change in the concrete. As stated in Subsection 5.4.2, the concrete's colour change occurs in areas where the concrete is in direct contact with the reinforcement. Since the hypnotised silicalayer only will be created through direct contact between the reinforcement and the concrete, Figures 5.21a and 5.22a indicate that the colour change results from chemical reactions.

Changes in the colour of concrete caused by friction is an explanation of the colour difference between areas of concrete in touch with reinforcement and those that have not. The surface roughness of the reinforcement will increase friction during pull-out for areas in direct contact with the concrete, leading to colour change. In addition, the discrepancies in colour between the right and left impressions in

Figure 5.22a can be explained by the application of friction, as the reinforcement was not drawn out entirely vertically. In the event of uneven extraction, the friction will be more substantial on one side of the concrete cube, resulting in a more pronounced colour change. The light brown colour at the bottom left of the imprint in Figure 5.22a could be further explained by the imprint's friction-induced colour change. As the colour shift occurs at the surface where the reinforcement was extracted, the friction will be particularly high in this area, causing a colour change in the imprint.

As for altering the colour of the concrete, the air bubbles noticed in the concrete imprints in Figure 5.22 can be explained chemically. By corroding the reinforcement, the creation of H_2 -gas as tiny air bubbles can be released into the concrete imprint. The fact that the tiny air bubbles are evenly distributed in regions of the concrete structure that were in direct contact with the reinforcement lends credence to the theory that the air bubbles result from a corrosion response.

In contrast, the most plausible explanation for the large air bubbles is that they persisted after the cement paste was stirred. Since large air bubbles can be visible in portions of the impression that were in direct contact with the reinforcement as well as places that were not (Figure 5.21a), these air bubbles cannot be a result of the corrosion process. The size and irregular distribution of the air bubbles provide more evidence that these air bubbles are not chemically produced. Figure 5.22b demonstrates that the large air bubbles are more common on the left side of the imprint of the L-shaped reinforcement. This is due to the cement block's position during curing, as shown in Figures 4.12b and 4.12c. Large air bubbles generated by stirring the cement will not be able to diffuse out of the cement during the curing process when they interact with the horizontal reinforcing surface, causing them to accumulate at the interface. In contrast, the geometry of the reinforcing bar will permit more air bubbles to diffuse past it. This explains why the rod impression does not contain as many large air bubbles.

Based on these results, it is recommended for further work to harden the concrete structures with the reinforcements vertical to avoid an unnecessary accumulation of air bubbles at the reinforcement-concrete interface.

7 Conclusion

This master's thesis examined the potential of utilising an environment-friendly concrete structure in which 55% of the cement has been replaced with SCM, and CaCl_2 has been added for concrete construction that use 6082 or 4xxxA reinforcement. The potential of the environmentally friendly concrete construction was examined by determining the chemical corrosion resistance, assessing the interface between the reinforcement and the concrete, and study the mechanical bonding qualities of the concrete construction.

H_2 -emissions detected by GC demonstrated excellent corrosion resistance with the addition of CaCl_2 and a high potential for hyaloclastite to be utilised as SCM. Furthermore use of ICEM showed promising properties in the new environment friendly concrete constructions.

Adding CaCl_2 to the cement paste decreased H_2 -emission by 2.74 for the 6082 and 12.7 for the 4xxxA reinforcement. The GC measurements revealed that the inhibitory corrosion potential of hyaloclastite was comparable to or slightly superior to that of CC. The good properties of hyaloclastite were justified by a corresponding alumina and silica concentration and a halved alkali concentration for hyaloclastite compared to CC. The reduced alumina concentration of hyaloclastite, on the other hand, can cause a smaller amount of Friedel's salt to develop, resulting in a concrete construction that is less mechanically stable.

Compared to CCEM, ICEM resulted in more H_2 -emission and corrosion development, which was explained by the higher alkali concentration. For future studies, it is advised to increase the amount of CaCl_2 added to the cement paste to determine if corrosion can be decreased further or if a threshold has been reached. However, adding CaCl_2 to ICEM shows promise for future research and use.

Creating a new GC Flow system resulted in evenly detected samples that lowered the H_2 -detection noise level by a factor of 2.43. The subsequent lowering of the detection period from 600s to 180s resulted in a GC setup that more precisely identified changes in H_2 -concentrations. As a result, the values will be more credible, and the Flow system will be recommended for further experiments.

CaCl_2 prevented the formation of a brittle oxide layer at the surface and cross-sectional interface between the reinforcement and the concrete. Although the exact composition of the oxide layer could not be identified, the brittleness and at% detected by EDS indicate that the samples consisted of several alumina oxides. The LM, SEM, and EDS result also found a more significant proportion of Si clusters in the oxide layer of the 4xxxA reinforcement compared to the 6082 reinforcement. The corrosion-inhibiting capabilities of SiO_2 can explain why 4xxxA has superior corrosion resistance versus 6082.

Although EDS did not detect the expected protective silicate layer, GC H_2 -measurements for 6082 in a NaSi solution with $\text{pH} = 11.5$ demonstrated the creation of the Si layer indirectly. Moreover, the improved concrete adhesion to reinforcement in CaCl_2 -added cement paste showed the production of a silicate layer, as the gel-like structure of the silicate layer makes it thermodynamically

favourable for oxides in the cement paste to adsorb to the reinforcement.

The preparation of the samples and the use of EDS in the analysis contributed to sources of error in the study. Preparation with carbon coating prior to EDS examination resulted in significantly elevated C concentrations. In addition, because EDS is incapable of detecting H, it will be unable to differentiate between various aluminium oxides in the oxide layer. For a better determination of the products at the interface layer, it is recommended that Raman X-rays spectroscopy be used.

The mechanical bond strength between reinforcement and concrete was greater for 6082 than for stainless steel for smooth bars and more significant for 6082 smooth bars than for L-shaped profiles.

The improved bond strength of 6082 smooth is related to a higher adherence of concrete to the reinforcement due to creating a silicate layer and increased friction due to minor pitting for the 6082 reinforcement.

The geometry of 6082 smooth bars resulted in a constant adhesion between the concrete and reinforcement, which increased the bond strength of the construction in comparison to the L-shaped profiles, which had variable adhesion. Additionally, the uniform geometry prevented the accumulation of air bubbles at the interface, which reduced the bond strength.

The influence of the bonding strength was also discovered by evaluating the reinforcing imprint, where a shift in colour at places of high bonding strength showed the impact on the concrete construction. It should be noted that the results are indicative since they are based on limited sample size.

In summary, it is concluded that environmentally friendly concrete construction using aluminium reinforcement refer to high chemical and mechanical potentials to replace traditional climate-challenging concrete construction.

8 Further Work

- Perform several GC and pull-out tests and parallels to get a better sample size.
- Map the potential of ICEM better by adding more significant amounts of CaCl_2 .
- Analyse the interface between reinforcement and concrete with X-ray Raman spectroscopy.
- Analyse silicate with X-ray Raman spectroscopy.
- Carry out pull-out test after thermal cycling.
- Perform pull-out test for concrete construction using 4xxxA, hylocastite and ICEM.

References

- [1] S. Jacobsen, *Concrete Technology*. Norwegian University of Science and Technology, Faculty of Engineering Science and Technology, Department of Structural Engineering, January 2016.
- [2] H. Klee, R. Hunziker, R. van der Meer, and R. Westaway, “Getting the numbers right: a database of energy performance and carbon dioxide emissions for the cement industry,” *Greenhouse Gas Measurement and Management*, vol. 1, no. 2, pp. 109–118, 2011.
- [3] *Low-Carbon Transition in the Cement Industry*. OECD, Apr. 2018.
- [4] H. Justnes, “Aluminium metal reinforced concrete-an environmental-friendly system with infinite service life.”
- [5] D. L. Chandler, “Researchers have created emissions-free cement.” <https://www.weforum.org/agenda/2019/09/cement-production-country-world-third-largest-emitter/>, 2019. Last accessed 16 October 2021.
- [6] “Cement technology roadmap plots path to cutting co2 emissions 24 by 2050 - news.” <https://www.iea.org/news/cement-technology-roadmap-plots-path-to-cutting-co2-emissions-24-by-2050>.
- [7] IEA, “Global cement production.” <https://www.iea.org/data-and-statistics/charts/global-cement-production-2010-2019>, 2010-2019. Last accessed 16 October 2021.
- [8] H. Justnes, *Performance of SCMs – Chemical and Physical Principles*. 2nd International Conference of Sustainable Building Materials, Technische Universiteit Eindhoven, 2019.

-
- [9] J. H., *Durability and sustainability implications of concrete reinforced with aluminium metal*. 07 2019.
- [10] H. Justnes, “Durable aluminum reinforced environmentally-friendly concrete construction – dare2c,” *Nordic Concrete Research*, vol. 56, p. 71, 07 2017.
- [11] M. S. Imbabi, C. Carrigan, and S. McKenna, “Trends and developments in green cement and concrete technology,” *International Journal of Sustainable Built Environment*, vol. 1, pp. 194–216, Dec. 2012.
- [12] C. R. Gagg, “Cement and concrete as an engineering material: An historic appraisal and case study analysis,” *Engineering Failure Analysis*, vol. 40, pp. 114–140, May 2014.
- [13] M. O. Bosoga, A. and Oakey, “Co2 capture technologies for cement industry,” *Energy Procedia*, vol. 1:1, pp. 133–140, 2009.
- [14] H. Justnes, “How to make concrete more sustainable,” *Journal of Advanced Concrete Technology*, vol. 13, pp. 147–154, Mar. 2015.
- [15] H. Justnes, *How to make concrete more sustainable*. 1st International Conference on Concrete Sustainability, 2013.
- [16] H. Justnes, *Kinetics of Reaction in Cementitious Pastes Containing Silica Fume as Studied by ^{29}Si MAS NMR*. Nuclear Magnetic Resonance Spectroscopy of Cement-based Materials (Eds. P. Colombet, A.-R. Grimmer, H. Zanni and P. Sozzani), Springer Verlag, Berlin, 1998.
- [17] B. Lothenbach, K. Scrivener, and R. D. Hooton, “Supplementary cementitious materials,” *Cement and Concrete Research*, vol. 41, pp. 1244–1256, 2011.
- [18] M. I. B. J. Justnes, H. and J. Krane, *A ^{29}Si MAS NMR Study of the Pozzolanic Activity of Condensed Silica Fume and the Hydration of Di- and Tricalcium Silicate*, ch. 111-116. Advances in Cement Research, 1990.
- [19] R. E. Richards, “Hyaloclastite pozzolan hyaloclastite based cement hyaloclastite based concrete and method of making and using same,” *Romeo Ilarian Ciuperca*, 2018.
- [20] M. T. Gudmundsson, F. Sigmundsson, and H. Björnsson, “Ice–volcano interaction of the 1996 gjálp subglacial eruption, vatnajökull, iceland,” *Nature*, vol. 389, pp. 954–957, Oct. 1997.
- [21] K. J., “Alternative reinforcement approaches – extended service life of exposed concrete structures,” *Chalmers University of Technology*, vol. Department of Civil and Environmental Engineering, p. 117, 2014.
- [22] H. Justnes, “A review of chloride binding in cementitious systems,” *Nordic Concrete Research*, vol. 1/98, no. 21, pp. 48–63, 1998.

- [23] J. Skibsted and R. Snellings, “Reactivity of supplementary cementitious materials (scms) in cement blends,” *Cement and Concrete Research*, vol. 124, p. 105799, 2019.
- [24] Norcem, “Norcem industrisement,” 2017. Last accessed 6. June 2022.
- [25] S.-H. Chao, A. Naaman, and G. Parra-Montesinos, “Local bond stress-slip models for reinforcing bars and prestressing strands in high-performance fiber-reinforced cement composites,” *American Concrete Institute, ACI Special Publication*, pp. 151–171, 01 2010.
- [26] A. H. Nilson, D. Darwin, and C. W. Dolan, *Design of Concrete Structures*. New York, NY: McGraw-Hill Professional, 15 ed., Jan. 2015.
- [27] J. Eiras-López, S. Seara-Paz, B. González-Fonteboa, and F. Martínez-Abella, “Bond behavior of recycled concrete: Analysis and prediction of bond stress–slip curve,” *Journal of Materials in Civil Engineering*, vol. 29, no. 10, p. 04017156, 2017.
- [28] C.-W. Tang and C.-K. Cheng, “Modeling local bond stress–slip relationships of reinforcing bars embedded in concrete with different strengths,” *Materials*, vol. 13, p. 3701, Aug. 2020.
- [29] C. R. Gagg, “Cement and concrete as an engineering material: An historic appraisal and case study analysis,” *Engineering Failure Analysis*, vol. 40, pp. 114–140, 2014.
- [30] I. Concrete, “The glue that holds concrete together.” https://medium.com/@Int_Concrete/asr-in-concrete-part-2-b131d661a02c.
- [31] J. F. D. D. Mindess, Sidney; Young, *Concrete Second Edition*. Prentice Hall, Pearson Education, Inc. Upper Saddle River, NJ 07458,U.S.A., 2003.
- [32] H. F. W. Taylor, *Cement Chemistry* -. London: Thomas Telford, 1997.
- [33] I. Richardson, “The calcium silicate hydrates,” *Cement and Concrete Research*, vol. 38, pp. 137–158, 02 2008.
- [34] A. J. Allen, J. J. Thomas, and H. M. Jennings, “Composition and density of nanoscale calcium–silicate–hydrate in cement,” *Nature Materials*, vol. 6, pp. 311–316, Mar. 2007.
- [35] L. G. Baquerizo, T. Matschei, K. L. Scrivener, M. Saeidpour, and L. Wadsö, “Hydration states of afm cement phases,” *Cement and Concrete Research*, vol. 73, pp. 143–157, 2015.
- [36] K. Nisancioglu and A. Erbe, *Corrosion Basics and Engineering*. Trondheim: NTNU, 1994.
- [37] K. B. Oldham, J. Myland, and A. Bond, *Electrochemical Science and Technology*. Hoboken, NJ: Wiley-Blackwell, Dec. 2011.

-
- [38] U. Nürnberger, “Korrosion der metalle im kontakt mit minerlischen baustoffen.” <https://citeseerx.ist.psu.edu/viewdoc/download?doi=10.1.1.1.492.8847&rep=rep1&type=pdf>.
- [39] C. Q. Li, J. J. Zheng, W. Lawanwisut, and R. E. Melchers, “Concrete delamination caused by steel reinforcement corrosion,” *Journal of Materials in Civil Engineering*, vol. 19, pp. 591–600, July 2007.
- [40] “Abundance in earth’s crust of the elements,” 2019. Last accessed 5 December 2020.
- [41] I. J. Polmear, I. Polmear, and V. Ravi, *Light alloys*. Woburn, MA: Butterworth-Heinemann, 4 ed., May 2014.
- [42] M. D. Sabatino, “knalegeringer.”
- [43] N. Christensen, “aluminiumlegeringer.”
- [44] T. Kobayashi, “Strength and fracture of aluminum alloys,” *Materials Science and Engineering: A*, vol. 280, no. 1, pp. 8–16, 2000.
- [45] S. Otarawanna and A. Dahle, “6 - casting of aluminium alloys,” in *Fundamentals of Aluminium Metallurgy* (R. Lumley, ed.), Woodhead Publishing Series in Metals and Surface Engineering, pp. 141–154, Woodhead Publishing, 2011.
- [46] R. Nadella, D. Eskin, Q. Du, and L. Katgerman, “Macroseggregation in direct-chill casting of aluminium alloys,” *Progress in Materials Science*, vol. 53, no. 3, pp. 421–480, 2008.
- [47] Y. Dewang, “A study on metal extrusion process,” vol. 2, 07 2018.
- [48] S. A. Rahim, M. Lajis, and S. Ariffin, “A review on recycling aluminum chips by hot extrusion process,” *Procedia CIRP*, vol. 26, pp. 761–766, 2015. 12th Global Conference on Sustainable Manufacturing – Emerging Potentials.
- [49] I. Runnigen, “Aluminum alloys as reinforcement in concrete constructions: Opportunities and challenges,” 2021.
- [50] A. Vasudevan and R. Doherty, *Aluminum Alloys—Contemporary Research and Applications: Contemporary Research and Applications*. ISSN, Elsevier Science, 2012.
- [51] C. Vargel, “Chapter a.3 - the metallurgy of aluminium,” in *Corrosion of Aluminium* (C. Vargel, ed.), pp. 23–57, Amsterdam: Elsevier, 2004.
- [52] M. Zamani, *Al-Si Cast Alloys - Microstructure and Mechanical Properties at Ambient and Elevated Temperature*. Jonkoping: Jonkoping University, School of Engineering, 2015.
- [53] B. Dybowski, B. Adamczyk-Cieslak, K. Rodak, I. Bednarczyk, A. Kielbus,

- and J. Mizera, “The microstructure of als7mg alloy in as cast condition,” *Solid State Phenomena*, vol. 229, pp. 3–10, 04 2015.
- [54] I. Kovačević, “Simulation of spheroidisation of elongated si-particle in al–si alloys by the phase-field model,” *Materials Science and Engineering: A*, vol. 496, no. 1, pp. 345–354, 2008.
- [55] G. Ran, J. Zhou, and Q. Wang, “Precipitates and tensile fracture mechanism in a sand cast a356 aluminum alloy,” *Journal of Materials Processing Technology*, vol. 207, no. 1, pp. 46–52, 2008.
- [56] J. A. Taylor, “The effect of iron in al-si casting alloys,” *Australian Foundry Institute National Conference*, vol. 35, pp. 148–157, 2004.
- [57] C. Ravi and C. Wolverton, “First-principles study of crystal structure and stability of al–mg–si–(cu) precipitates,” *Acta Materialia*, vol. 52, pp. 4213–4227, 08 2004.
- [58] D. Kim, J. Kim, S. Wenner, E. Thronsen, C. D. Marioara, R. Holmestad, and E. Kobayashi, “Precipitation behavior of al-si-cu-mg(-fe) alloys by a deformation-semisolid extrusion process,” *Materials Characterization*, vol. 173, p. 110863, Mar. 2021.
- [59] F. J. Tavitas-Medrano, A. M. A. Mohamed, J. E. Gruzleski, F. H. Samuel, and H. W. Doty, “Precipitation-hardening in cast AL–si–cu–mg alloys,” *Journal of Materials Science*, vol. 45, pp. 641–651, Feb. 2010.
- [60] J. R. Davis, ed., *Alloying*. ASM International, Oct. 2001.
- [61] G. K. Sigworth, “The modification of al-si casting alloys: Important practical and theoretical aspects,” *International Journal of Metalcasting*, vol. 2, pp. 19–40, Apr. 2008.
- [62] A. Beer, “8 - enhancing the extrudability of wrought magnesium alloys,” in *Advances in Wrought Magnesium Alloys* (C. Bettles and M. Barnett, eds.), Woodhead Publishing Series in Metals and Surface Engineering, pp. 304–322, Woodhead Publishing, 2012.
- [63] G. E. Totten and D. S. MacKenzie, eds., *Handbook of aluminum: Handbook of aluminum alloy production and materials manufacturing volume 2*. Boca Raton, FL: CRC Press, Apr. 2003.
- [64] W. D. Callister and D. G. Rethwisch, *Materials Science and Engineering*. Nashville, TN: John Wiley & Sons, 9 ed., May 2014.
- [65] A. Rollett, *Recrystallization and related annealing phenomena*. Elsevier, 3 ed., Apr. 2013.
- [66] A. Blackman, *Aylward and Findlay’s SI chemical data*. Milton, Qld: John Wiley & Sons Australia, 2014.
- [67] *Corrosion of Aluminium*. Elsevier, 2004.

-
- [68] R. Meyers, *Encyclopedia of physical science and technology*. San Diego: Academic Press, 2002.
- [69] J. H. Reimers, *Aluminium*. Oslo: Johan Grundt Tanum, 1947.
- [70] R. Ma, Q. Jiang, and J. Chen, “The superhydrophobic surface constructed with boehmite micro-nanostructure,” *Journal of Materials Science*, vol. 55, pp. 5795–5807, Feb. 2020.
- [71] C. Kautz and P. Ryan, “The 10 Å to 7 Å halloysite transition in a tropical soil sequence, costa rica,” *Clays and Clay Minerals - CLAYS CLAY MINER*, vol. 51, pp. 252–263, 06 2003.
- [72] S. MAHMOUD and M. Ahmed, “The inhibition effect of some pyrimidine derivatives on corrosion of aluminum and some of its alloys in 2.0 m hcl solutions,” *Al-Azhar Bulletin of Science*, vol. 18, pp. 133–149, 06 2007.
- [73] C. Y. Chao, L. F. Lin, and D. D. Macdonald, “A point defect model for anodic passive films: I. film growth kinetics,” *Journal of The Electrochemical Society*, vol. 128, pp. 1187–1194, June 1981.
- [74] A. Sehgal, D. Lu, and G. S. Frankel, “Pitting in aluminum thin films: Supersaturation and effects of dichromate ions,” *Journal of The Electrochemical Society*, vol. 145, pp. 2834–2840, aug 1998.
- [75] Z. Szklarska-Smialowska, “Pitting corrosion of aluminum,” *Corrosion Science*, vol. 41, no. 9, pp. 1743–1767, 1999.
- [76] R. Johnsen, “Corrosion challenges with the use of aluminium in offshore and marine environments.” https://www.bluemaritimecluster.no/download?objectPath=/upload_images/CA6A704C6D3F4F2196B367FC79E66DCE.pdf, 2019. Accessed: 2022-15-05.
- [77] M. C. Juenger, R. Snellings, and S. A. Bernal, “Supplementary cementitious materials: New sources, characterization, and performance insights,” *Cement and Concrete Research*, vol. 122, pp. 257–273, 2019.
- [78] B. Lothenbach, K. Scrivener, and R. Hooton, “Supplementary cementitious materials,” *Cement and Concrete Research*, vol. 41, pp. 1244–1256, Dec. 2011.
- [79] C. IEA, “Technology roadmap: Low-carbon transition in the cement industry,” *Geneva: World Business Council for Sustainable Development*, 2018.
- [80] M. Hossain, C. Poon, Y. Dong, and D. Xuan, “Evaluation of environmental impact distribution methods for supplementary cementitious materials,” *Renewable and Sustainable Energy Reviews*, vol. 82, pp. 597–608, 2018.
- [81] S. A. Miller, A. Horvath, and P. J. M. Monteiro, “Readily implementable techniques can cut annual CO₂ emissions from the production of

- concrete by over 20%,” *Environmental Research Letters*, vol. 11, p. 074029, July 2016.
- [82] K. Kupwade-Patil, C. De Wolf, S. Chin, J. Ochsendorf, A. E. Hajiah, A. Al-Mumin, and O. Büyüköztürk, “Impact of embodied energy on materials/buildings with partial replacement of ordinary portland cement (opc) by natural pozzolanic volcanic ash,” *Journal of Cleaner Production*, vol. 177, pp. 547–554, 2018.
- [83] S. A. Miller, “Supplementary cementitious materials to mitigate greenhouse gas emissions from concrete: can there be too much of a good thing?,” *Journal of Cleaner Production*, vol. 178, pp. 587–598, 2018.
- [84] S. Kumar, R. Kumar, A. Bandopadhyay, T. Alex, B. Ravi Kumar, S. Das, and S. Mehrotra, “Mechanical activation of granulated blast furnace slag and its effect on the properties and structure of portland slag cement,” *Cement and Concrete Composites*, vol. 30, no. 8, pp. 679–685, 2008.
- [85] S. Pal, A. Mukherjee, and S. Pathak, “Investigation of hydraulic activity of ground granulated blast furnace slag in concrete,” *Cement and Concrete Research*, vol. 33, no. 9, pp. 1481–1486, 2003.
- [86] K. De Weerd and H. Justnes, *Synergic Reactions in Triple Blended Cements*, 11th NCB International Seminar on Cement and Building Materials, ch. 257-261. 11th NCB International Seminar on Cement and Building Materials, New Delhi, India, 17-20 November, 2009.
- [87] S. W. M. Zajac, M.; Bremseth and M. Ben Haha, *Effect of $\text{CaMg}(\text{CO}_3)_2$ on hydrate assemblages and mechanical properties of hydrated cement pastes at 40°C and 60°C*, ch. 21 -29. Cement and Concrete Research, V. 65, 2014.
- [88] W. A. Gutteridge and J. A. Dalziel, “Filler cement: The effect of the secondary component on the hydration of portland cement: Part i. a fine non-hydraulic filler,” *Cement and Concrete Research*, vol. 20, no. 5, pp. 778–782, 1990.
- [89] M. C. Juenger and R. Siddique, “Recent advances in understanding the role of supplementary cementitious materials in concrete,” *Cement and Concrete Research*, vol. 78, pp. 71–80, 2015. Keynote papers from 14th International Congress on the Chemistry of Cement (ICCC 2015).
- [90] S. . M. Guggenheim, “R.t definition of clay and clay minerals,” *Joint report of the AIPEA nomenclature and CMS nomeclature committess*, no. 43, pp. 255–256, 1995.
- [91] B. Sabir, S. Wild, and J. Bai, “Metakaolin and calcined clays as pozzolans for concrete: a review,” *Cement and Concrete Composites*, vol. 23, no. 6, pp. 441–454, 2001. Metakaolin and Calcined Clays.
- [92] C. He, B. Osbaeck, and E. Makovicky, “Pozzolanic reactions of six principal

- clay minerals: Activation, reactivity assessments and technological effects,” *Cement and Concrete Research - CEM CONCR RES*, vol. 25, pp. 1691–1702, 12 1995.
- [93] J. Warren, “Calcium chloride (cacl₂) article 2 of 2: Cacl₂ minerals across time and space,” *SALTWORK CONSULTANTS*.
- [94] V. Ramachandran, “Calcium chloride in concrete,” *Appl. Sci. Pub., London, U.K.*, vol. 29, 01 2010.
- [95] J. P. Icenhower and P. M. Dove, “The dissolution kinetics of amorphous silica into sodium chloride solutions: effects of temperature and ionic strength,” *Geochimica et Cosmochimica Acta*, vol. 64, no. 24, pp. 4193–4203, 2000.
- [96] T. Zheng, L. Wang, J. Liu, J. Wang, and G. Jia, “The corrosion inhibition effect of sodium silicate and triton x-100 on 2024-t3 aluminum alloy in naoh medium: Experimental and theoretical research,” *Colloids and Surfaces A: Physicochemical and Engineering Aspects*, vol. 610, p. 125723, 2021.
- [97] Lemnitzer, Laura, Schröder, Steffen, Curbach, and Manfred, “Bond behavior between reinforcing steel and concrete under multiaxial loading conditions in concrete containments,” 2009.
- [98] V. Bilek, S. Bonczková, J. Hurta, D. Pytlík, and M. Mrovec, “Bond strength between reinforcing steel and different types of concrete,” *Procedia Engineering*, vol. 190, pp. 243–247, 2017. Structural and Physical Aspects of Construction Engineering.
- [99] B. S. I. Staff and B. S. Institution, *Steel for the Reinforcement of Concrete. Weldable Reinforcing Steel. General*. 12 2005.
- [100] M. H. Mazumder, R. Gilbert, and Z. Chang, “Analytical model for bond–slip behavior of the anchorage of deformed bars in reinforced concrete members subjected to bending,” *Journal of Building Pathology and Rehabilitation*, vol. 6, 12 2021.
- [101] M. H. Mazumder and R. I. Gilbert, “Finite element modelling of bond–slip at anchorages of reinforced concrete members subjected to bending,” *SN Applied Sciences*, vol. 1, Oct. 2019.
- [102] Bradbury, *Introduction to light microscopy*. Singapore, Singapore: Springer, 2 ed., Jan. 1997.
- [103] J. C. H. Spence, “ELECTRON OPTICS,” in *High-Resolution Electron Microscopy*, pp. 15–47, Oxford University Press, Oct. 2008.
- [104] B. Inkson, “2 - scanning electron microscopy (sem) and transmission electron microscopy (tem) for materials characterization,” in *Materials Characterization Using Nondestructive Evaluation (NDE) Methods* (G. Hübschen,

- I. Altpeter, R. Tschuncky, and H.-G. Herrmann, eds.), pp. 17–43, Woodhead Publishing, 2016.
- [105] J. Hjelen, *Scanning elektron-mikroskopi*. SINTEF, Avdeling for metallurgi Metallurgisk Institutt, NTH.
- [106] L. C. Wagner, ed., *Failure Analysis of Integrated Circuits*. Springer US, 1999.
- [107] S. Ebnesajjad, “Chapter 4 - surface and material characterization techniques,” in *Surface Treatment of Materials for Adhesive Bonding (Second Edition)* (S. Ebnesajjad, ed.), pp. 39–75, Oxford: William Andrew Publishing, second edition ed., 2014.
- [108] J. Davis, “Alloying. understanding the basics: Aluminum and aluminum,” *ASM International*, 2001.
- [109] dropforgine, “6082 aluminum forging.” <https://www.dropforging.net/6082-aluminum-forging.html>.
- [110] R. Courland, *Concrete planet : the strange and fascinating story of the world's most common man-made material*. Amherst, N.Y, Prometheus Books, 2015.
- [111] N. Tor Magnus Zackariassen, “Report on quality test,” 2015.
- [112] P. Mohazzab, “Archimedes’ principle revisited,” *Journal of Applied Mathematics and Physics*, vol. 05, no. 04, pp. 836–843, 2017.
- [113] T. P. Flaten, “Kjemisk sammensetning av drikkevann i norge . dokumentasjon av analysedata.,” *NORGES GEOLOGISKE UNDERSØKELSE*, vol. NGU-rapport, no. 90.044, p. 71, 1990.
- [114] M. Fousová, V. Valesova, and D. Vojtech, “Corrosion of 3d-printed als₉cu₃fe alloy,” *Manufacturing Technology*, vol. 19, pp. 29–36, 03 2019.
- [115] S. Perry, S. Gateman, L. Stephens, and J. Mauzeroll, “Pourbaix diagrams as a root for the simulation of polarization curves for corroding metal surfaces,” 10 2017.

Appendix

A Theoretical additional information

A.1 Pourbaix diagram for aluminium and steel

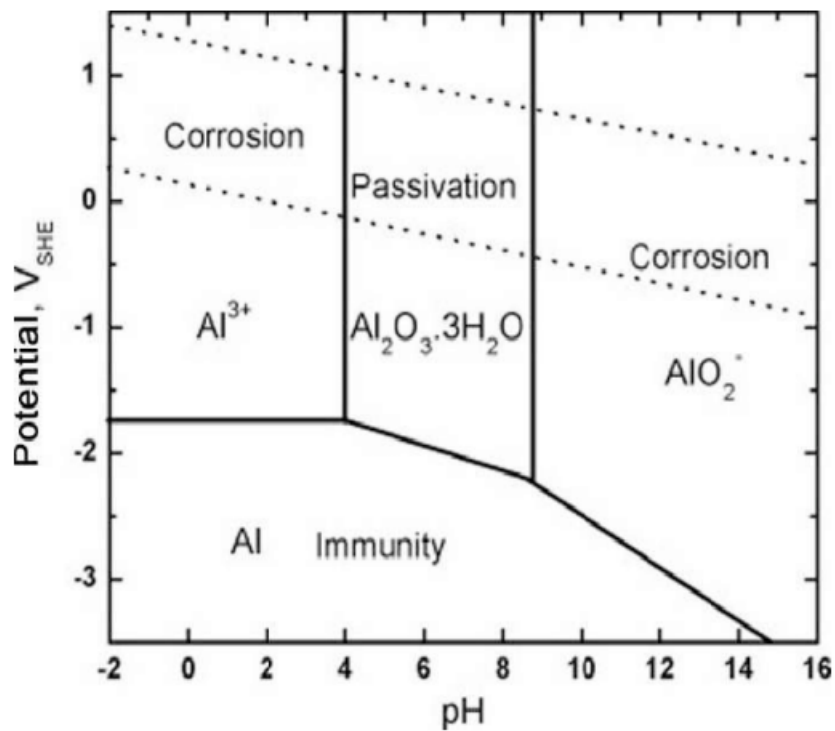


Figure A.1: Pourbaix diagram for aluminium^[114].

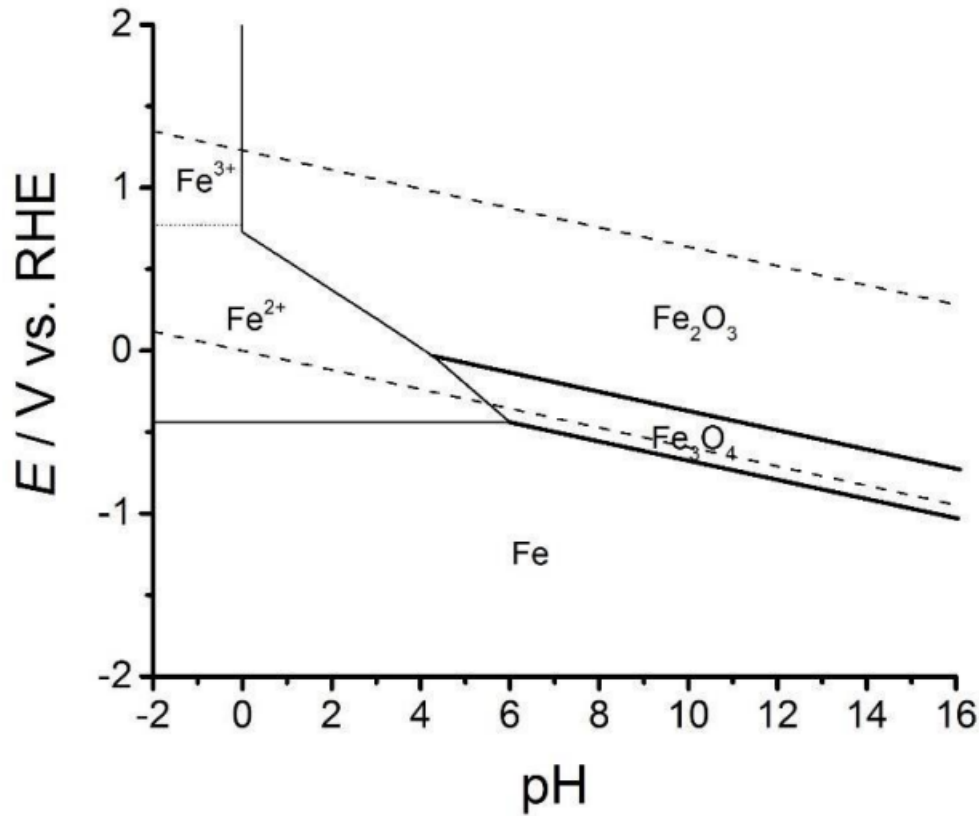


Figure A.2: Pourbaix diagram for iron^[115].

B Additional experimental information

Table B.1: List the length of the reinforcements used in each experiment.

Sample	Reinforcement length [mm]
Stationary setup	
Hyaloclastite, OCP, CaCl ₂ , 6082	39.02
Estoninan clay, OCP, CaCl ₂ , 6082	39.85
Flow system setup	
Hyaloclastite, OCP, CaCl ₂ , 6082	40.87
CC, OCP, CaCl ₂ , 6082	40.07
CC, ICEM, CaCl ₂ , 6082	39.94
CC, ICEM, 6082	41.00
CC, ICEM, CaCl ₂ , 4xxxA	39.10
CC, ICEM, 4xxxA	40.72
6082, NaOH	39.41
6082, NaSi	39.16

Table B.2: Mineral and respectively weight percent based on Rietveld analysis of XRD profiles for ICEM.

Mineral	wt %
Alite	60.4
Belite	14.4
Aluminate	7.7
Ferrite	8.8
Calcite	0.4
Periclase	1.2
Free Lime	0.4
Portlandite	0.6
Anhydrite	0.8
Gypsum	0.4
Bassanite	2.9
Aphthitalite	1.5
Arcanite	0.2
Quartz	-

Table B.3: Chemical composition of the 6082 alloy given in wt%. The alloy was analysed using ICP-MS at Hydro Sunndalsøra.

Alloying element	[wt %]
Al	97.68116
Si	0.95806
Mg	0.62716
Mn	0.4885
Fe	0.17959
Cr	0.00551
Ti	0.01268
Ga	0.01194
V	0.00918
Zn	0.00263
Ni	0.00389
Cu	0.01017
B	0.00096
Zr	0.00265
Pb	0.00099
Sn	0.00075
Na	0.00079
Ca	0.00172
Bi	0.00018
Be	0.00024
Co	0.00016
Sb	0.00012
P	0.00053
Ag	0.00021
Sr	0.00023

Table B.4: Chemical composition of 4xxxAl alloy given in wt%. The alloy was analysed using ICP-MS at Hydro Sundalsøra.

Alloying element	Weight percent[wt%]
Al	87.478
Si	9.1818
Cu	2.1494
Mg	0.2795
Ti	0.0205
Ni	0.0037
Sn	0.0031
Ca	0.0009
Bi	-
V	0.0086
Co	0.0005
Sb	0.0012
P	0.0009
Sr	0.0001
Fe	0.4094
Mn	0.1128
Zn	0.2169
Cr	0.1171
Pb	0.0012
Na	-
B	0.0023
Zr	0.0016
Be	-
Cd	0.0006
Ga	0.01
Li	-

B.1 Table: Determine the volume of air in the gas bag**Table B.5:** Individual measurements from the determination of the volume of the gas bag.

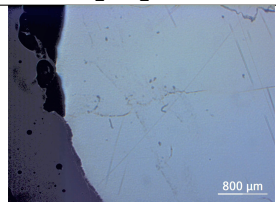
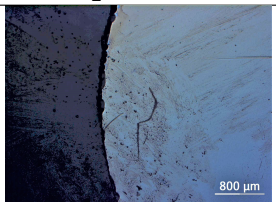
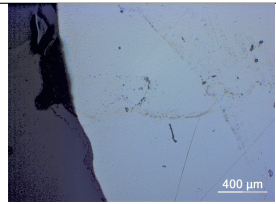
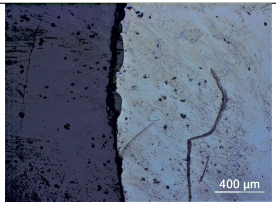
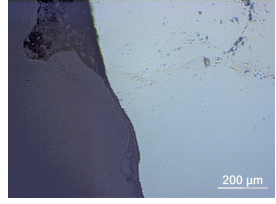
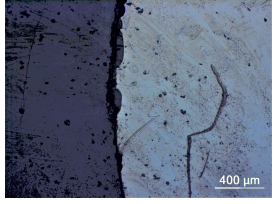
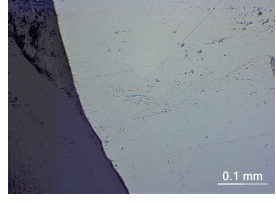
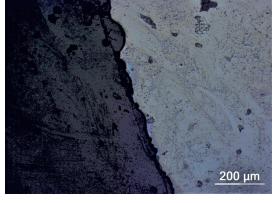
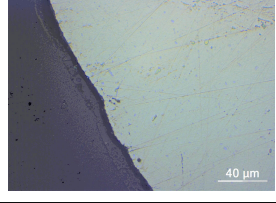
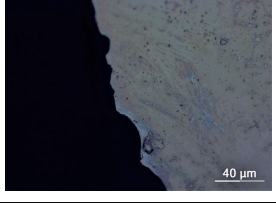
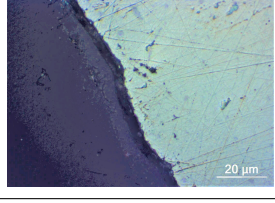
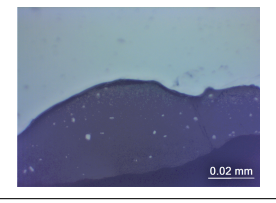
10 s		
Start [Volume]	End [Volume]	Difference [Volume]
49	191	142
54	196	142
41	184	143
13 s		
Start [Volume]	End [Volume]	Difference [Volume]
42	226	184
46	231	185
47	223	186

C Additional results

C.1 LM

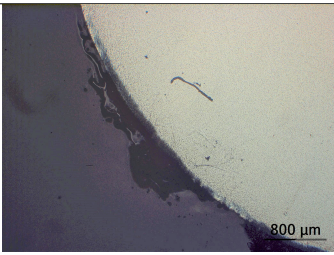
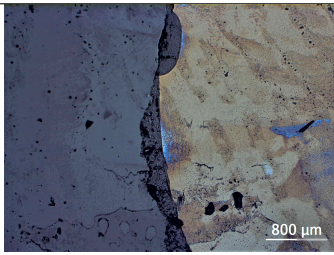
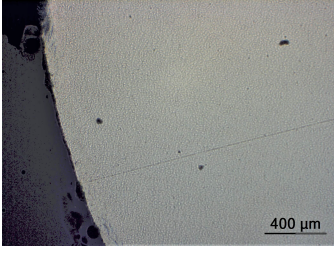
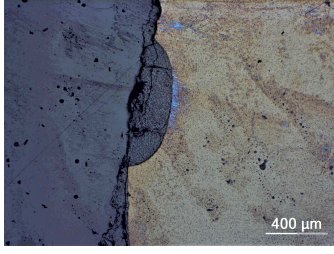
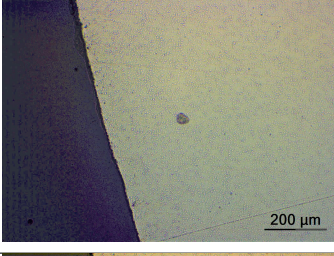
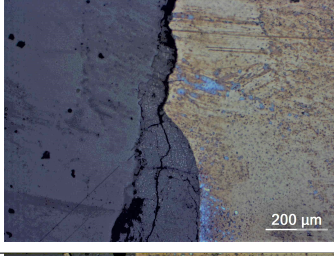
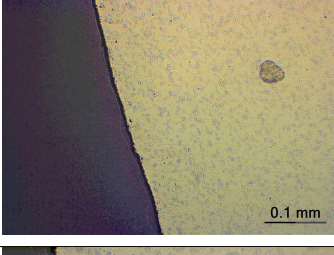
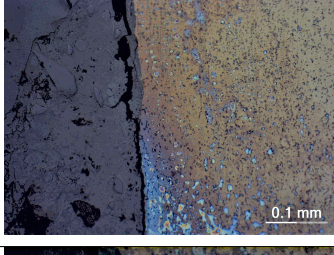
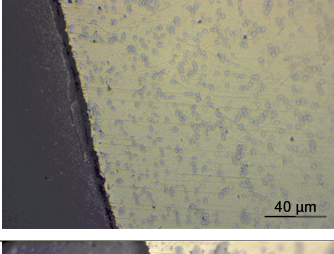
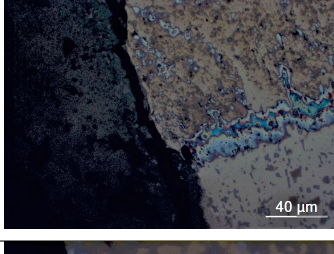
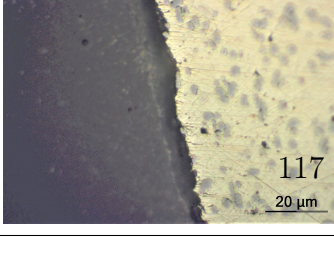
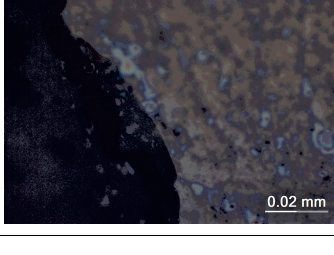
C.1.1 Difference between addition of CaCl_2 to the cement paste for 6082 reinforcements

Table C.1: The images in the table depict the difference between 6082 reinforcement with and without CaCl_2 added to the cement paste. The photos, captured using light microscopy at magnifications of 2.5X, 5X, 10X, 20X, 50X, and 100X, depict the interface surface of the 6082 reinforcements after they were removed from the concrete structure and embedded in epoxy.

	$\text{CaCl}_2, \text{H}_2\text{O}, 6082$	$\text{H}_2\text{O}, 6082$
2.5X		
5X		
10X		
20X		
50X		
100x		

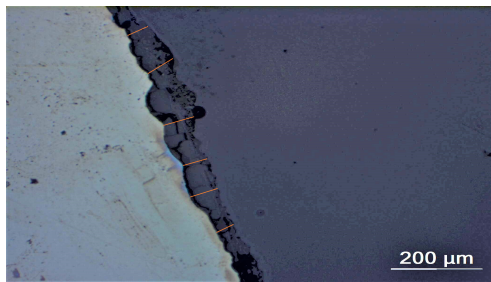
C.1.2 Difference between addition of CaCl_2 to the cement paste for 4xxxA reinforcements

Table C.2: The images in the table depict the difference between 6082 reinforcement with and without CaCl_2 added to the cement paste. The photos, captured using light microscopy at magnifications of 2.5X, 5X, 10X, 20X, 50X, and 100X, depict the interface surface of the 4xxxA reinforcements after they were removed from the concrete structure and embedded in epoxy.

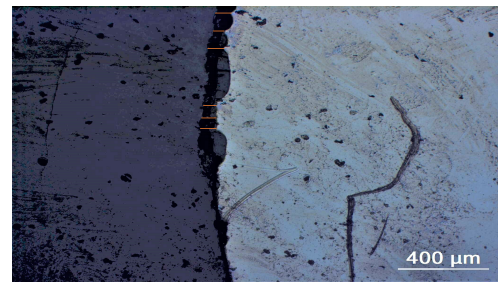
	$\text{CaCl}_2, \text{H}_2\text{O}, 4\text{xxxA}$	$\text{H}_2\text{O}, 4\text{xxxA}$
2.5X		
5X		
10X		
20X		
50X		
100X		

C.2 Coating thickness

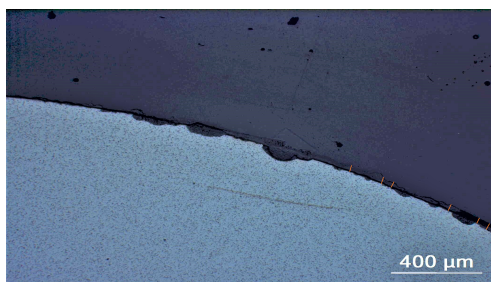
Figure C.1 depicts the six coating measurements used to calculate the thickness of each sample for samples 2, 4, 6, and 8. Using the scale in the bottom right corner of the photos, the thickness of the coating in each image (in cm) was translated to the actual coating thickness. Using the measurement data for each sample, the mean thickness and standard deviation were calculated.



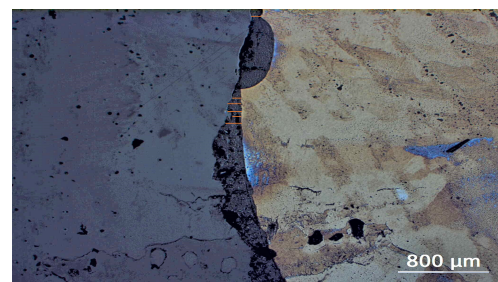
(a) Sample 2:6082,seawater



(b) Sample 4: 6082,freshwater



(c) Sample 6: 4xxxA, seawater



(d) Sample 8: 4xxxA, freshwater

Figure C.1: The image shows the six separate coating measurements for samples 2, 4, 6, and 8.

C.3 Standard deviation and noise level of the two setups using Estonian CC

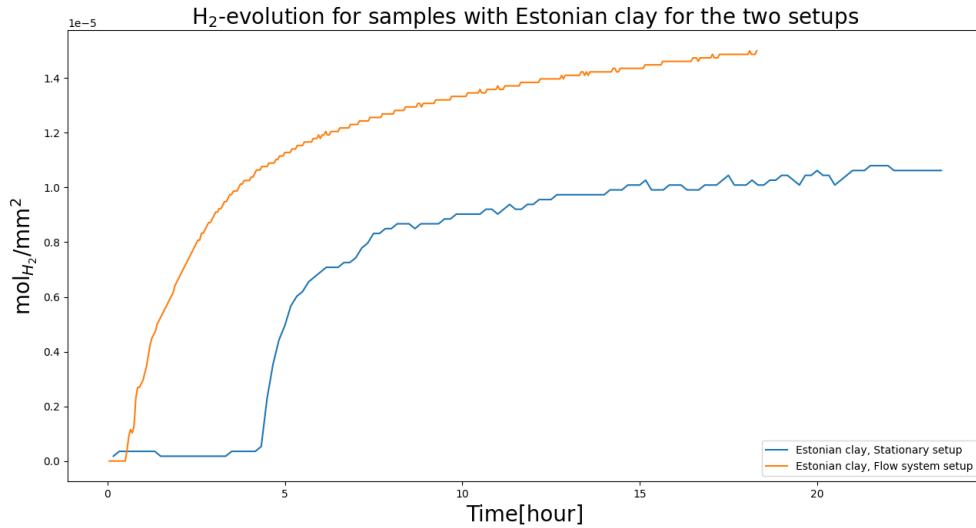


Figure C.2: Comparing H₂-development per area over time for Stationary and Flow system setups when using estonian CC. mol_{H_2} is used due to different volume for the setups.

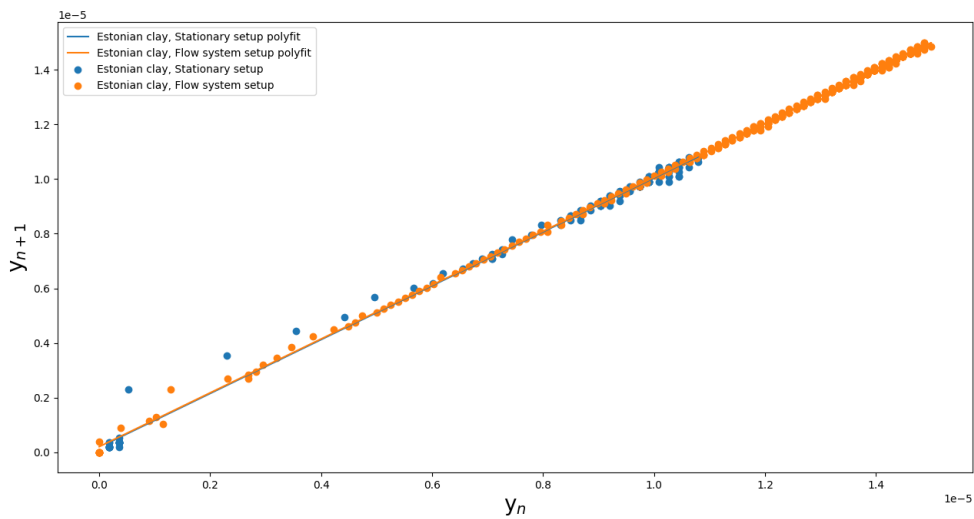


Figure C.3: Normalising of the two setups when estonian CC is used.

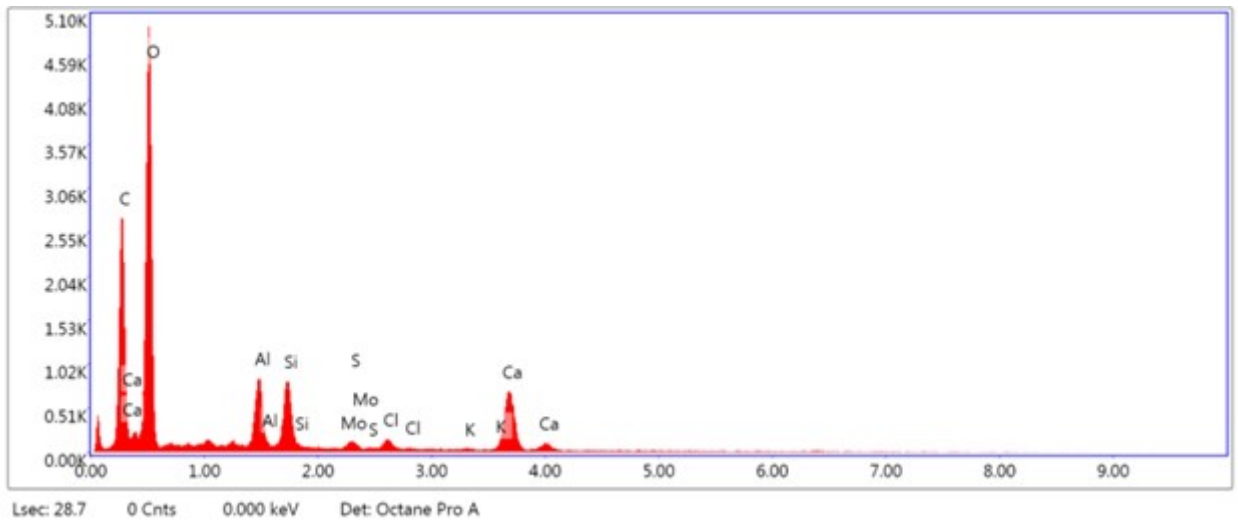
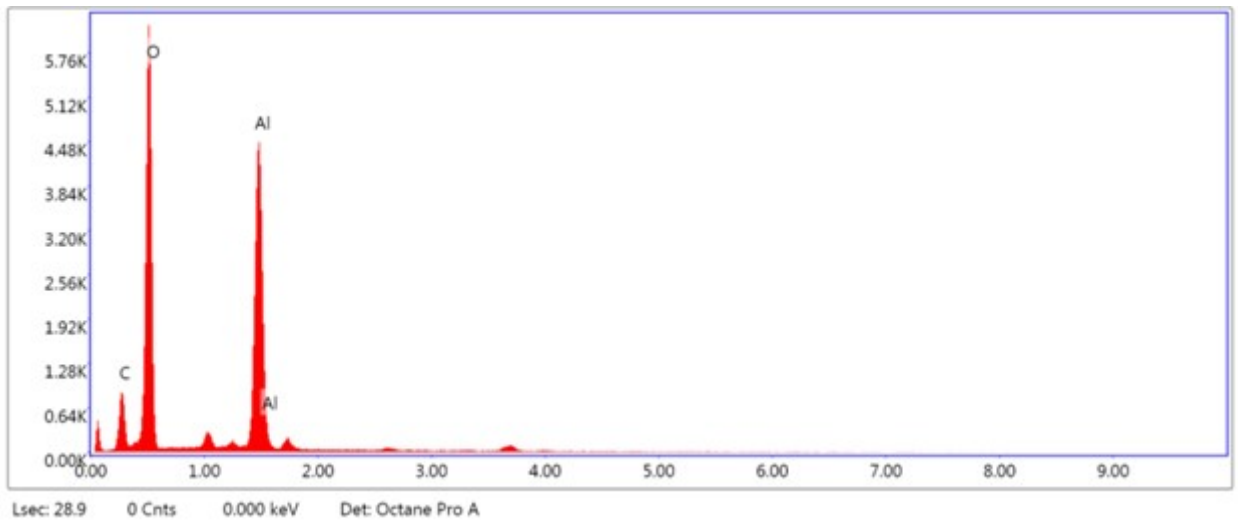
Table C.3: Standard deviation (σ) for the two setups using estonian CC as SCM.

System	Standard deviation [$\sigma \cdot 10^{-8}$]
Estonian CC, Stationary setup	9.76
Estonian CC, Flow system setup	4.98

C.4 EDS spectra

C.4.1 Surface area analysis

EDS-spectre for samples with added CaCl_2

**Figure C.4:** EDS-spectra for Area 1 in Figure 5.9.**Figure C.5:** EDS-spectra for Area 2 in Figure 5.9.

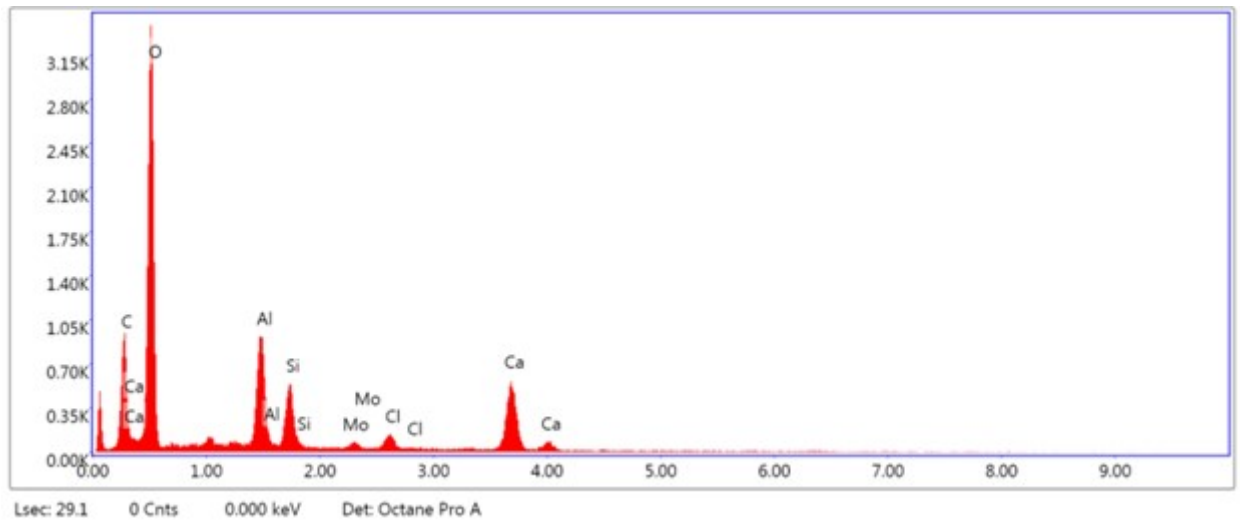


Figure C.6: EDS-spectra for Area 3 in Figure 5.9.

EDS-specter for samples without added CaCl_2

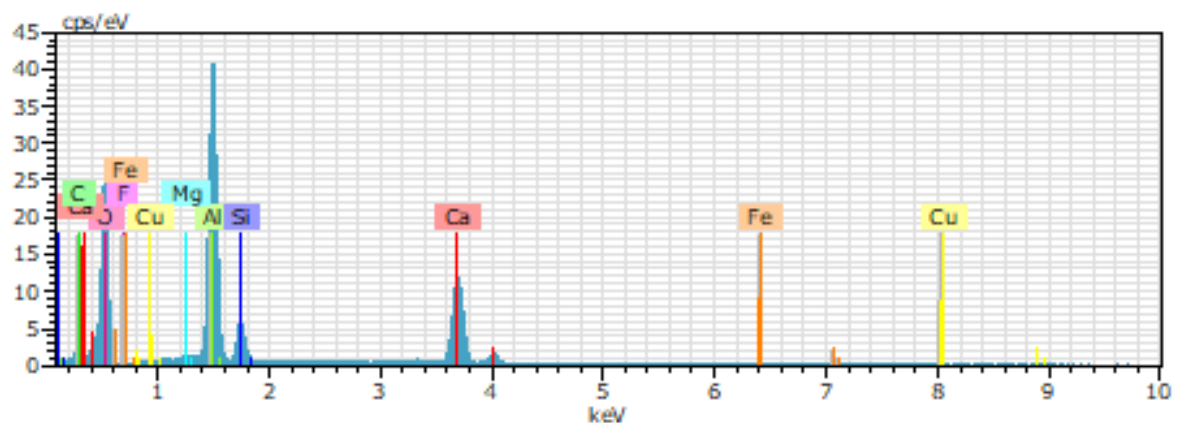


Figure C.7: EDS specter for Point A in Figure 5.10.

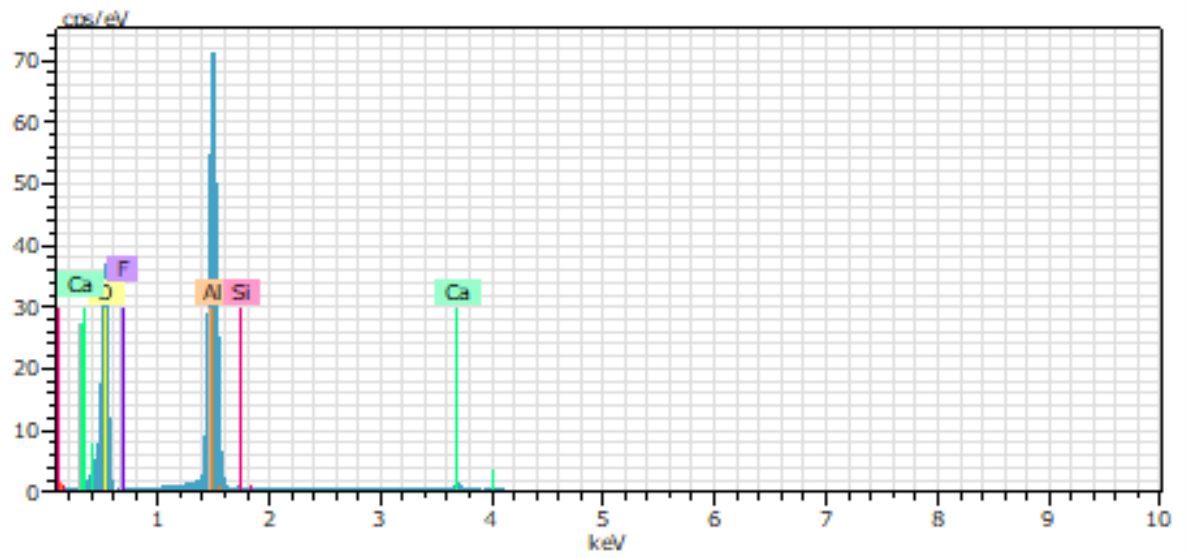


Figure C.8: EDS specter for Point B in Figure 5.10.

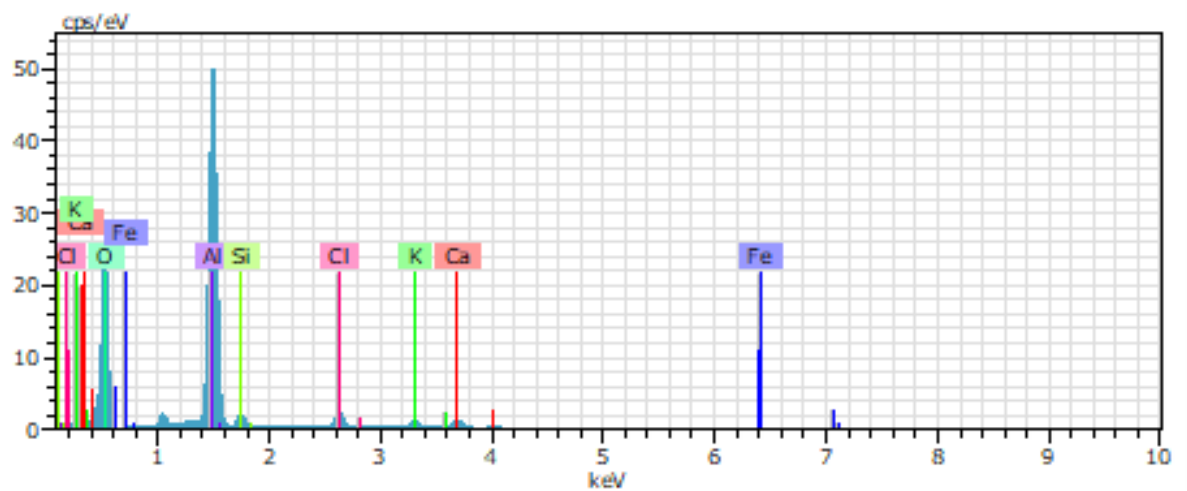


Figure C.9: EDS specter for Point C in Figure 5.10.

C.4.2 Interfacial analysis

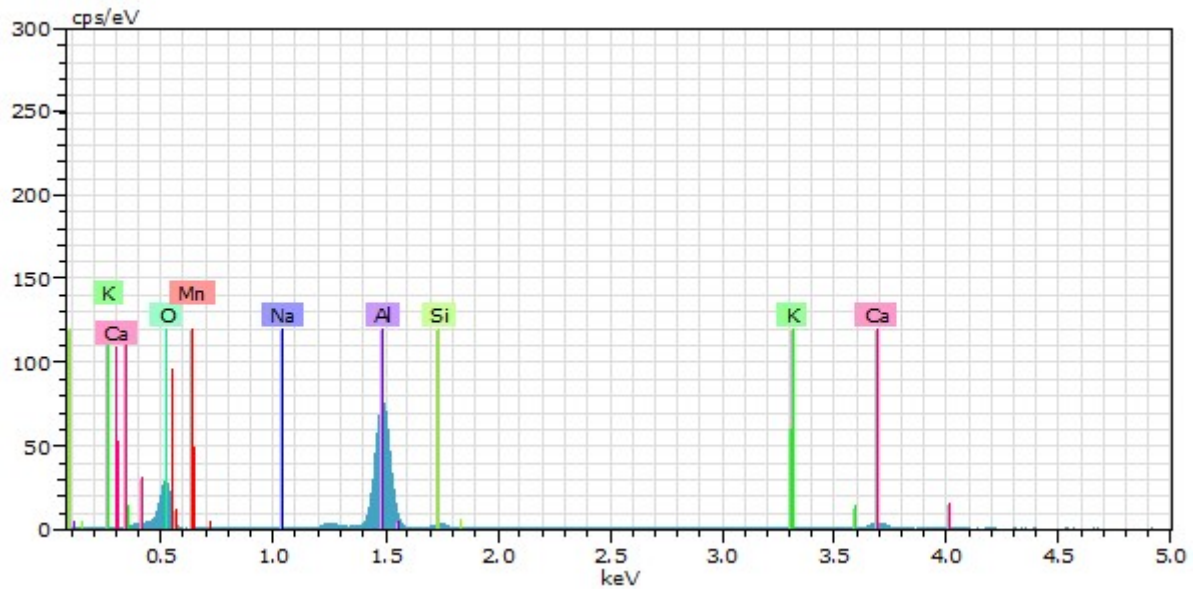
EDS-spectre for samples without CaCl_2 

Figure C.10: EDS specter for the interface layer in Figure 5.15.

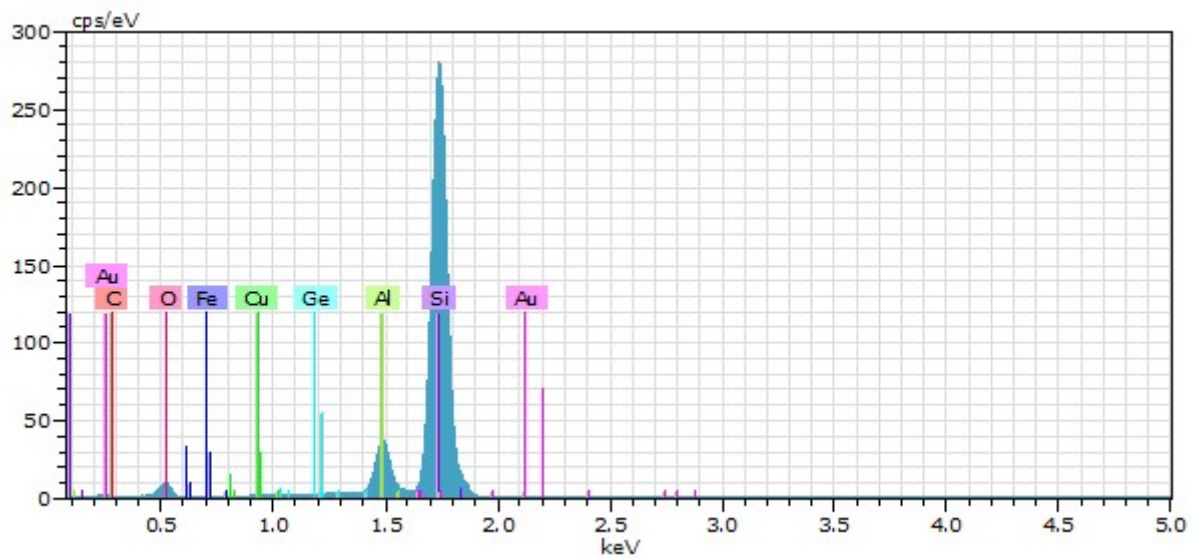


Figure C.11: EDS spectre of observed clusters in Figure 5.16.

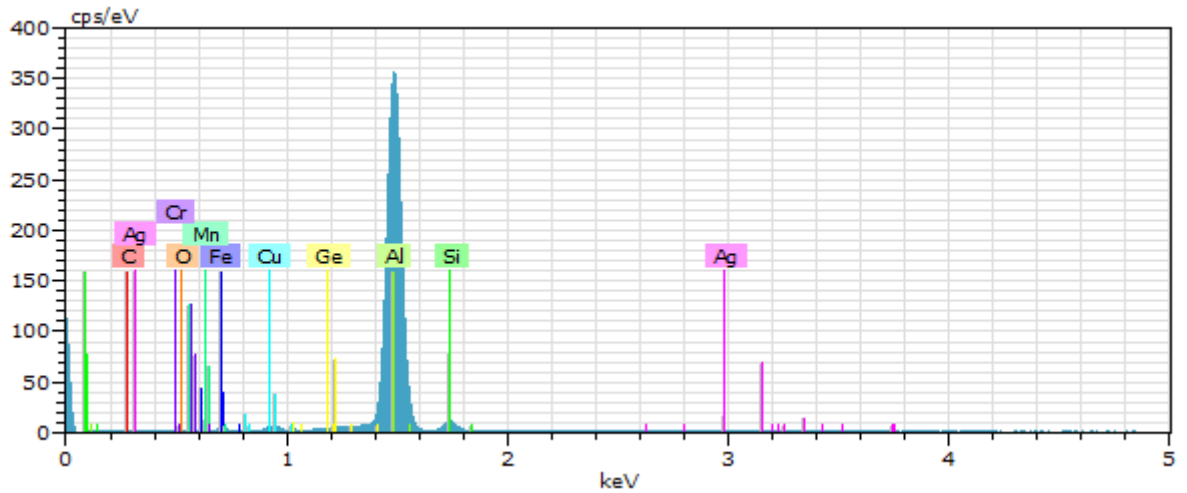


Figure C.12: EDS spectre of cluster in reinforcement in Figure 5.16.

C.4.3 EDS-spectres for samples with CaCl_2

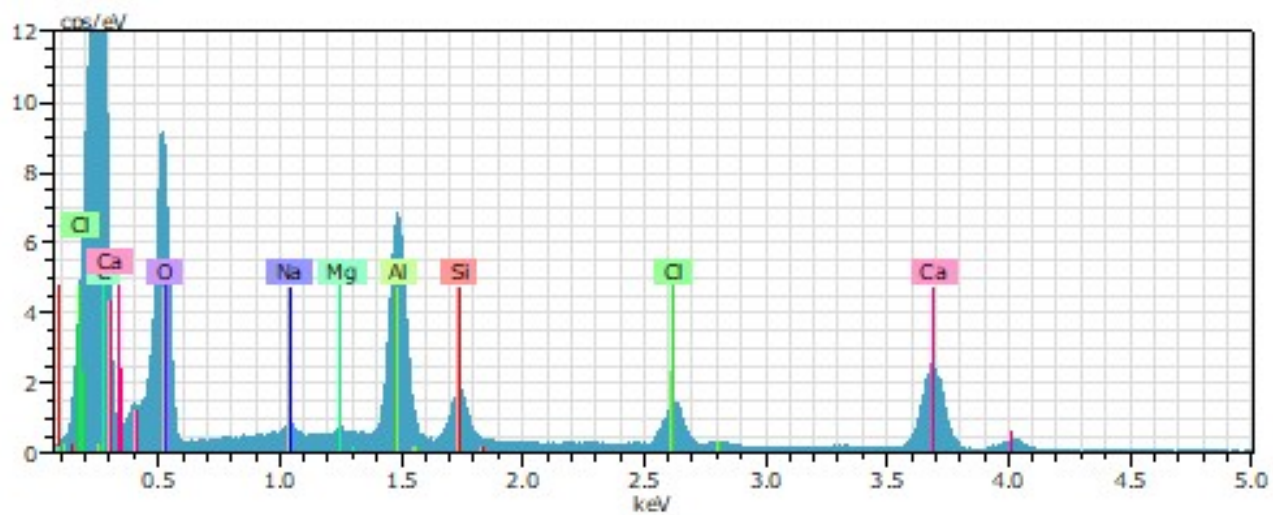


Figure C.13: EDS specter of the EDS-analysis in Point A given in Figure 5.17.

